Stockholm University

Master Thesis

Degree Project in
Marine Geology 60 hp

Testing mechanisms for potential terrace formation from submarine groundwater discharge in the archipelago south of Stockholm

Malin Lindström

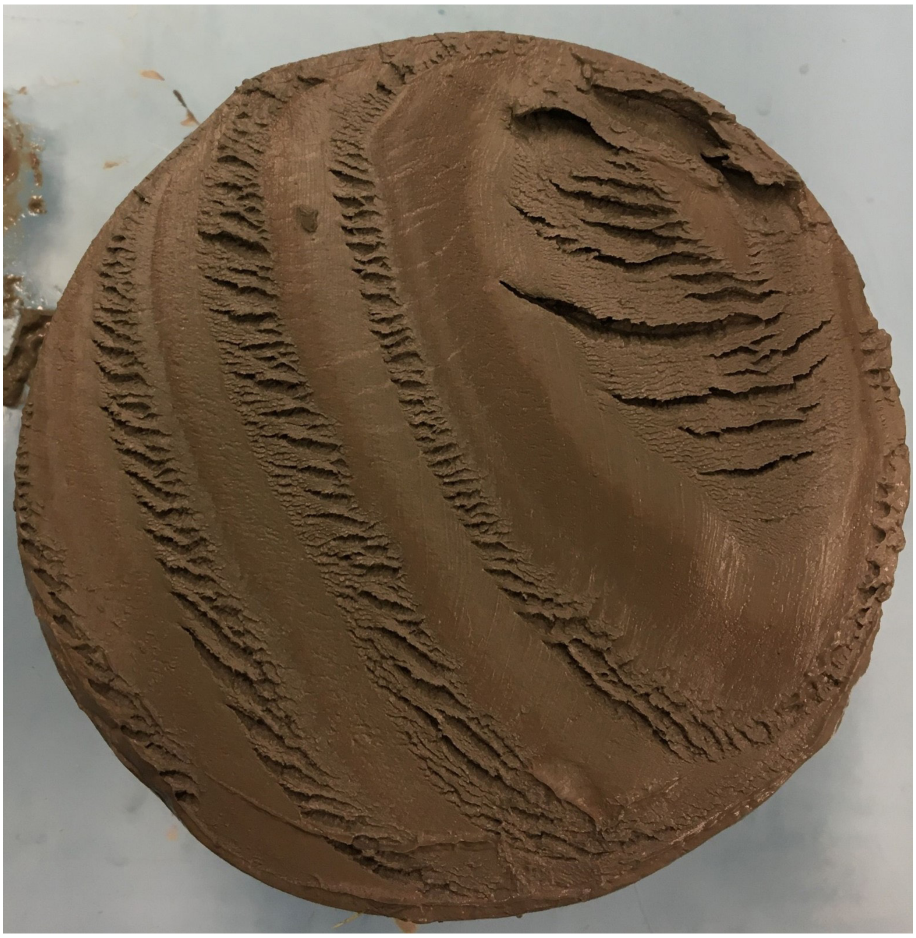

Stockholm 2022

Department of Geological Sciences
Stockholm University
SE-106 91 Stockholm

Abstract

The flow of groundwater from terrestrial aquifers to the oceans through sediment or bedrock, known as submarine groundwater discharge (SGD), can be an important source of pollutants and nutrients to the oceans. In the archipelago south of Stockholm, terraces in the seabed have been suggested to potentially result from erosion by water transported through silty layers in the varved glacial clay discharging at the seafloor as SGD. If the terraces are the result of SGD, mapping these features could help identify where groundwater drains to the Baltic Sea. In this project, geophysical and geotechnical methods have been used to investigate the subsurface geometry and physical properties of terraces located off the coast of Fifång island, to investigate the possibility of sediment erosion by groundwater using Darcy's Law calculations. The geophysical mapping show that terraces systematically occur in glacial clay where the less permeable overlying sediment have been eroded, allowing for potential upward fluid migration. Consequently, terraces mainly appear to form in shallow waters in the near-shore areas, where more extensive erosion have taken place. One-dimensional consolidation tests on sediment samples from the terraces are combined with grain size, grain density and geophysical analyses of the sediment, revealing a relationship between a downcore increase in silt and an increase in hydraulic conductivity for any specific porosity as the silt content increases. The groundwater flow calculations show that the seepage velocities generated through either a clay-enriched or a silt-enriched glacial clay are too low to cause erosion of the terrace sediments. For erosion to occur the hydraulic conductivity and/or hydraulic gradient need to increase with several orders of magnitude. Further research is needed to evaluate terrace formation by piping erosion from groundwater flowing via alternative flow paths.

Keywords: Submarine groundwater discharge, marine geophysical mapping, marine geotechnics, glacial clay, internal erosion, Baltic Sea.

Table of Contents

1. Introduction

Submarine groundwater discharge (SGD) is defined as the flow of water on the continental margins from land to the coastal sea where it discharges below the sea surface . There are several driving forces for SGD, such as terrestrial hydraulic gradients , pressure gradients induced by currents in the near shore zone, or tidally driven flows . The total flow of water via SGD can therefore have both terrestrial and marine components in terms of fluid composition and flow drivers (Moore, et al., 2008 and Taniguchi, et al., 2019) and its global discharge into the oceans have been estimated to be comparable to that of rivers (Kim & Lee, 2003; Hwang, et al., 2005; Moore, et al., 2008; Kim & Kim, 2011; Rodellas, et al., 2015 and Cho, et al., 2018). Meanwhile, recent studies estimate that the global volume of the freshwater component from SGDs only correspond to approximately 1% of the annual river discharge or even as low as ~ 0.6% of the total freshwater input to oceans . These numbers contrast with the large amount of fresh and recirculated water suggested by previous authors and it is acknowledged that the amount of discharge can vary locally (Peltonen, 2002; Burnett, et al., 2006 and Luijendijk, et al., 2020) largely to due to the type of geological setting . Therefore, the exact amount of discharge from SGDs into the oceans is not known and research is needed to identify where it occurs and how to calculate the flow. One of the important aspects of understanding SGD systems is that they can provide a pathway for nutrients and other dissolved elements, such as metals and nuclear waste, to reach the oceans (Johannes, 1980; Taniguchi, et al., 2002; Burnett, et al., 2006; Moore, et al., 2008; Ma & Zhang, 2020).

By using marine geophysical mapping, detection of SGD can be made by locating morphological features in the seabed formed by erosion of the sediments from water driven through permeable layers in the sediment. Examples of such formations are valleys, depressions, and terraces in the seabed. Valleys and depressions have been studied globally, such as valleys on the New Jersey continental slope , 40 m wide and 2 m deep depressions off the east coast of Australia , and 20- 700 m wide and 10- 20 m deep depressions on the South-east coast of New Zealand . Around the Baltic Sea and in North America the landscape is shaped by glacial activity, leaving buried eskers, till and coarser layers in the glacial clay to serve as permeable layers for SGD (Robb, 1984; Soderberg & Flodén, 1992; Goff, et al., 2019; Gustafson, et al., 2019; Virtasalo, et al., 2019 and Jakobsson, et al., 2020). In Sweden, seafloor terraces were first detected in the southern archipelago of Stockholm, with lengths of 100- 1500 m and heights of 1- 3 m (Söderberg and Flodén, 1992, 1997). In the walls of the terraces there were holes/cavities that were suggested to serve as groundwater outlets, formed by fluid seepage through coarser silty layers in the glacial clay. The terraces were hypothesised to have been formed by the erosion or 'spring sapping', as debris of glacial clay were found along the base of the terrace walls which indicate collapse of the sediment (Söderberg and Flodén, 1992, 1997). Similar findings of debris next to depressions found offshore New Jersey also suggest this erosion process .

Through geophysical mapping east of Askö, south of Stockholm in south-central Sweden, and in Blekinge in southern Sweden, Jakobsson et al. (2016, 2020) discovered <1 m high terraces extending from a few meters to >100 m outside Askö, and terraces extending >550 m in Blekinge. In both instances the terraces were formed in glacial clays that outcrop at the seafloor. Observations of 1-2 cm wide holes in the walls of the terraces outside Askö resembles the cavities described by Söderberg and Flodén (1992, 1997). Jakobsson et al. (2020) concluded that the terraces in the near-shore areas of the Baltic Sea could have been formed according to the original hypothesis put forward by Söderberg and Flodén (1992, 1997), i.e., by erosion during groundwater seepage through silty layers in the glacial clay, which caused the undermining of the sediment and subsequent failure and terrace formation. The driving force of SGD was suggested to be the hydraulic gradient (dH/dL) between the groundwater table and the discharge outlet at the terrace site (Figure 1).

In this project the terraces east of Askö are further investigated (Figure 2) and quantitative evaluations are made to determine if hydraulic heads from the local groundwater table are sufficient to drive SGD and lead to spring sapping (erosion) at sites where seafloor terraces are formed. The main hypothesis of this project is partly the same as brought forward by Söderberg & Flodén. (1992; 1997) and Jakobsson et al. (2020); that the seafloor terrace formations are a result of the SGD through silty layers in the glacial clay, which cause erosion and failure of the sediment. To test this, sediment permeability-porosity-grain size relationships are defined through laboratory geotechnical testing and the subsurface geometry and thickness of the sediments that groundwater would need to flow through to reach the terraces are constrained using geophysical data. This is combined with observations on groundwater table variations in the region.

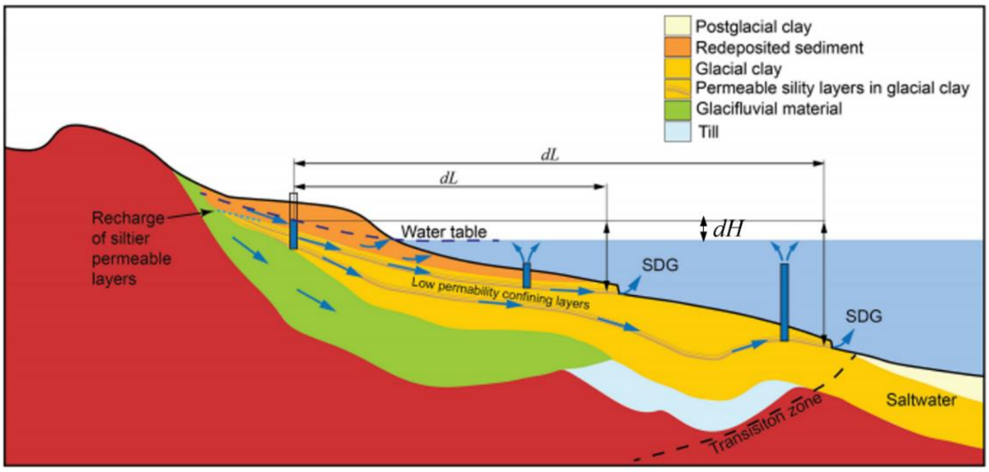

Figure 1. Schematic diagram of the formation of terraces and the flow paths of SGD, modified from Jakobsson et al. (2020). The spatial dimension parameters required for fluid flow according to Darcy's law is illustrated; Length of the flow path along the permeable layer from source to outlet (dL) and the change in hydraulic head (dH) from the groundwater table to the sea surface.

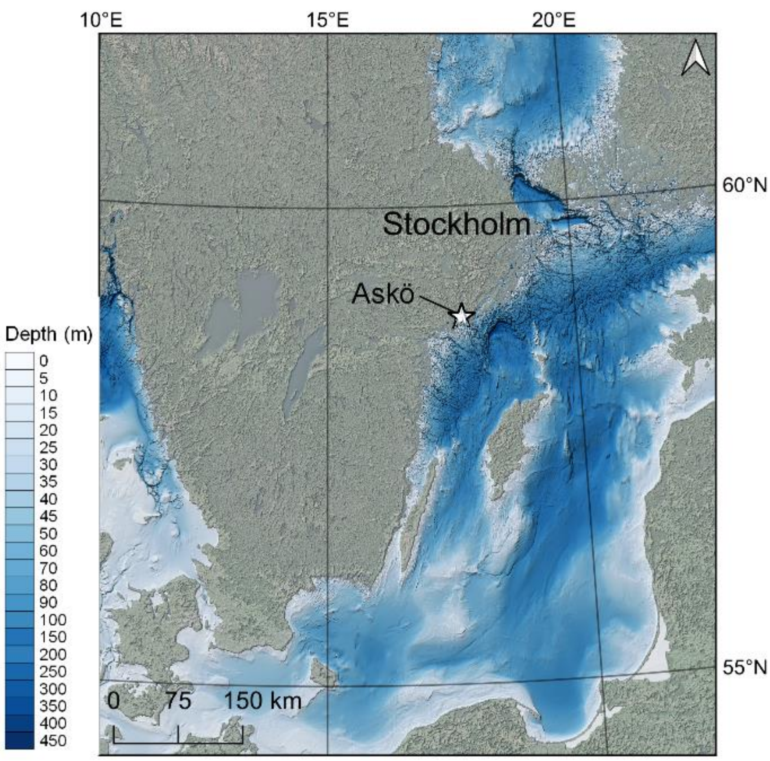

Figure 2. Location of the study site of Askö in the archipelago south of Stockholm, Sweden, where seafloor terraces were mapped by Jakobsson et al. (2016 , 2020). Land images from © Google Satellite; Bathymetry (DTM) from EMODnet Bathymetry Consortium (2020): EMODnet Digital Bathymetry (DTM). Coordinate reference system: WGS 84/UTM zone 33N.

1.2. Background

1.2.1. Geotechnical background

Internal erosion

Erosion within a sediment parcel or sequence is called *internal erosion*. There are two main types of internal erosion: suffusion and piping . Suffusion is the erosion process where finer particles within a coarser grained skeleton are eroded away in the direction of internal fluid flow (Wan & Fell, 2008; Briaud, et al., 2019; Werner, et al., 2020). Piping is the erosion of sediments where flow is channelized in a pipe system and can thus be regarded as *surface erosion* internally to the structure .

Erosion occurs when flowing water reaches a critical velocity (v_c), where the drag force (F_D) of the water upon the grains results in a shear stress (τ) that exceeds the weight (F_N), friction (F_F) and cohesion (F_C) of the grains, resulting in a lift force (F_L) (Grabowski, 2011; Bonelli, et al., 2007; Briaud, et al., 2019) (Figure 3). Thus, the critical parameters determining if erosion will occur are (1) critical fluid velocity (v_c) and (2) critical shear stress (τ_c). The critical fluid velocity depends on the hydraulic head (**H**) and the intrinsic permeability (**K**, m^2) or hydraulic conductivity (**k**, m/s) of the sediment. Intrinsic permeability and the hydraulic conductivity depend on the porosity **(ϕ)** and grain size distribution. The critical shear stress will be governed by the shear strength of the sediment, which in turn is heavily dependent on cohesion and consolidation state . Cohesion is the force which occurs from attractions between negative charged sheeted clay silicates and other particles through Van der Vaals bonds, and other inter-particle attraction forces owing to the clay particles (Bonelli, et al., 2007 and Rankka, et al., 2004). A sediment is defined as cohesive if it contains > 4-10 % clay (Grabowski, et al., 2011; Zahidul & Kuleza, 2020). However, the presence of silt reduces the cohesive properties of clay-rich sediment by increasing the permeability (Higgins, 1982; Dunne, 1990; Schneider, et al., 2011; Briaud, et al., 2019).

Consolidation

Consolidation is defined as the time-dependent process of porosity reduction as pore water is expelled from saturated sediments resulting in compression and stress transfer . It occurs when a load is applied to a sediment parcel, whereby the load is initially transferred to the pore water as excess pore pressure (u_e). As the pore water is expelled, the stress is transferred to the grains, which causes an increase in the effective stress (σ'_v) of the sediment. The time it takes for a sediment to consolidate depends on the hydraulic conductivity (k, m/s) or the intrinsic permeability (K, m^2), which defines how quickly water can dissipate from the sediment .

The time-dependent consolidation of sediments can be reproduced in the laboratory by performing a consolidation test, or *oedometer test*. During the test a sediment sample is compressed and decompressed under specific incremental loading and unloading steps. At each step the consolidation (settlement) over time is measured. Based on the changes in sediment height over time, several parameters can be calculated, including void ratio (e) or porosity (ϕ), sediment compressibility and hydraulic conductivity (k). Specifically, these tests allow us to derive relationships between porosity-stress (burial depth)-permeability that can be used to model the in-situ properties of sediments.

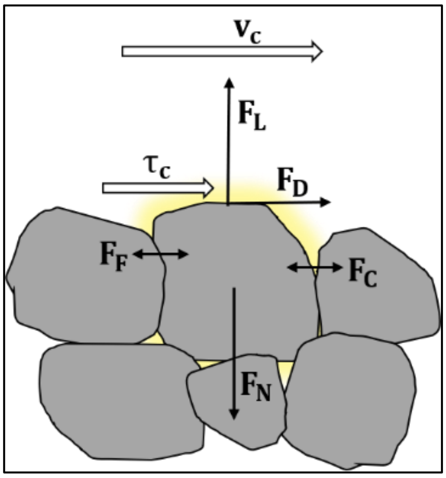

Figure 3. Illustration of a cohesive sediment during erosion by flowing water, showing the resulting forces acting on a grain and the critical parameters for movement of the particle. The resisting forces are; F_F: friction, F_C: cohesion, F_N: Normal force (weight of the particle). The driving forces, resulting from the moving water, are; F_L: Lift force, F_D: Drag force. The critical parameters for movement are: τ_c: critical shear stress, v_c: critical velocity.

1.2.2. Baltic Sea sedimentation history with respect to Askö

Sediment stratigraphy in the Baltic Sea largely reflects paleoenvironmental changes during the latest deglaciation of the Fennoscandian Ice Sheet (FIS) between ~16-8 cal. ka BP . During deglaciation the Baltic Sea basin went through four main stages of formation, where the basin was alternatingly cut off and connected to the North Sea.

The initial period of ice sheet retreat beginning ~16 cal. ka BP formed the first stage known as the Baltic Ice Lake (BIL) through melting of the northward retreating glacial ice . At 13 cal. ka BP the first drainage of BIL occurred through south-central Sweden close to Mt. Billingen due to a 10 m water level difference between the BIL and the North Sea (Andrén, et al., 2011; Swärd, et al., 2016). During this period the Askö region was just south of, or underneath the ice margin, as the Askö region is located slightly above the Levene recessional moraine that was formed around 13.4 cal. ka BP (Figure 4A). During the Younger Dryas cooling period (12.9-11.7 cal. ka BP) the ice margin readvanced and retreated in oscillations which formed a band of end moraines, called the Middle Swedish End Moraine Zone (MSEMZ) which extended from Skövde to the Askö region (Figure 4A). In front of the ice margin, varved glacial clays are deposited generally due to the expulsion of fine-grained material in meltwater. The varves are composed of a slightly coarser grained and thicker summer layer when meltwater output is high, and a thinner and slightly finer winter layer when meltwater is reduced. Furthermore, the thickness and grain size of the varved glacial clays vary in response to the distance from the ice margin. Coarser and thicker varve sequences represent deposition closer to the ice margin.

At the end of Younger Dryas around 11.7 cal. ka BP, isostatic uplift and a milder climate caused rapid retreat of the FIS. As the icesheet retreated north of Mt Billingen a final drainage of the BIL occurred, when 7800 m^3 water flowed out of the BIL . At this time the ice margin was located 30 km south of Stockholm , located about 30 km north of the Askö region (Figure 4B). A pathway to the North Sea was opened again which led to the formation of the next Baltic basin stage; the Yoldia Sea (YS), during which rapid warming led to increased ice recession and sedimentation rates. In sediment cores retrieved at locations close to the ice margin during early YS, thicker and coarser grained layers are indicative of (both) the BIL drainage(s) as deposition occurred close to the margin, followed by thinner and finer grained varves representing an increasing distance to the ice (Swärd, et al., 2016 and Swärd, et al., 2018) and homogenous clay depositing when the ice was furthest away . This implies that older sediments likely consist of a higher amount of coarser grains compared to the younger sediments . At the end of the YS stage only the Bothnia Bay in the north was still glaciated and postglacial sedimentation occurred in the central part of the basin .

Continued uplift led to the Baltic basin once again to become cut off from the sea, marking the onset of the Ancylus stage at 10.7 ka BP, represented by low organic productivity and highly oxygenated bottom waters . A rising sea level and increasing organic content initiated the onset of the Littorina Sea around 8-8.5 ka BP, which is the ongoing stage of the Baltic basin (Andrén, et al., 2011; Björck, 1995). The Askö region had still not emerged from the water during the onset of the Littorina Sea, however, continued isostatic uplift may have resulted in the creation of a present-day hydraulic head between the (eventually) landward and seaward parts of glacial clay layers of Askö .

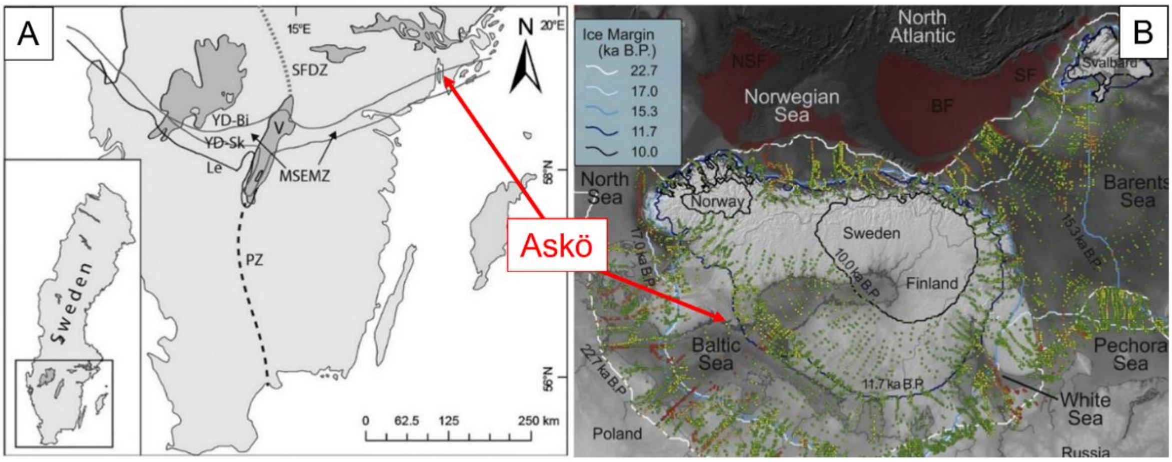

Figure 4. Location of the ice sheet margin with respect to Askö region during the retreat of the Fennoscandian Ice Sheet. A: Illustration modified from Swärd et al. (2016) that shows the extents of the Levene recessional moraine (Le) and the Middle Swedish End Moraine Zone (MSEMZ). Also shown, but not discussed, is the Sveconorwegian Frontal Deformation Zone (SFDZ), Younger Dryas-Billingen ice marginal line (YD-Bi), Younger Dryas-Skövde ice marginal line (YD-Sk), Lake Vättern (V) and the Protogine Zone (PZ). B: The positions and dates of the ice margin during the FIS retreat (Figure modified from Shackleton et al. (2018)).

2. Materials and method

2.1. Survey area

The survey area is in the archipelago south of Stockholm, east of Askö Island (Figure 5Figure 5). The main research area for this project is on the terraces outside the SW shore of Fifång Island, about 3.5 km NE of Askö (Figure 5C). Hydrological and geological information on the survey area was obtained from the islands Askö, Fifång, Boko-Oxnö and Brännskär based on reports from the Geological Survey of Sweden (SGU, 2021).

2.1.1. Groundwater tables

The measured groundwater levels from the wells on Askö and Fifång dates to the same time as they were drilled, which was 2017-05-10 on Askö and 2006-06-07 on Fifång, while no information of when the measurements on Bokö-Oxnö and Brunnskär is provided (SGU, 2021). The groundwater well on Fifång is located at the boundary between granite and slate and the measured groundwater level is 32 m below the surface of the well (SGU, 2021). Based on the elevation at the well site, this corresponds to a groundwater table of -26 masl (Figure 5Figure 5). This is very low compared to the groundwater tables of the other islands (Figure 5Figure 5). The reported initial level in the Fifång well was measured in 2006-06-07, and is much below the present water level provided from ocular inspection by the Askö personnel in Feb 2022. According to the groundwater well information provided in the area (SGU, 2021) the well on Fifång is drilled in gneissy bedrock, while the wells on Askö are drilled in granitic bedrock.

No bedrock information for the wells on Bokö-Oxnö and Brännskär is provided by SGU (2021), but they seem to be in either granitic or sedimentary bedrock (Figure 6).

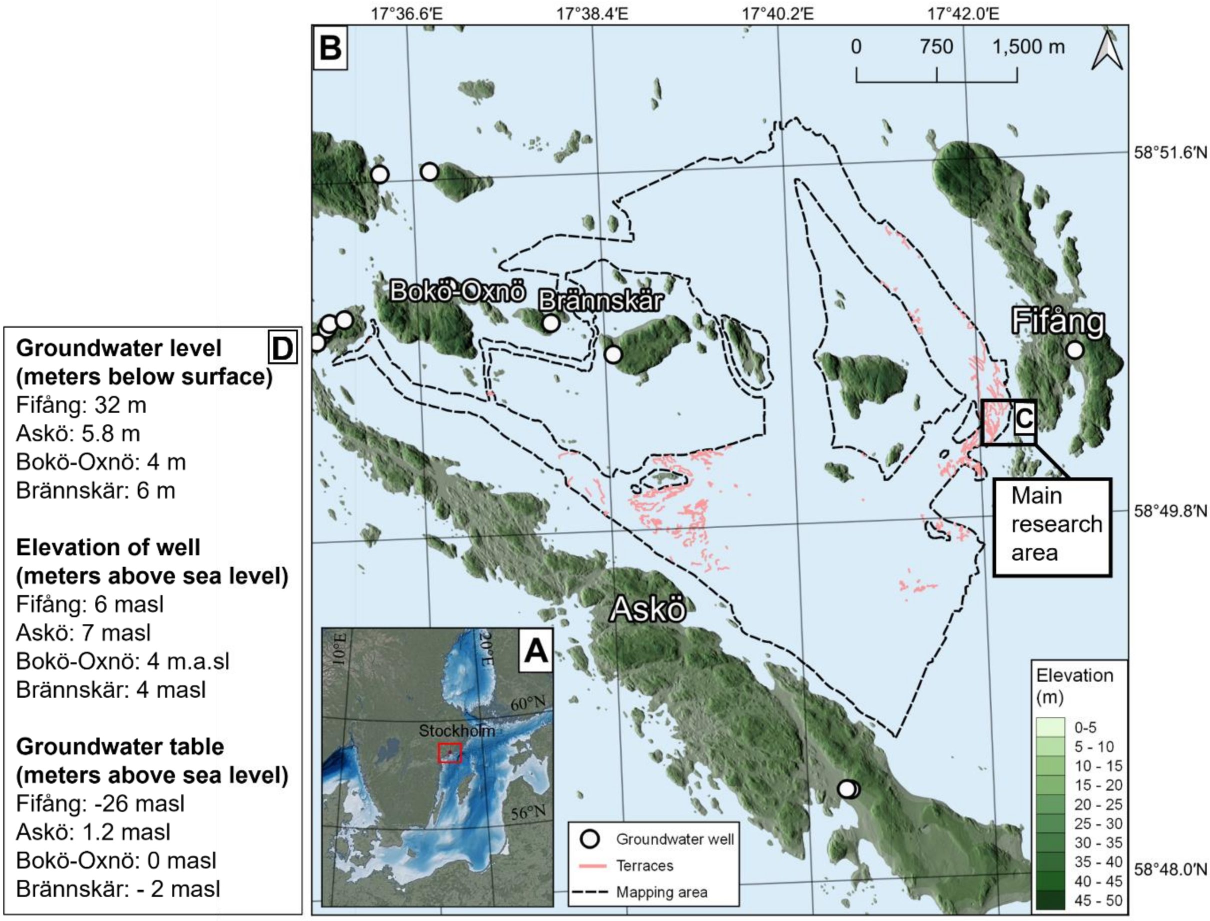

Figure 5. Map of the survey area including groundwater level information and locations of terraces. A: Overview of the survey area shown on a map of Sweden and the Baltic Sea (the size of the red box corresponding to the survey area is exaggerated for presentational purposes). Land images from © Google Satellite; Bathymetry (DTM) from EMODnet Bathymetry Consortium (2020): EMODnet Digital Bathymetry (DTM). B: The survey area east of Askö. The mapped seafloor is marked with black dotted lines. Groundwater wells are present on several locations, but only the islands Askö, Fifång, Bokö-Oxnö and Brännskär contain information about the groundwater levels © SGU (2021). The groundwater levels were measured 2017-05-10 on Askö and 2006-06-07 on Fifång, while the dates for measurements on Bokö-Oxnö and Brunnskär are undocumented (SGU, 2021). The elevations of the islands and the wells are obtained from the Terrain model (DTM) grid 1 © Lantmäteriet (2021). The terraces are mapped and digitized by M. Jakobsson. C: The main study area for this project and location of the core site. D: Groundwater table and elevation information for the wells (SGU, 2021 and Lantmäteriet, 2021). Coordinate reference system: WGS 84/UTM zone 33N.

2.1.2. On-shore geology

The islands in the research area are dominated by gneissy granites and granodiorites, and all contain metasedimentary rocks, such as sandstones and greywackes (SGU, 2021, Figure 6A). The sedimentary sequences are mainly localized in the northern and northeastern part of Askö and in the west side of Fifång, both facing the survey area and the locations of the mapped terraces (Figure 5B, Figure 6A). The bedrock of Askö also contains metavolcanic rocks such as rhyolites and basalts and some intrusions of gabbro, diorites and dolerites (SGU, 2021). Deformation zones cut through all islands and rock types, with one main deformation group extending NW-SE, and another, less coherent, in an NNE-SSW to NE-SW direction. On Fifång, the NW-SE deformation zones are most notable as well as one distinct zone extending NNE-SSW through the central southern part of the island (Figure 6A). Sandy tills and glacial clays are found on all islands, and postglacial sediments such as wave washed gravel, postglacial sand and gyttja clay are also present on Askö (Figure 6B). The sediment cover is generally thin on all islands (0-5 m) but with locally thicker strata up to 20 m (Figure 6C). Toward the shores that face the survey area sediment cover is absent on all islands (Figure 6B) (SGU, 2021).

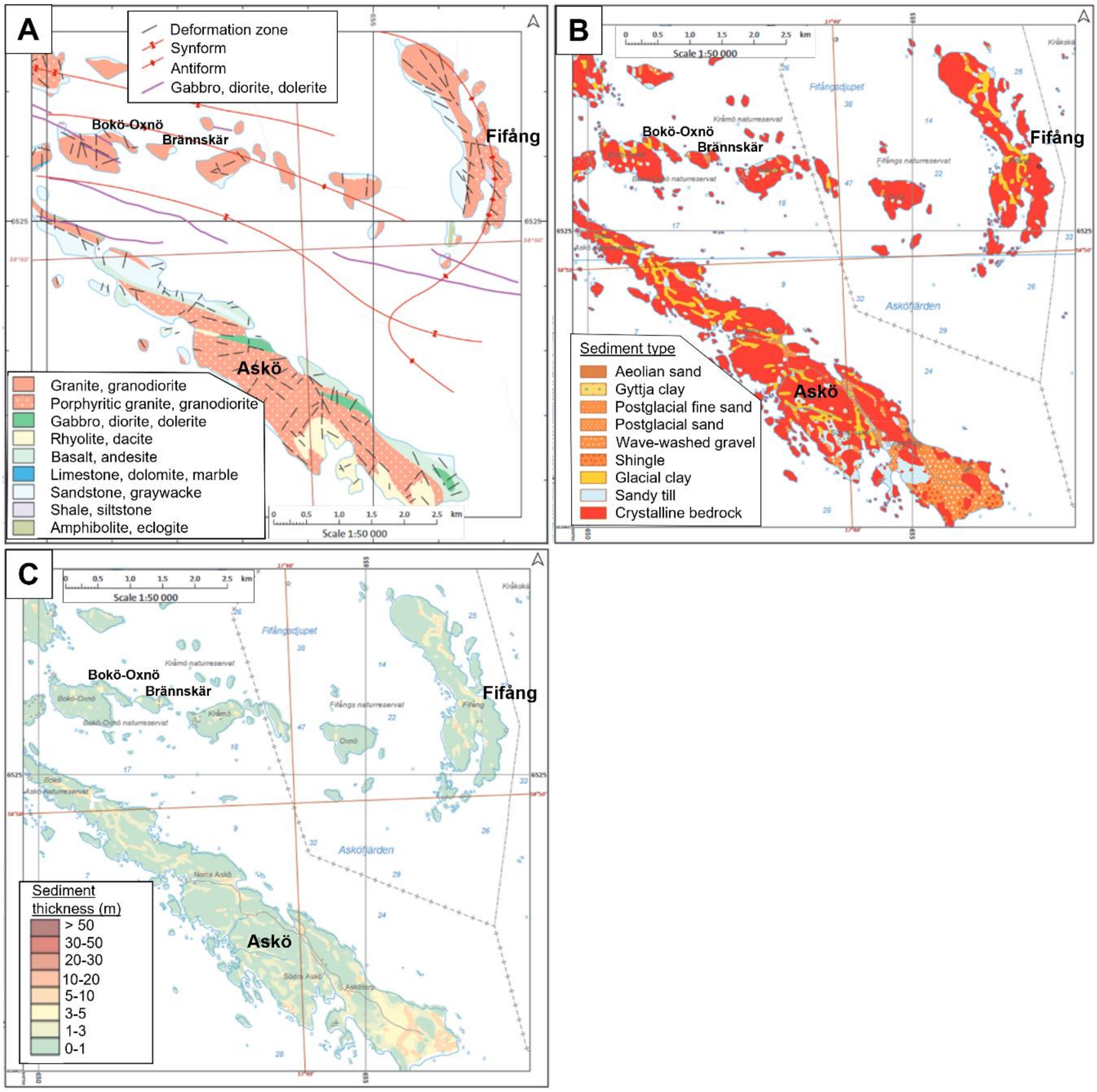

Figure 6. Bedrock and sediment of the islands in within the survey area. Apart from Fifång which is the main island of interest as the main research area is off its coast, Askö, Bokö-Oxnö and Brännskär are annotated with their names as they contain groundwater level information and are therefore of special interest compared to the other islands in the area. A: Bedrock map with deformation zones, antiforms, synforms and mafic intrusions presented. The islands mainly compose of granite and sandstone, with NW-SE and NNE-SSW to NE-SW trending deformation zones. Askö also contain rhyolite/dacite in the SW and more mafic rock types in NE, such as gabbro and basalt. B: Sediment type map showing the patchy presence of glacial sediment on all islands (sandy till and glacial clay) and also postglacial sediments on Askö. C: Sediment thickness map indicating that the sediment cover is between 1-20 m but with most of the sediment having a thickness of around 3-5 m or less. The maps are modified from SGU's map generator, 2021 (SGU). Coordinate reference system: SWEREF 99.

2.2. Geophysical mapping and core sampling

2.2.1. Acoustic geophysical mapping

Acoustic geophysical mapping techniques use reflecting acoustic pulses to create high resolution images of the bathymetry, sub-bottom stratigraphy and water column. Descriptions of acoustic geophysical mapping methods are, for example found in Lurton (2016) and Jakobsson et al., (2016). A brief summary is provided here using these references as source information. A pulse is sent from a transmitter and is reflected to a receiver upon interference with an object. The receiver registers the time-measured signal as a two-way travel time (TWT). Subsequently, the two-way travel time is converted into a depth (D) depending on the speed of sound in water or through the sediment (v) by the following equation:

$$D = v * \frac{TWT}{2} \tag{1}$$

At the interface between two geological mediums the acoustic signal is reflected due to the impedance contrasts of the materials (resistance of the acoustic wave to travel through the material). This produces images that reflect the properties of the bathymetry or sub-bottom sediments.

Multibeam echo sounders (MBES) use high frequency pulses and are mainly used for the mapping of the seafloor depth. MBES sends out several pulses in a sideways direction, which produces a 2D profile in the direction of the boat as well as to the sides of it. Sub-bottom profilers are used for imaging the subsurface sediment stratigraphy and operate using lower frequency pulses than MBES, allowing for deeper penetration into the subsurface. The sub-bottom profiler sends out acoustic pulses in one direction which produces 2D profiles along the boat tracks. Conventional sub-bottom profilers operate in one frequency while chirp sub-bottom profilers send out acoustic pulses in a sweep of varied frequencies: a bandwidth of frequencies. Thus, the chirp produces images of the sub-bottom with high resolution that can penetrate deeper into the sediment than when using conventional sub-bottom sonar systems. Resolution refers to the ability to resolve two objects or interfaces as separate entities, hence higher resolution systems can identify both smaller and more closely spaced features.

The horizontal resolution of a sonar system is determined by which is the largest of the footprint (D_f) or the radius of the First Fresnel zone (R_F). The footprint (D_f) corresponds to the horizontal area on the seafloor that is covered by a sound pulse (ping), and it depends on the water depth (H) and transducer opening beam angle in radians (α):

$$D_f = 2H\, x \tan\frac{\alpha}{2} \tag{2}$$

The First Fresnel zone is the area in which the soundwaves of the pulses interfere constructively (offsets between the pulses are ¼ of the wavelength or less) and its radius (R_F) is estimated using the water depth (H) and wavelength (λ):

$$R_F \approx \sqrt{\frac{H\lambda}{2}} \tag{3}$$

The vertical resolution of a chirp pulse (R_V) can be calculated based on the bandwidth of the sonar system (B) and the sound velocity (v):

$$R_V = \frac{v}{B/2} \quad (4)$$

Geophysical mapping was done with Stockholm University's R/V Electra, equipped with multibeam echosounder and sub-bottom profiler. Multibeam bathymetry and sub-bottom profiles were collected by Jakobsson, et al. (2020), and during annual courses held by Martin Jakobsson at Stockholm University between 2007 and 2018. Additional sub-bottom profiles were acquired in December 2020 across the terraces of interest for this project (Figure 5C). The multibeam bathymetry was acquired with a Kongsberg EM2040 0.4° × 0.7°, 200–400 kHz multibeam echo sounder, using a frequency of 400 kHz. Sub-bottom profiles were collected between 2007 and 2015 with an Edgetech SB-216S (17°-24°, 2-16 kHz) tow-fish chirp sonar, operating with 1 ms long 3–9 kHz pulses and towed at a 3 m depth. Between 2016 and 2020 the sub-bottom profiles were collected with a hull mounted Kongsberg Topas PS40 (3.5°-5°) 24-channel parametric sub-bottom profiler, operating in chirp mode with 4 ms long 4-10 kHz pulses. Due to the SB-216S being towed at a distance behind the ship (on which the GPS antenna is located) the position of the tow-fish is determined by accounting for the layback of the cable that connects it to the ship. Thus, the georeferenced profile from this system is less accurate than for the hull mounted sub-bottom profiler which is precisely referenced to the GPS on the ship. Photographs of the terraces in the core site were obtained during the expedition in December and 3D-digitized (courtesy to Jim Hansson, Swedish Maritime Museum).

2.2.2. Core sampling

Three cores were taken from three different terraces in the main research area (Figure 5C) using a piston corer for two cores (EL20-IGV07-1PC and 2PC) and a gravity corer for core (EL20-IGV07-3GC) (Table 1). The cores were cut into <1.5 m sections and taken to Stockholm University where they were kept in cold storage until usage. Core EL20-IGV07-1PC was opened and photographed during a laboratory exercise in the master's level Marine Geotechnics course at Stockholm University and the resulting images are used in this paper. Similarly, bulk density (ρ_B) and magnetic susceptibility (MS) of the cores were measured at 1 cm intervals on a Geotek Multi-Sensor Core Logger (MSCL). The MSCL data was used to identify key lithologic changes in the cores, choose sampling locations for consolidation tests, and for calculating the in-situ effective stress (σ'_v) and porosity (ϕ).

Core ID	**EL20-IGV07-1PC**	**EL20-IGV07-2PC**	**EL20-IGV07-3GC**
Coordinates core site	Lat 58.8373562352363, Lon 17.7031561210803	Lat 58.8373086597803, Lon 17.7029029701671	Lat 58.8372598762413, Lon 17.7022734354647
Corer	Piston corer	Piston corer	Gravity corer
Core length (m)	1.79	4	1
Section lengths (m)	Sec 1: 0-0.31, Sec 2: 0.31-1.79	Sec 1: 0-0.96, Sec 2: 0.96-2.48, Sec 3: 2.48-4	Sec 1: 0-1

Table 1. Specifications of the retrieved sediment cores, including coordinates, type of corer, core length and lengths of the cut sections of each core.

2.3. Geophysical data processing

2.3.1. Processing of the multibeam bathymetry data

The multibeam data in this project were processed and gridded by Martin Jakobsson, for details see Jakobsson et al. (2020). The gridded multibeam bathymetry was used for detecting terraces and for calculating sediment thicknesses.

2.3.2. Processing of the sub-bottom data

The sub-bottom raw data were stored in SEGY-format with the navigation in geodetic (latitude and longitude) coordinates in arc seconds. These spherical coordinates were projected into Universal Transverse Mercator (UTM) zone 33 cartesian (xy) coordinates, using the software tool GSCA SegY Navigation Converter version 1.2 (Geological Survey of Canada with courtesy of Bob Courtney). The projected coordinates were stored in the header of the converted SEGY-files, which were imported into OpendTect Pro (version 6.6.2, dGB Earth Sciences) for further processing and analysis (for details about OpendTect setup, see Appendix A). To import navigation data from the sub-bottom profiles to QGIS (version 3.16.11 Hannover) they were further converted into SHP-format by using software provided by the Geological Survey of Canada (with courtesy of Bob Courtney). The sub-bottom profiles from the Askö region were used to construct isopach maps defining the thickness of key sedimentary units. These were needed to assess the length/thickness of the sediments through which groundwater would need to travel under different scenarios.

2.3.3. Processing and analysis in OpendTect and QGIS

The sub-bottom profiles and multibeam bathymetry (having depths in two-way travel time) were imported into OpendTect using WGS 84/UTM zone 33N [EPSG:32633] projection of the coordinate system. The reference sea surface level recorded in the sub-bottom profiles varied slightly between the lines, causing a misalignment between the profiles with respect to depth. This is mainly an effect of the different transducer depths of the towed and the hull-mounted chirp sonar. Since the towed chirp is moving within the water column it operates at a deeper and fluctuating level, which was only accounted for during data acquisition by entering estimated depth values based on the amount of tow cable payed out, as the SB216 tow fish used lacked a pressure sensor (M. Jakobsson personal communication). The accuracy of the multibeam bathymetry depth is much higher, due to the multibeam having a higher resolution than the sub-bottom profiler and the fact that it is fully compensated for ship motions and sound-velocity variations through the water column. In addition, the GPS navigation was RTK-corrected implying a horizonal accuracy of about 2-3 cm. Therefore, each sub-bottom profile was depth-adjusted to match the seafloor level of the multibeam bathymetry. This was done visually in OpendTect by comparing the seafloor of the sub-bottom profiles with the bathymetry. As the offsets in depth can vary along one profile (with the location of the towed chirp varying along a line), the adjustments were averaged along each profile.

To enhance the visualization of the acoustic stratigraphic layers, an *Instantaneous amplitude attribute* filter was added to all sub-bottom profiles. All seismically driven parameters are attributes, such as velocity, amplitude and frequency, and by applying a certain attribute filter to the profiles, specific features which are sought for are intensified . The Instantaneous amplitude attribute enhances the visibility of the acoustic impedance contrasts or *reflectors* and was therefore chosen.

The prominent reflectors of each sub-bottom profile were manually digitized and labelled according to their vertical position in the upward stratigraphic sequence. The layer between two prominent reflectors is considered an *acoustic unit*. A gridded surface of each reflector was generated by interpolating along and between the digitized reflectors with the OpendTect plugin “Grid 2D-3D horizon” using a Local Thin Plate Spline (LTPS) algorithm (as this algorithm produced a seabed surface with the best fit to the bathymetry. LTPS is an algorithm which can be used for interpolation and smoothing of scattered data , which works well for this project as the sub-bottom lines were sparse at places. All gridded surfaces were cropped along the borders of the multibeam bathymetry since sub-bottom lines were adjusted vertically to it and because the bathymetry was to be used for isopach calculations- hence only areas corresponding to the bathymetry should be used.

The sediment thickness in time (ms), isochrons, of the acoustic units between the gridded surfaces was obtained using an assumed constant sound speed of 1500 m/s. This sound speed is a simplification as it varies between the water column and within the sediments (Jakobsson, et al., 2016). With respect to the sediments, 1500 m/s is likely a minimum value implying that calculated thicknesses are “minimum thicknesses”. The isochrons and multibeam bathymetry were imported into QGIS (version 3.16.11 Hannover), where the depths of the surfaces were converted from time (ms) to distance (m) (Equation 1). Lastly, both bathymetry maps and isopach maps (thickness in meters) of the key sedimentary units were created in QGIS (version 3.16.11 Hannover).

2.4. Physical Properties and Geotechnical testing of sediment cores

2.4.1. Consolidation Tests

One-dimensional incremental load consolidation tests were performed on 7 samples from EL20-IGV07-2PC following the ASTM standard method (D2435-04 Method B) . Whole-round samples of 3-5 cm thickness were cut from the unopened core at locations where the MSCL data showed differences in bulk density, magnetic susceptibility, and porosity (Table 2). The samples were trimmed to fit a fixed ring oedometer cell with a height of 20 mm and inner diameter of 50.4 mm (Figure 7A). Two samples were prepared from EL20-IGV07-2PC-SEC 2-147-152. Trimmings from each sample were used for grain density measurements. Filter papers were placed both underneath and on top of the sample before being placed between the porous stones in the oedometer cell. The porous stones were always kept saturated in distilled water during the preparations of the samples, and distilled water was used to fill the oedometer cell. Tests were performed using an Loadtrac 2 load frame with a load capacity of 45 kN but a load cell with a 4500 N limit (Figure 7B) and FlowTrac 2 Pressure and volume control flow pump with a pressure capacity of 3500 kPa (Geocomp Corporation, MA, USA). Incremental load steps with a Load Incremental Ratio of 1 (doubling of the load for each step), from 2 kPa to 2050 kPa, were performed. The end of each step was reached at 90 % primary consolidation, after a minimum duration of 2 hours or maximum time of 24 hours. The time required to reach the end of primary consolidation (t90) as well as the corresponding vertical displacement was determined by the software, based on the *square root of time method* . Unloading of the sample occurred at the same load increments until 2 kPa, when the test was ended. The samples were weighed before and after consolidation test. The consolidated sample and trimmings from sample preparation were dried in the oven at 55°C for a minimum of 2 days and used to calculate the water content before and after consolidation.

2.4.2. Grain size and grain density measurements

Grain size measurements were made on subsamples from the wet consolidated samples using a Malvern Mastersizer 3000 laser diffraction particle size analyzer. The particle sizes were defined based on the Wentworth classification system as follows: Clay: 0–4 μm, silt 4–63 μm, sand > 63 μm .

To calculate the porosity/void ratio of samples, grain density (ρ_G) measurements were performed with a helium gas pycnometer (Micromeritics, AccuPyc 2, 1340). This was done by crushing 8-12 g of the dried trimmings from the consolidation test sample with a pestle and mortar and filling it in a 6.37 cm^3 sample cup, leaving 5 mm to the top. Each sample was measured five times and the resulting average grain density was reported with a standard deviation.

Core	EL20-IGV07-2PC						
Sample ID	EL20-IGV07-2PC-SEC 3-136-142	EL20-IGV07-2PC-SEC 3-130-136	EL20-IGV07-2PC-SEC 3-120-125	EL20-IGV07-2PC- SEC 2-147-152-A	EL20-IGV07-2PC- SEC 2-147-152-B	EL20-IGV07-2PC-SEC 2-4-7	EL20-IGV07-2PC-SEC 2-0-3
Core section	3	3	3	2	2	2	2
Core depth (m)	3.88	3.81	3.71	2.46	2.46	1.03	0.99

Table 2. Locations of where the samples used for geotechnical tests were taken from core EL20-IGV07-2PC.

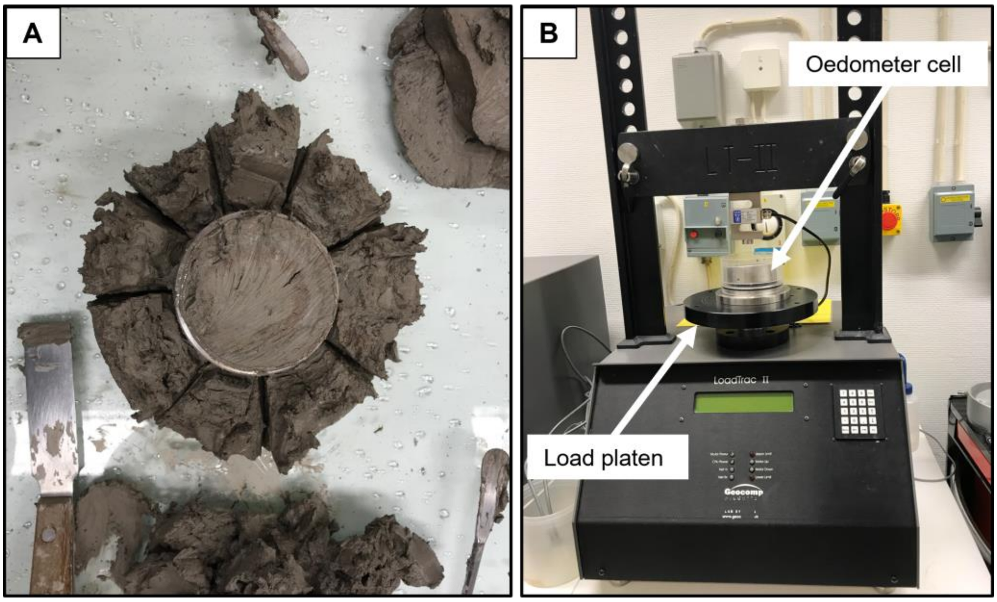

Figure 7. Consolidation test components. A: Sample preparations of trimming and fitting the samples into the fixed ring cell (20x50.4mm). B: Loadtrac 2 load frame with the following features pointed out: oedometer cell containing the sample specimen, load platen which moves upwards to increase the pressure, pressure sensor which is connected to the Flowtrac 2 system.

2.5. Data reduction and processing steps of geotechnical data

From the consolidation tests the change in void ratio (e) and hydraulic conductivity (k) during increased effective stress (σ'_v) was obtained (data reduction details in Appendix B), and from void ratio the sample porosity (ϕ) was derived with the following relationship:

$$\phi = \frac{e}{e+1} \tag{5}$$

2.5.1. Pre-consolidation pressure, compression, and recompression indices

Each consolidation test was plotted as a *consolidation curve* on a log void ratio (e) – log effective stress ($\sigma' v$) graph to graphically determine the pre-consolidation pressure (σ'_p), compression index (C_c) and recompression index (C_r) (Figure 8). The pre-consolidation pressure and compression index is needed for producing an in-situ depth-porosity model of the sediment as well as to know if the sediment is over consolidated (was buried to a deeper depth in the past).

The consolidation curve consists of lines that connect void ratio at the end of each loading step, with the consolidation path starting at point A and ending at point E (Figure 8). The initial loading, or *reloading* (as the sediment is being reloaded after having been taken up from the seafloor) of the sediment is represented by the *recompression curve* between point A and B (Figure 8). A line fitted along the initial load steps of the recompression curve represent the *recompression line* and its slope is the *recompression index (C_r)* . During recompression, the void ratio changes little with the increased load steps until the recompression curve is interrupted by a break and a distinct downwards slope in the curve between point B and C (Figure 8). At the break of the curve the sediment is subjected to loads that exceed the maximum effective stress that the sediment has ever experienced. This is termed the *pre-consolidation pressure (σ'_p)*. This break represents the change from recompression to compression of the sediment. The path of the curve after the pre-consolidation pressure, between point C and point D, is called the *Virgin Compression Line (VCL)* and its slope is the *Compression index (C_c)*. The VCL represents how the void ratio decreases with increased effective stress, it essentially represents the void ratio/porosity-depth function of the sediment. The unloading part of the curve is shown between D and E and corresponds to the load decrease until the end of the test at point E. By extending the VCL upwards to meet the y-axis, the void ratio upon initial sediment deposition (e_0), at an effective stress of 1 kPa, is obtained (Figure 8).

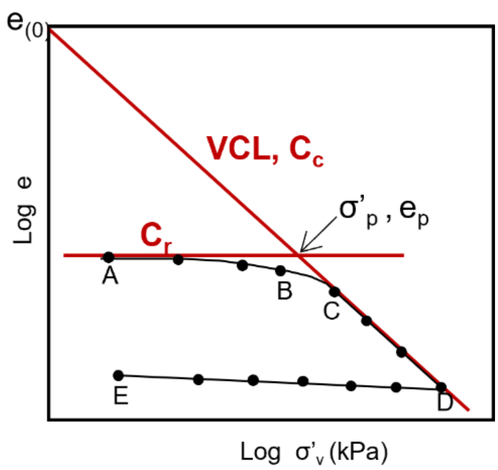

Figure 8. Illustration of a textbook-example consolidation curve with an arbitrary number of load steps shown as points on the curve. Point A-B: The path of the recompression curve, onto which the recompression line and recompression index (C_r) is fitted. B-C: Break between recompression and compression part of the curve from which the pre-consolidation pressure (σ'_p) and the void ratio at the pre-consolidation pressure (e_p) is shown. C-D: Virgin compression line (VCL) and its corresponding slope, the compression index (C_c). D-E: Unloading of the effective stress until the end of the test at point E.

2.5.2. Effective vertical stress and downcore porosity from the MSCL data

When saturated sediments are compressed under hydrostatic pore pressure conditions, the stress consolidating the sediments is a function of the buoyant weight of the overlying sediments and is called the *effective vertical stress* (σ'_v). From the MSCL bulk density (ρ_B) (g/cm^3) a downhole profile of in-situ effective vertical stress in kPa (σ'_v) (assuming no excess pore pressure and a fluid density (ρ_f) of 1 g/cm^3) was calculated for each core:

Since the vertical effective stress is defined as:

$$\sigma'_v = (\rho_B - \rho_f)gz \tag{6}$$

$where\ g = gravity\ acceleration\ (m/s^2)\ and\ z = depth\ (m)$

The downcore effective stress profiles between closely spaced bulk density measurements can be calculated as:

$$\sigma'_{v2} = \sigma'_{v1} + (\rho_{B1} g \Delta z) - (\rho_f g \Delta z) \tag{7}$$

$where$
$\sigma'_{v2} = effective\ stress\ at\ the\ new\ depth\ (kPa)$
$\sigma'_{v1} = effective\ stress\ at\ previous\ depth\ (kPa)$
$\rho_{B1} = bulk\ density\ at\ previous\ depth\ (g/cm3)$
$\Delta z = change\ between\ previous\ depth\ (z_1)\ and\ new\ depth\ (z_2)\ (m)$

The in-situ effective stress was compared with the pre-consolidation pressure for each sample to determine its stress history or overconsolidation ratio.

Downcore porosity (ϕ) was calculated from the measured MSCL bulk density (ρ_B) following:

$$\phi = \frac{\rho_G - \rho_B}{\rho_G - \rho_f} \tag{8}$$

Where the grain density (ρ_G) (g/cm^3) for core 2PC was the average values obtained from the pycnometer measurements and for core 1PC and 3GC an assumed grain density of 2.73 g/cm^3 was used. The pore fluid density (ρ_f) was assigned a value of 1 g/cm^3.

2.5.3. Overconsolidation ratio (OCR)

The stress history for each sample was described using the *overconsolidation ratio (OCR)*, which is the ratio between the pre-consolidation pressure (σ'_p) and the corresponding MSCL derived in-situ effective stress (σ'_v):

$$OCR = \frac{\sigma'_p}{\sigma'_v} \tag{9}$$

Because sediments compress differently depending on their consolidation state, modelling in-situ depth-porosity profiles require knowledge of the overconsolidation ratio. If the in-situ effective stress of the sediment is experiencing the highest load it has ever been subjected to, the sediment is *normally* consolidated and the OCR = 1. If the in-situ effective stress is lower than the past maximum effective stress ($\sigma'p > \sigma'_v$) it is *overconsolidated* with an OCR > 1. If the existing in-situ effective stress is higher than the pre-consolidation pressure the sediment is *underconsolidated* ($\sigma'p < \sigma'_v$) and the OCR < 1. Underconsolidation implies that the porewater pressure is higher than the hydrostatic pressure and that excess pore pressure exists.

3. Results

3.1. Geophysical mapping and data processing

3.1.1. Bathymetry

The seafloor depth along the coasts of Askö and Fifång is between 10-20 m and deepens further offshore toward the middle of the mapping area, with depths up to 55 m (Figure 9). At water depths around 15 m, where most terraces are located (Figure 5), the across track resolution of the multibeam (based on the transmitter angle of 0.7°) gives a footprint of 0.18 m, and the along track resolution (based on the receiver beam angle of 0.4°) gives a resolution of 0.1 m (Equation 2). Meanwhile, at the same average depth of 15 m, the Fresnel zone radius is 0.17 m (Equation 3), which gives a diameter of 0.34 m. Thus, the horizontal resolution is dictated by the Fresnel zone as it is larger than the footprint, and only objects larger than 0.34 m can be detected by a single pass of the used EM2040 multibeam sonar.

Core EL20-IGV07-1PC and EL20-IGV07-2PC were collected from two adjacent terraces with steps facing away from Fifång, while core EL20-IGV07-3GC belongs to a terrace opposite the other two, which faces inland (Figure 9B). The terraces are situated at water depths between 16 and 18 m (Figure 9B) with distances of 310 m (core EL20-IGV07-1PC), 325 m (core EL20-IGV07-2PC) and 360 m (core EL20-IGV07-3GC) to the shore of Fifång (Figure 9C). The heights of the terrace steps are 0.5 to 1 m (Figure 10), consistent with findings of Jakobsson et al. (2020) who concluded that terraces mainly occur at water depths of around 15-16 m with steps that usually are <1 m high. A 3D-digitized photograph (obtained from the expedition in December 2020, courtesy to Jim Hansson, Swedish Maritime Museum) of the terrace from where core 2PC was obtained, reveal holes in the terrace walls and sediment debris in front of the terrace (Figure 11). These features clearly resemble the descriptions of the terraces put forward by Söderberg and Flodén. (1992, 1997) and Jakobsson et al. (2020).

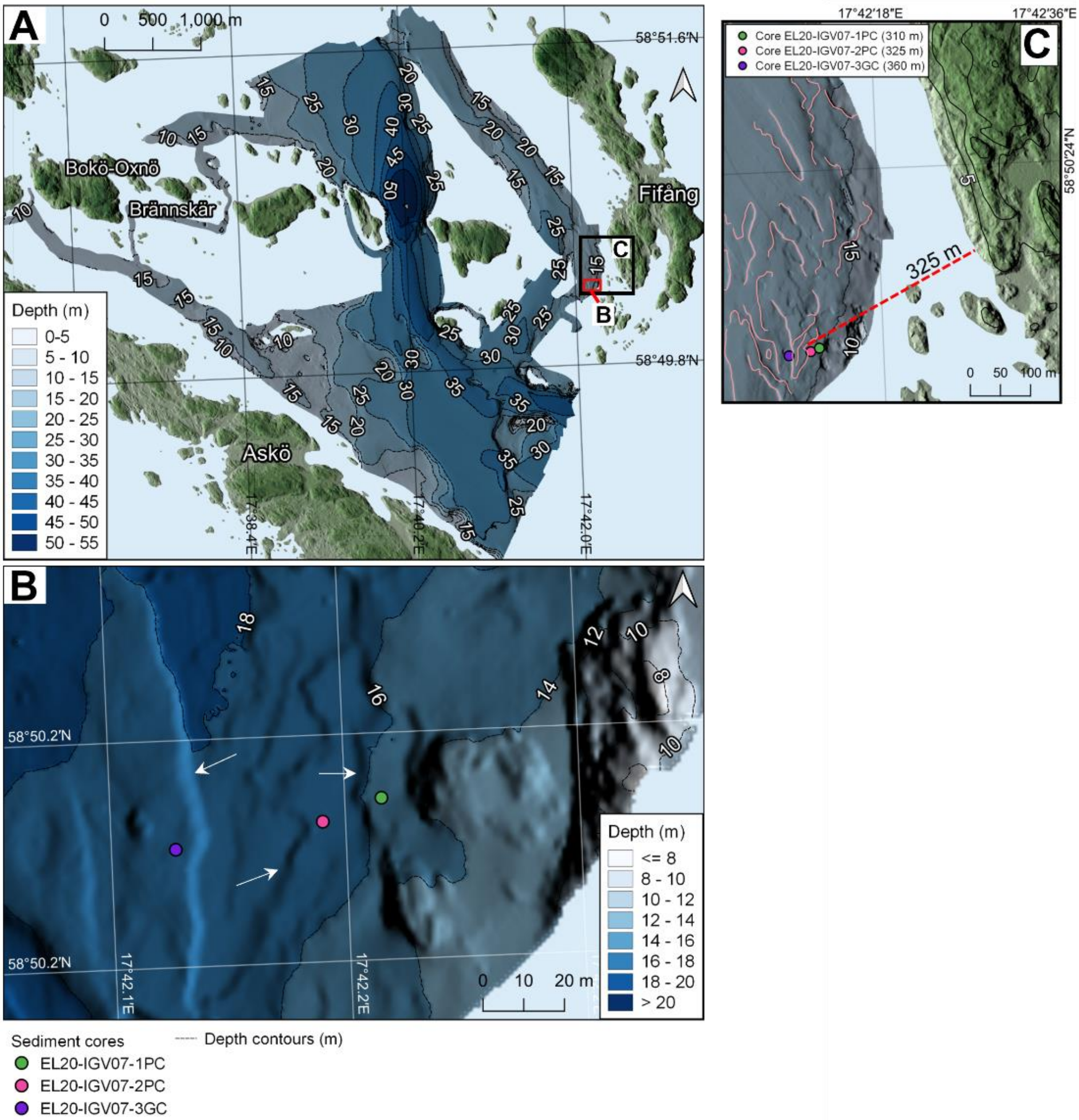

Figure 9. Multibeam bathymetry of the survey area. A: Overview of the mapped survey area showing the depths (m) with 5 m intervals. B: The core site with the terraces from which the cores were retrieved indicated with white arrows. C: The location of the core site with respect to Fifång shore showing the distance to core EL20-IGV07-2PC. Pink noodle-shaped lines show the locations of terraces in the area mapped (M. Jakobsson). Coordinate reference system: WGS 84/UTM zone 33N.

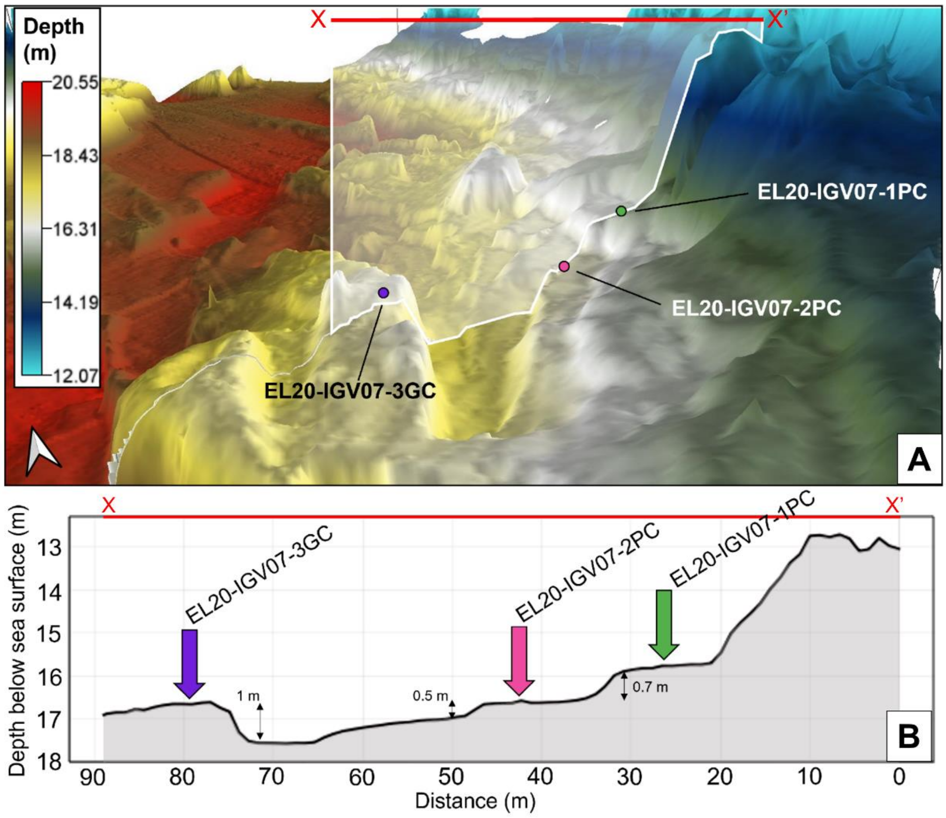

Figure 10. The terraces where the three sediment cores were retrieved. A: The terraces as viewed from the multibeam bathymetry in OpendTect Pro (version 6.6.2, dGB Earth Sciences). The location for the cross-section in (B) is viewed across the core sites. B: Cross-section of the terraces in line with the core locations, showing the height (m) of each terrace step (produced in QGIS version 3.16.11 Hannover).

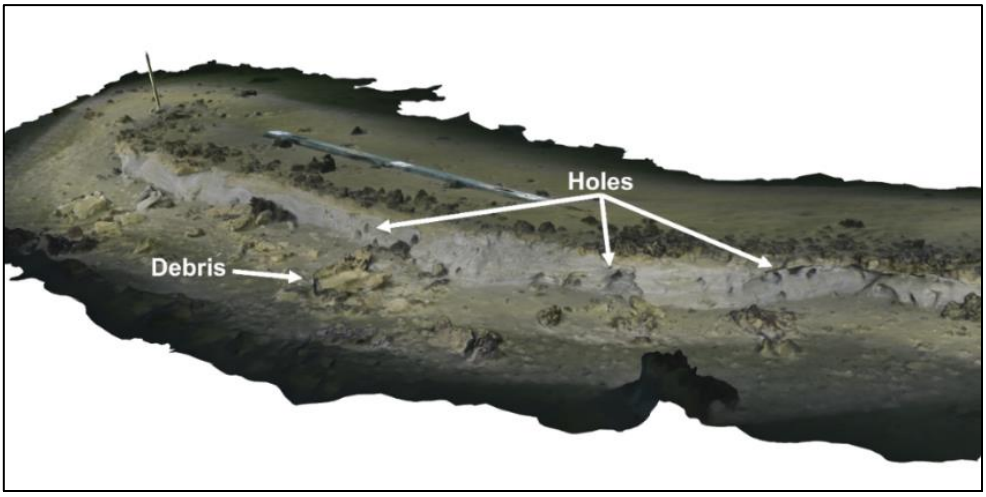

Figure 11. 3D-digitized photograph of the terrace from which core EL20-IGV07-2PC was retrieved (Jim Hansson, Swedish Maritime Museum). Holes within the terrace wall and debris in front of the wall correspond to the descriptions and photographs of terraces from previous studies by Söderberg and Flodén. (1992, 1997) and Jakobsson et al. (2020).

3.1.2.1. Sub-bottom profiles

A total of 115 sub-bottom profiles were analyzed for the purpose of interpreting the stratigraphy and creating isopach maps of the acoustic units in the survey area (Figure 12). The sub-bottom sediments off the west coast of Fifång island were mainly mapped during 2010, 2016, 2017, 2018-09 and 2020 (Figure 12A) and the terraces from which the three sediment cores were retrieved are only covered by sub-bottom profiles from 2016, 2017 and 2020 (Figure 12B).

The vertical resolutions (R_v) acquired with both the Topas PS40 chirp (4-10 kHz) and SB-216S chirp (3-9 kHz) is 0.5 m as the bandwidths of the systems are the same (Equation 4). This means that any vertical change smaller than 0.5 m will not be detected. Consequently, some terraces will not be detected in the sub-bottom profiles. The horizontal resolution for the Topas PS40 chirp, at a water depth of 15 m, is dictated by the 1st Fresnel zone (= 2.1-3.4 m, Equation 3), as it has relatively narrow beam widths for the primary and secondary frequencies of 3.5° and 5° respectively, which gives footprints of 0.9 and 1.3 m (Equation 2). However, for the SB-216S chirp, the footprint dictates the horizontal resolution as the beam width ranges from 17° to 24°, yielding resolutions of 4.5 m to 6.3 m respectively (Equation 2), while the 1st Fresnel zone is between 1.7 and 4.7 m (Equation 3). As the Topas PS40 was used for mapping from 2016 and onwards, any horizontal changes in the stratigraphy of these sub-bottom profiles that are smaller than ca 2 m in 15 m water depths will not be detected. The sub-bottom profiles collected prior to 2016 was collected with the SB-216S chirp which means that the smallest object that are horizontally detectable within these profiles are 4.5 m (Figure 12A).

3.1.2.2. Acoustic reflectors and acoustic units

Five prominent acoustic reflectors (R-1 to R-5) were defined in the sub-bottom profiles, including the interface to the acoustic basement (R-1) and the seafloor (R-5). The space between each reflector represents an acoustic unit, with Unit 1 being the lowermost one and Unit 4 the shallowest one (Figure 13).

R-1 is a reflector caused by a strong impedance contrast between the acoustic basement and the overlying sediments. Below R-1 there are generally no "real" reflections as the sound waves do not penetrate through the acoustic basement. However, "multiples", artefacts caused by the acoustic wave being reflected multiple times between two impedance layers before returning to the receiver of the sonar (Jakobsson, et al., 2016), are commonly occurring within the acoustic basement (Figure 13).

Unit 1 is the thickest unit in the stratigraphy and is acoustically stratified throughout the unit (Figure 13). In areas where there are depressions in the acoustic basement, Unit 1 is overlain by other acoustic units, but where the acoustic basement protrudes towards the surface, the other units are often absent resulting in Unit 1 outcropping at the seafloor (Figure 13). Blank areas extending upwards from the acoustic basement are common and appear to be bound to Unit 1 (Figure 13, Figure 14 and Figure 15). The terraces in the survey area consistently occurr in acoustic Unit 1 where the unit outcrops at the seafloor and often coincide with the presence of the vertically oriented blank zones (Figure 15).

The transition from Unit 1 to Unit 2 is represented by a strong impedance contrast (R-2) and a lower intensity of the internal reflections (Figure 13). The acoustic stratifications of Unit 2 are often faint (Figure 13) but can be clearly visible in sub-bottom profiles with high quality, which sometimes complicates distinguishing between Unit 1 and Unit 2 (Figure 14). The thickness of Unit 2 is mostly around 2-3 m. The top of the unit is traceable by R-3, a strong reflector that often blurs out along the sediment profile (Figure 13 and Figure 14).

Unit 3 is often double or three times thicker than Unit 2 and commonly contains weak internal acoustic stratifications in the bottom half of the unit, followed by a homogenous appearance absent of internal reflections (Figure 13). R-4 commonly marks a sharp acoustic impedance change between Unit 3 and

Unit 4 (Figure 13) but is not always present in the sub-bottom profiles. Consequently, Unit 4 does not appear in all profiles and usually exists where there is a depression in the acoustic basement accompanied by a generally thick sediment cover. Unit 4 is usually the thinnest unit (< 2 m) and generally never contains internal reflections. R-5 represents the topmost reflector of the seafloor (Figure 13).

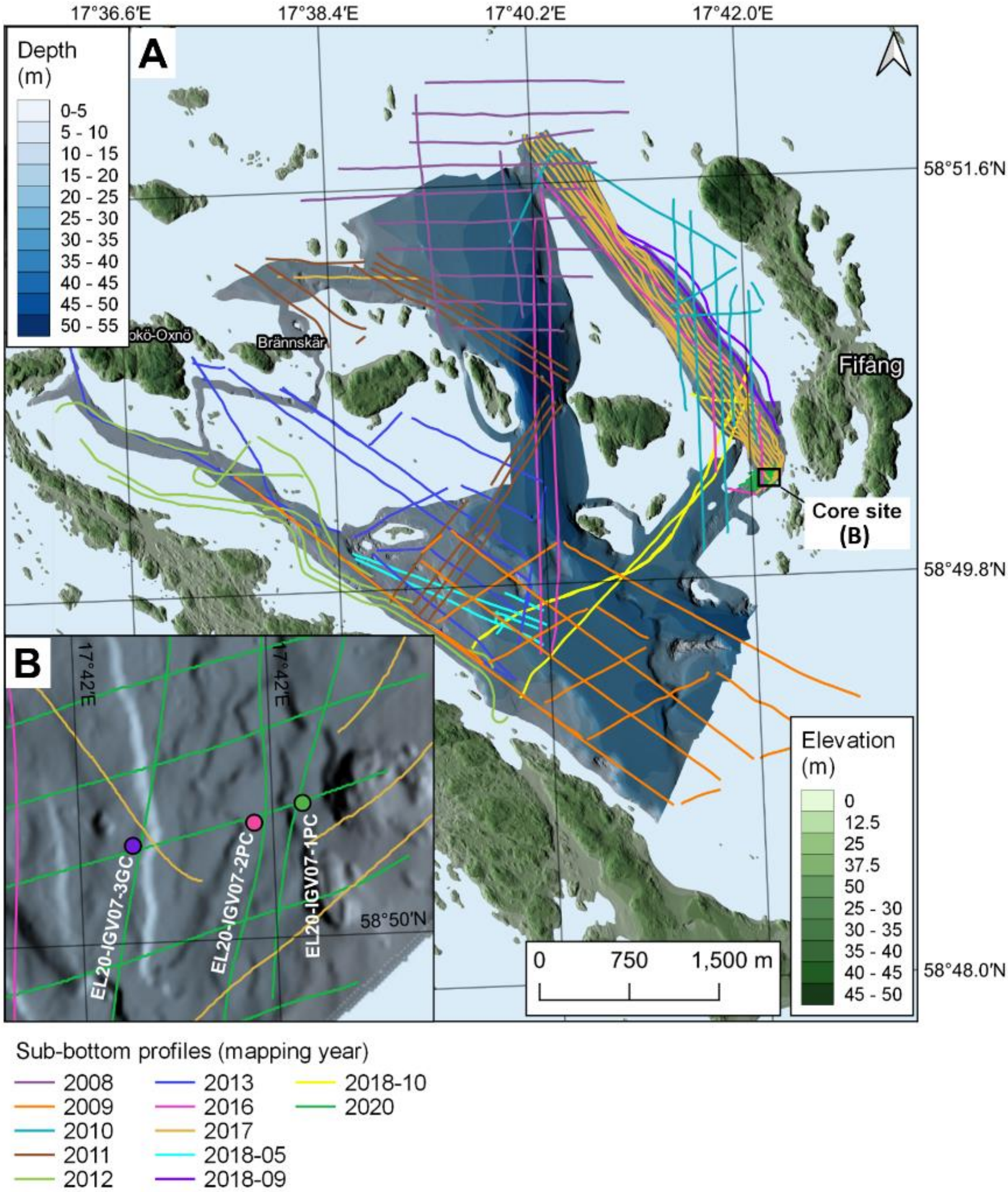

Figure 12. Map of the multibeam bathymetry and locations of the sub-bottom profiles. A: Overview of the survey area showing the bathymetry and elevation of the islands (DTM, grid 1 © Lantmäteriet, 2021) and the sub-bottom profiles in colors according to the year of mapping. Sub-bottom profiles are most frequently mapped off the shores of Askö and Fifång. B: Close-up of the core site and the terraces from which the sediment cores were retrieved. The sub-bottom profiles collected during 2020 mainly cover the terraces, and to a lesser extent the profiles from 2017 and 2016. Coordinate reference system: WGS 84/UTM zone 33N.

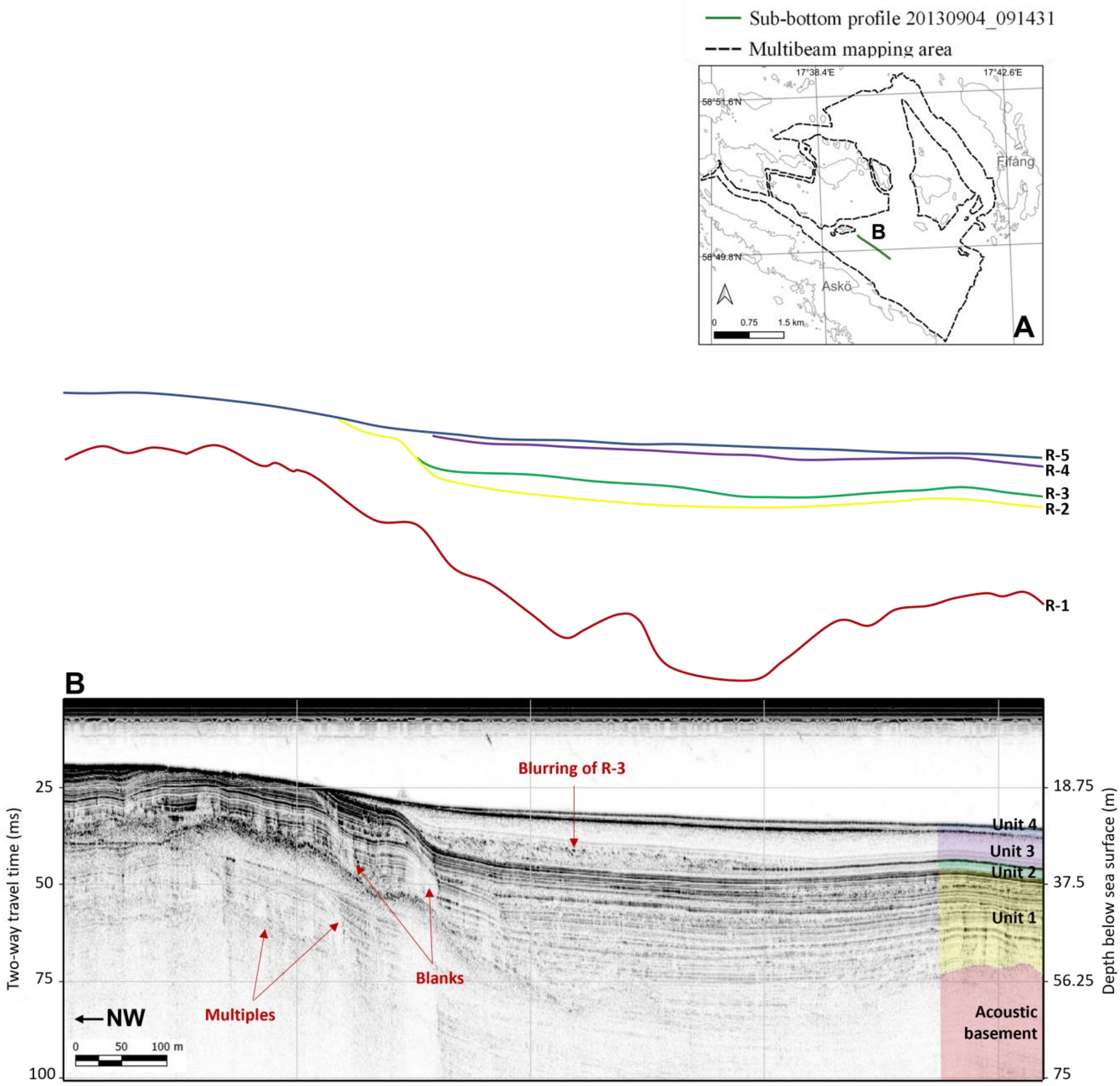

Figure 13. Sub-bottom profile 20130904_091431 with its mapping location shown in A and its cross-section shown in B. In B all digitized reflectors (R-1 to R-5) and acoustic units (Unit 1 to Unit 4) are illustrated. Multiples are shown in the acoustic basement, blanks in the sediment are constrained to Unit 1 and blurring of R-3 is visible at the interface between Units 2 and 3.

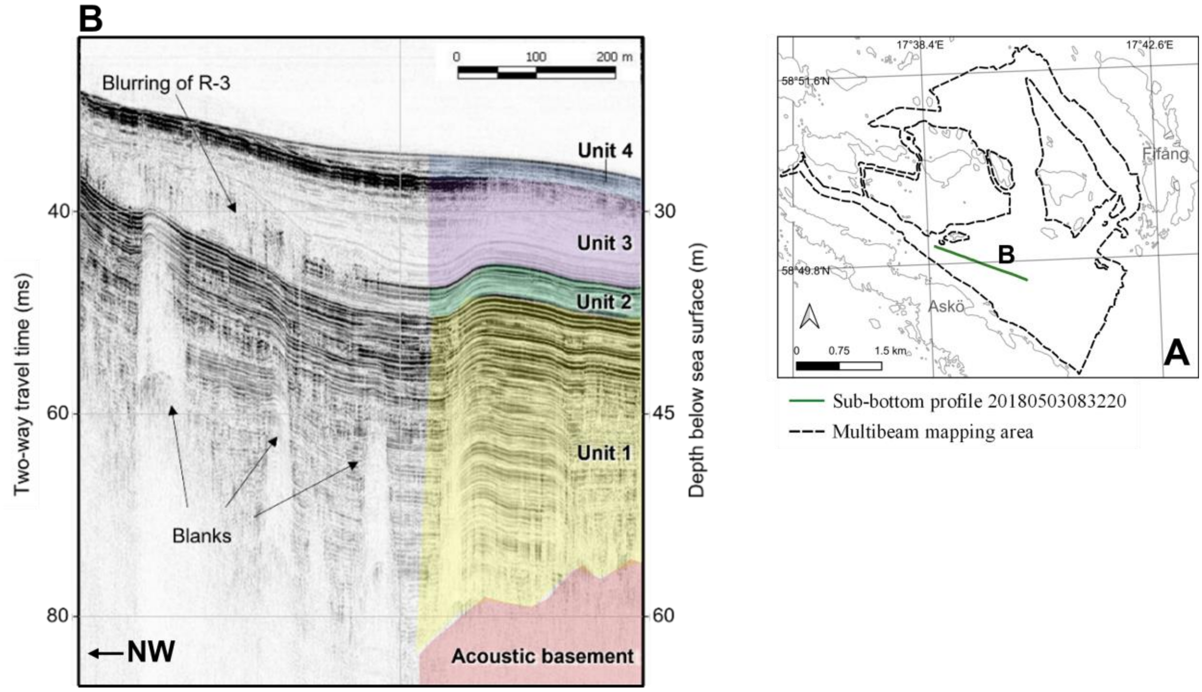

Figure 14. Sub-bottom profile 20180503083220 showing all acoustic units as well as blanks in Unit 2 and blurring of reflector 3 (R-3). Unit 2 contains visible acoustic stratifications which resemble those of Unit 1 and Unit 3 contain internal reflections in the bottom of the unit. A: Mapping location of the profile. B: Sub-bottom profile.

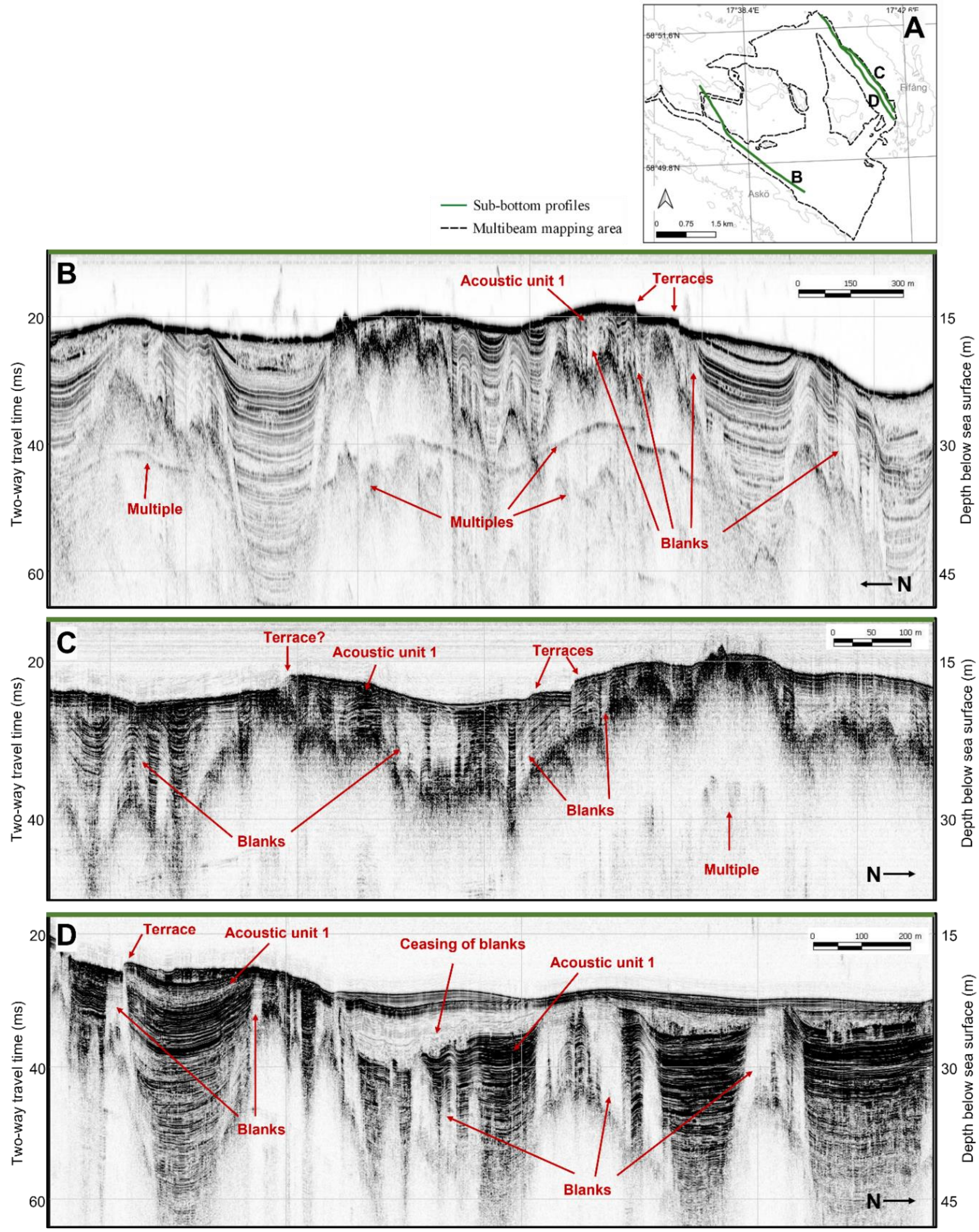

Figure 15. Three sub-bottom profiles obtained from along the coasts of Askö and Fifång showing terraces at the sea floor within acoustic Unit 1 and the presence of vertically ascending blanks in the acoustic stratigraphy of Unit 1. Any terraces < 0.5 will not be detectable due to the chirp profiler vertical resolution of 0.5 m. A: Location of the sub-bottom profiles (B-D) in the mapping area. B: Sub-bottom profile 20130904_105339, showing two distinct terraces facing south-eastwards. C: Sub-bottom profile 20180911091418 with terraces facing southwards. D: Sub-bottom profile 20170905114251 illustrating that the blanks are constrained to acoustic Unit 1 as they are undetected in the units above.

3.1.3. Gridding surfaces of acoustic units

Gridding of the digitized reflectors (R-1; R-5) produced surfaces (S-1; S-5) that represent the transition between each acoustic unit, with S-1 being the top of the acoustic basement, S-2: the top of Unit 1, S-3: top of Unit 2, S-4: the top of Unit 3 and S-5: the top of Unit 4 and/ or the seafloor (Figure 16A-C). The LTPS algorithm produced a surface that fitted the multibeam bathymetry best (Figure A1). However, a shortcoming of this gridding algorithm in OpendTect is that it interpolates between reflectors with no regard to the length of the distance between them, or if there are other (different) crossing reflectors in between (Figure 16D). Thus, some surfaces were not constrained enough during gridding as their corresponding reflectors did not appear continuously throughout the mapped area, leading to the gridded surfaces ending up where they do not exist (Figure 16D). This was particularly evident for S-3 and S-4 as they are interpolated from reflectors that occur sparsely in the area. Therefore S-3 and S-4 were excluded from further calculations of isopach's, thus, the only surfaces used for isopach calculations were S-1, S-2 and the multibeam bathymetry (Figure 17).

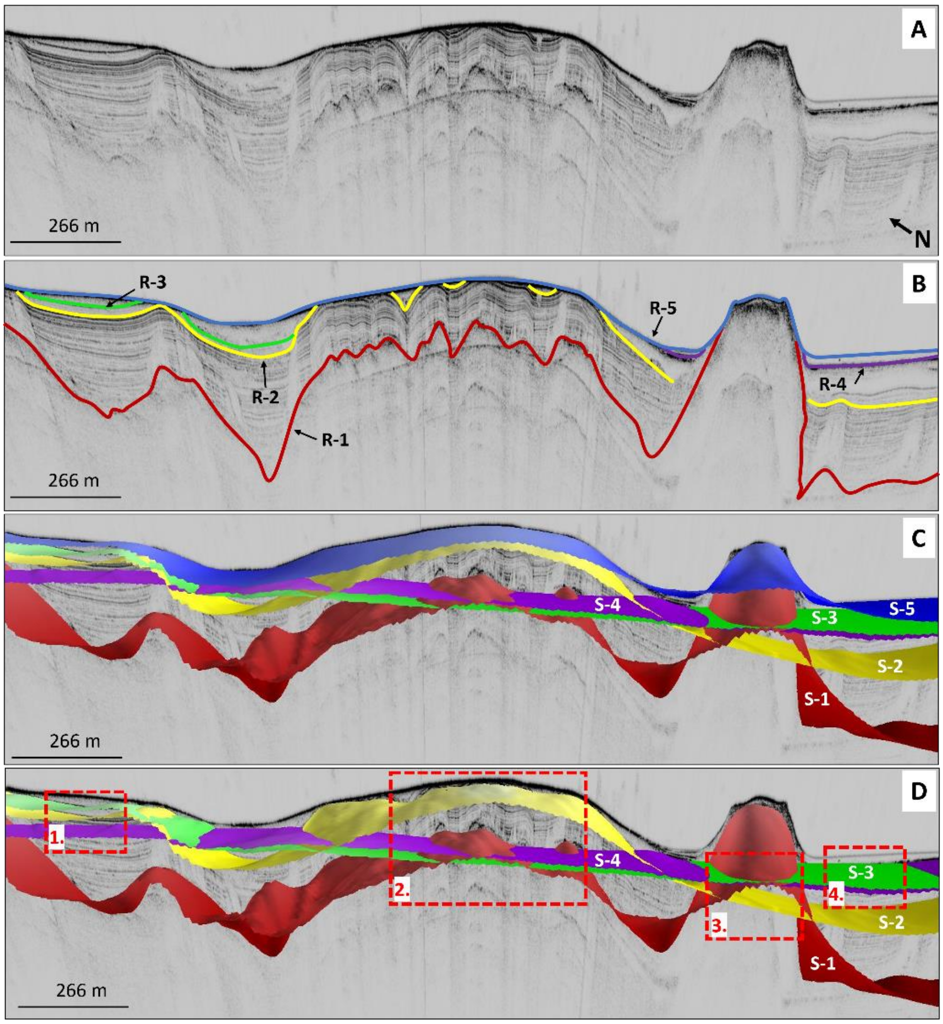

Figure 16. The digitized reflector lines and LTPS gridded surfaces within the sub-bottom profile 98260927 (2009) showing that interpolation between sparsely placed digitized reflectors can result in inaccurate surface grids of the units. A: Sub-bottom profile without interpretations. B: The digitized reflectors R-1 to R-5. C: The gridded surfaces (S-1 to S-5) of the interpolated reflectors (R-1 to R-5). D: The red boxes highlight the distorted surface grids of this sub-bottom profile due to the unconstrained interpolation between reflectors. Box 1: S-4 appears below S-2 and S-3 when it should be located above both in the stratigraphic sequence. Box 2: S-3 and S-4 have been inaccurately gridded below both S-2 and S-1. Box 3: S-2, S-3 and S-4 all grid below the acoustic basement (S-1). Box 4: S-3 is gridded above S-4.

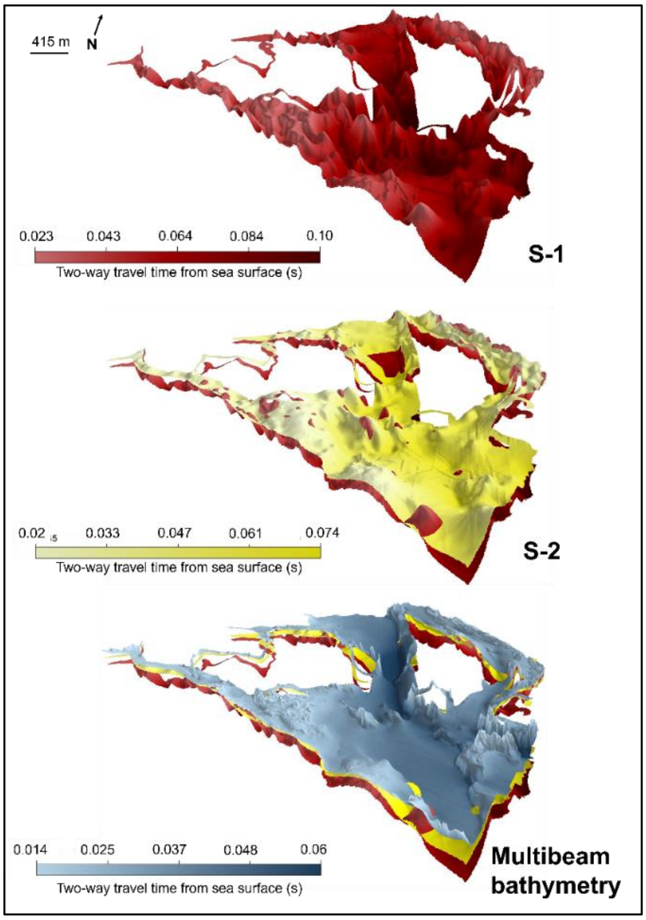

Figure 17. The gridded surfaces of the acoustic units used for isopach calculations. S-1 is the gridded reflector R-1 and corresponds to the acoustic basement. S-2 is the gridded reflector R-2 and marks the surface of Unit 1. Between S-2 and the multibeam bathymetry the digitized reflectors R-3 and R-4 have been excluded due to the poorly gridded surfaces from sparse data.

3.1.4. Isopach maps

Isopach calculations were done between: S-1 and the multibeam bathymetry, which corresponds to the total sediment thickness (Figure 18A); between S-2 and the multibeam bathymetry, which allows acoustic Units 2, 3 and 4 to be represented as one (Figure 18B); and between S-1 and S-2, corresponding to acoustic Unit 1 (Figure 18C). Thus, the isopach of the combined acoustic Units 2, 3 and 4 corresponds to the difference in sediment thickness between the other two isopach's.

Isopach maps of the mapping area between Askö and Fifång

All isopach maps show a thinner sediment cover closer to Askö and Fifång, while increasing toward the deeper waters (Figure 18A-C, Figure 9A). The total sediment thickness (Figure 18A) and the thickness of acoustic Unit 1 (Figure 18C) are similar close to the islands (0-15 m) while differing by 10-20 m in the deep waters, evidently meaning that the combined Units 2, 3 and 4 are deposited mainly in the deeper waters (Figure 18B). However, as the most extensive sub-bottom mapping has been made along the coasts of northern Askö and Fifång there are parts of the survey area which lack constraining data (Figure 18D). An example of this is illustrated in Figure 18A where the thickest sediment of ~ 55-70 m occur in an area without mapped sub-bottom profiles, meaning that the thickest sediment is an artifact from gridding. Additionally, many of the more offshore sub-bottom profiles have been disturbed by blanks (Figure 18D) and therefore the surrounding areas have been interpolated with a higher degree of uncertainty. This adds some uncertainty to the deep-water sediment thicknesses. For enlarged isopach maps see Appendix C.

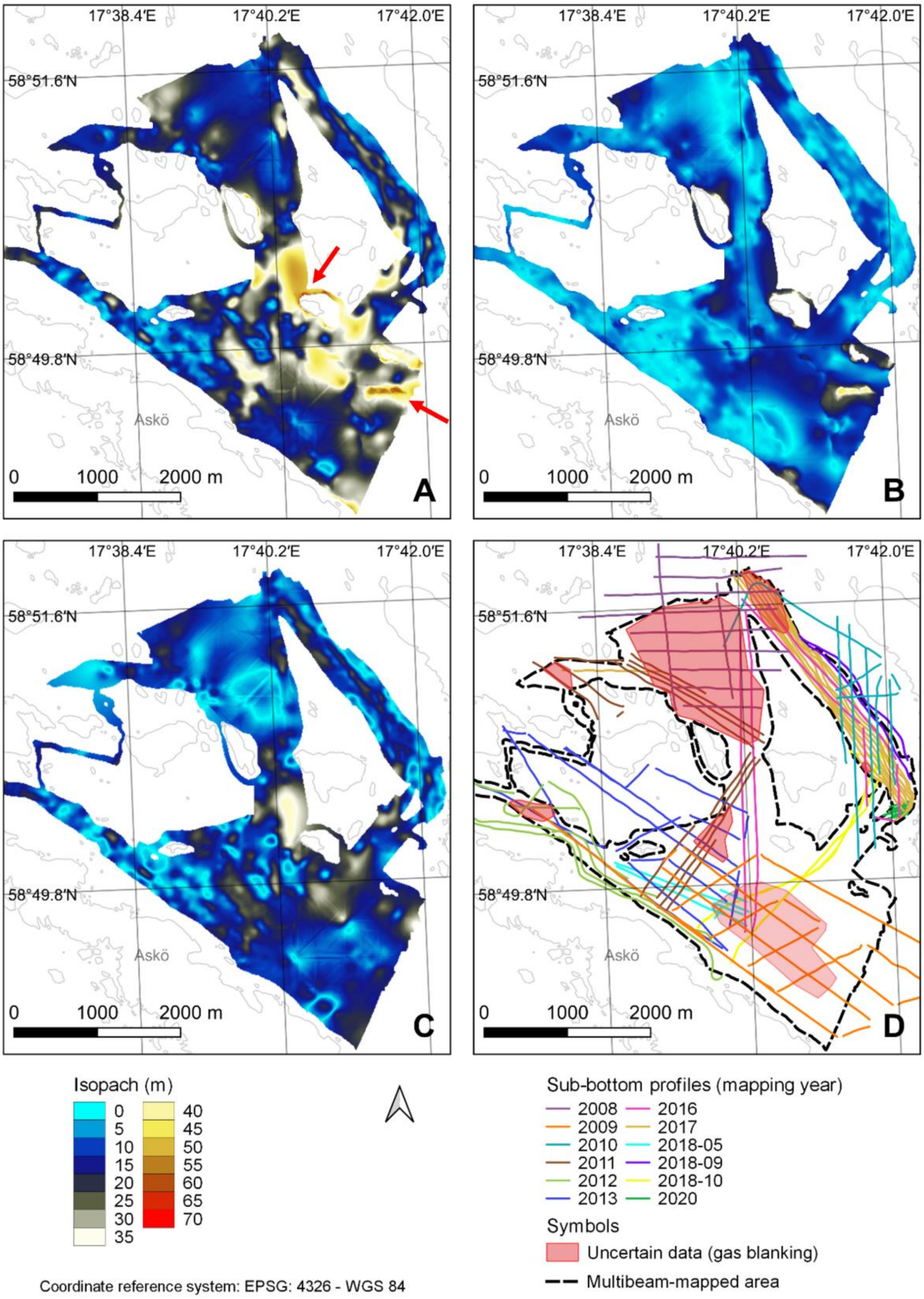

Figure 18. Isopach maps of the whole mapping area. A: Isopach between S-1 and multibeam bathymetry (the total sediment thickness). The red arrows indicate artifacts from gridding of unconstrained data (seen by the absence of sub-bottom profiles in these areas in figure D) yielding incorrect thickness values of around 55-70 m. B: Isopach between S-2 and the multibeam bathymetry (combined thickness of acoustic Unit 2, 3, 4 and 5). C: Isopach between S-1 and S-2 (acoustic Unit 1). D: Mapping area showing the locations of the mapped sub-bottom profiles and the areas of uncertain data due to the presence of blanks in the sub-bottom profiles.

Isopach map of the main research area/ core site south-west of Fifång

Below the terraces, at the location where the sediment cores were retrieved, acoustically stratified sediment appear to continue from the acoustic basement all the way up to the seafloor, with blanks extending from the acoustic basement to each terrace (Figure 19). By crossing another sub-bottom profile, whose stratifications of acoustic Unit 1 are more visible, the intersection between the two indicate that the sediment in the core site belongs to acoustic Unit 1 (Figure 20). However, reflector R-3 is not confidently distinguishable in any of the sub-bottom profiles that target the terrace area/core site (Figure 20), and consequently only the isopach map of the entire sediment column (S-1 to the multibeam bathymetry) was chosen to represent the sediment thickness at the core site (Figure 21). The total sediment thickness increases away from Fifång, from 5- 5.5 m at the location of core EL20-IGV07-1PC to a thickness of 6.5 m where both core EL20-IGV07-2PC and EL20-IGV07-3GC were retrieved (Figure 21).

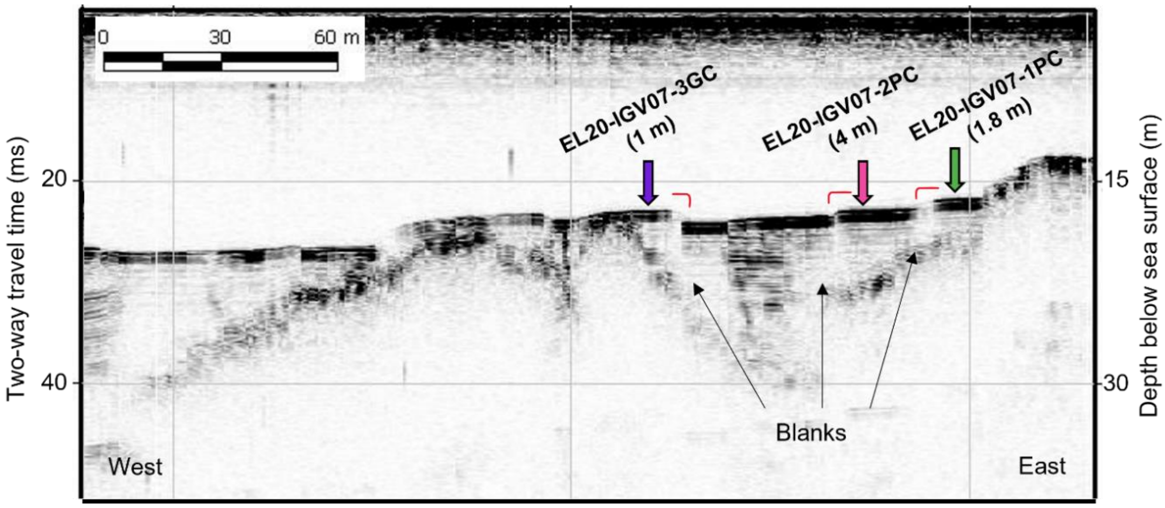

Figure 19. A cut-out from sub-bottom profile 20201201131013 showing a cross-section of the terraces and locations of the retrieved sediments cores (EL20-IGV07-1PC, 2PC, 3GC) in the main research area SW of Fifång, with Fifång being located to the east. The terrace steps are indicated with red markings above them.

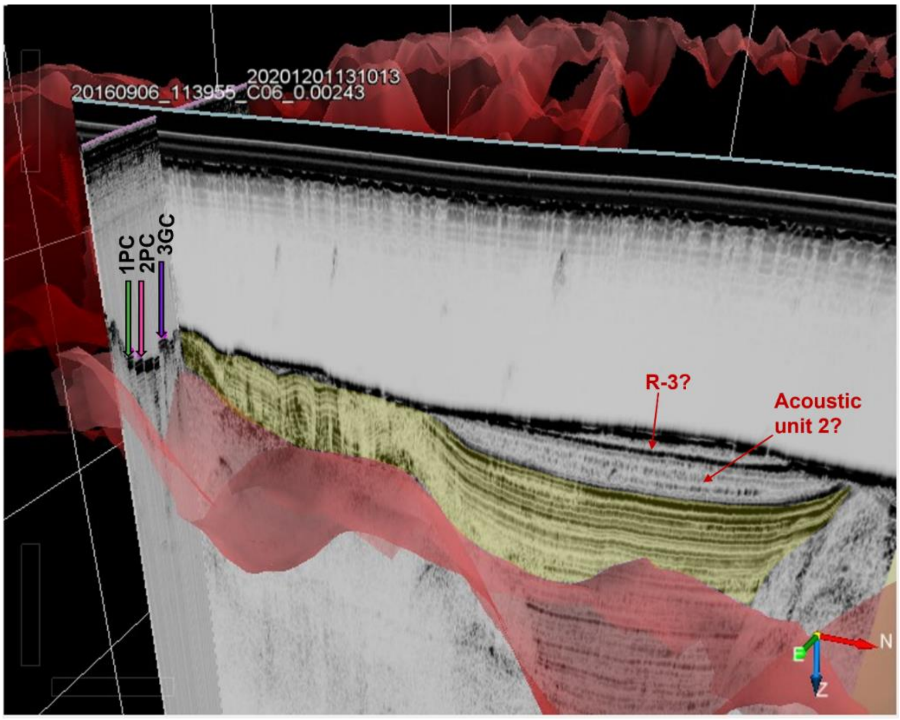

Figure 20. Sub-bottom profiles 20201201131013 and 20160906_113955) displayed in the 3D viewer in OpendTect. Also viewed is the gridded surface for the acoustic basement (S-1) in red. Sub-bottom profile 20201201131013 shows the locations of core EL20-IGV07-1PC, 2PC and 3GC. In the crossing sub-bottom profile 20160906_113955 the interpreted acoustic Unit 1 (yellow) is displayed. Where the two profiles cross there is a depression in the acoustic basement, which indicates that the sediments of the two sub-bottom profiles are connected. Therefore, the cores sample Acoustic Unit 1, which outcrop at the seafloor in this area. R-3 and acoustic Unit 2 are marked with question marks because the unit is acoustically stratified like Unit 2, but is thicker than Unit 2 usually is, resulting in an uncertainty to which acoustic unit it is.

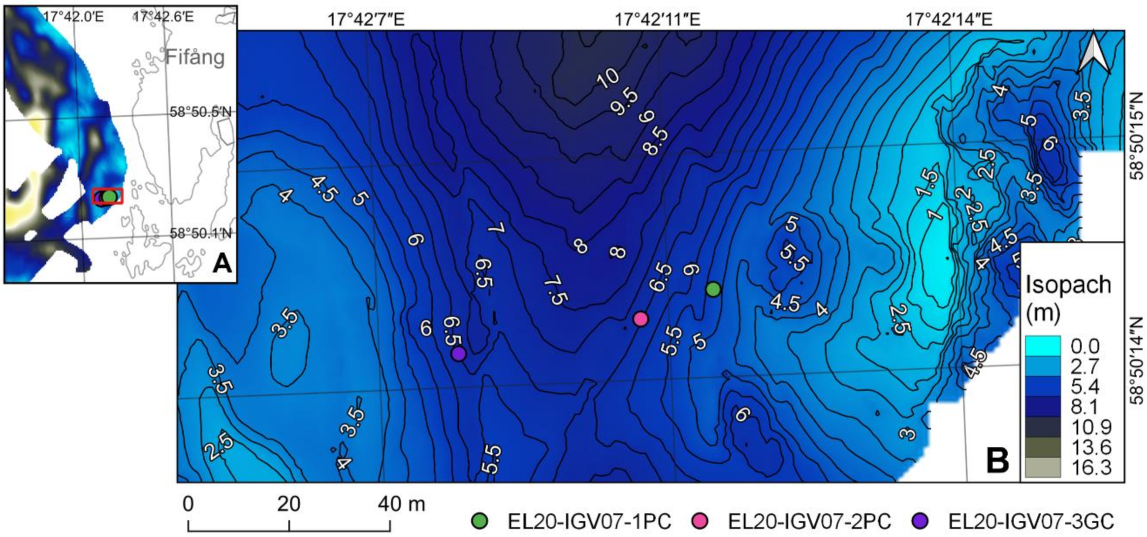

Figure 21. Isopach map of the total sediment thickness between the acoustic basement (S-1) to the seafloor (multibeam bathymetry) in the main research area/core site SW of Fifång. A: Overview of the main research area. B: Close-up of the total sediment thickness at the core site, with 5- 5.5 m thickness at the location of core EL20-IGV07-1PC and 6.5 m at EL20-IGV07-2PC as well as EL20-IGV07-3GC.

3.2. Geotechnical analyses

All 3 cores that were collected in 2020 were logged on the MSCL. Core EL20-IGV07-1PC was further opened for visual inspection and core EL20-IGV07-2PC was cut into samples which were used for geotechnical tests. The consolidation test for sample EL20-IGV07-2PC-130-136 had the wrong diameter value inserted to the control software, therefore the parameters obtained from the consolidation test for this sample were calculated manually based on a corrected sample diameter according to the calculations in Appendix B. This also resulted in the applied effective stress during consolidation of sample EL20-IGV07-2PC-130-136 exceeding the maximum limit of the 4500 N load cell, which caused the test to automatically end, and therefore the consolidation curve of the sample lacks an unloading (recompression) line. The complete consolidation test data is provided in Appendix D.

3.2.1. Physical properties and lithology

The general pattern of the measured physical properties of the three cores is that bulk density and magnetic susceptibility increase downcore while porosity decreases downcore, and at the bottom 0.5 m of each core there is a distinct change in all the measured properties (Figure 22). Visual inspection of core EL20-IGV07-1PC show that other than a thin surface layer of sandy, shell bearing silt, the entire core is composed of varved glacial clays (Figure 23). This was also noted for core EL20-IGV07-2PC during sample preparations. The varves compose of dark and light-colored layers that thicken up-core, with section 2 (1.51-0.31 mbsf) comprising of ca 0.5 cm thick light layers and 0.1-0.3 cm dark layers, while section 1 (0-0.31 mbsf) contain approx. 1 cm light layers and 0.3 cm dark ones. In the upper and lower ca 20 cm of the core the varves are inclined (Figure 23) which also is seen in samples from both core EL20-IGV07-1PC and EL20-IGV07-2PC (Figure 24A-C). In the bottom 0.5 m of each core the physical property changes follow the same pattern, with the magnetic susceptibility increasing from ~ 40-60 to ~80-90, the bulk density increasing from ~1.7-1.8 to 2-2.2 g/cm^3 and porosity decreasing from ~0.6 to 0.4 (Figure 25).

The cores consist entirely of glacial clay belonging to the same lithologic unit, which is subdivided into two sections: lithologic Unit 1A and 1B (Figure 25). These subdivisions are, however, not reflected in the sediment of core EL20-IGV07-1PC, other than that the varves are tilted at a depth corresponding to the top of 1B (Figure 25), while the rest of 1B (1.51 m to 1.79 m, Table 1) was cut at 1.51 m prior to being split open (Figure 23). The general downcore changes in the physical properties are however correlated to the downcore increase of silt in core EL20-IGV07-2PC (Table 3).

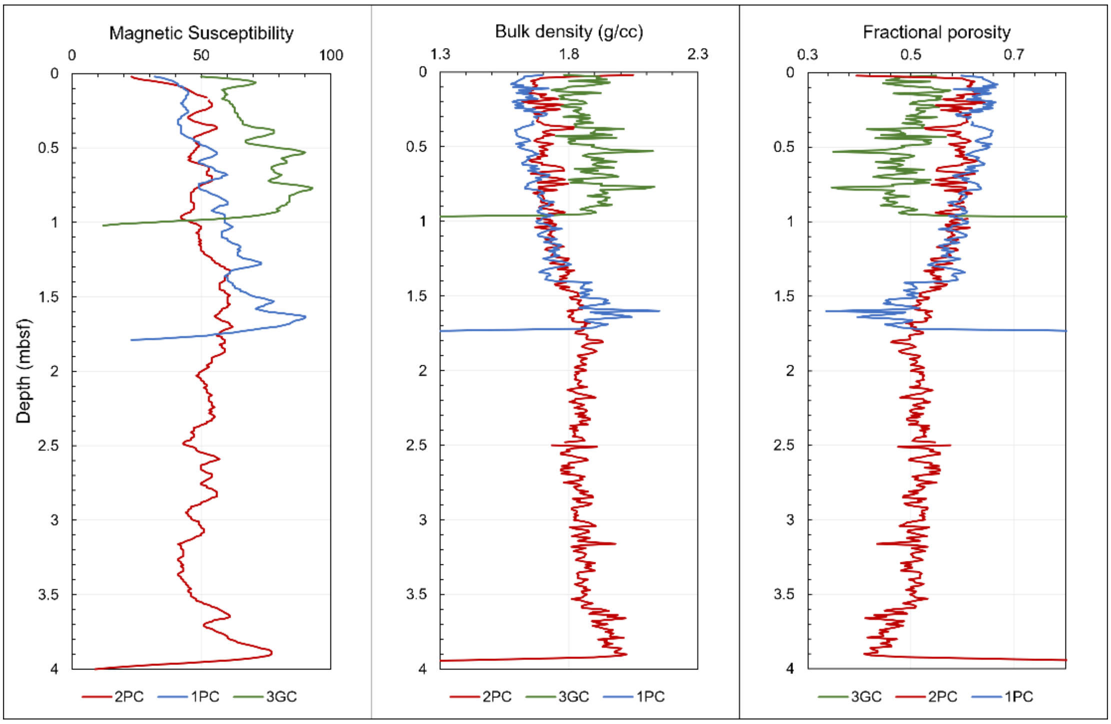

Figure 22. MSCL measured magnetic susceptibility, bulk density (g/cm3) and fractional porosity for the three cores retrieved outside of Fifång (EL20-IV07-1PC, 2PC and 3GC). The physical properties of the cores have a similar pattern with the magnetic susceptibility and bulk density increasing downcore and porosity decreasing simulateously. The lower 0.5 m of the cores show a distinct change in all the measurements.

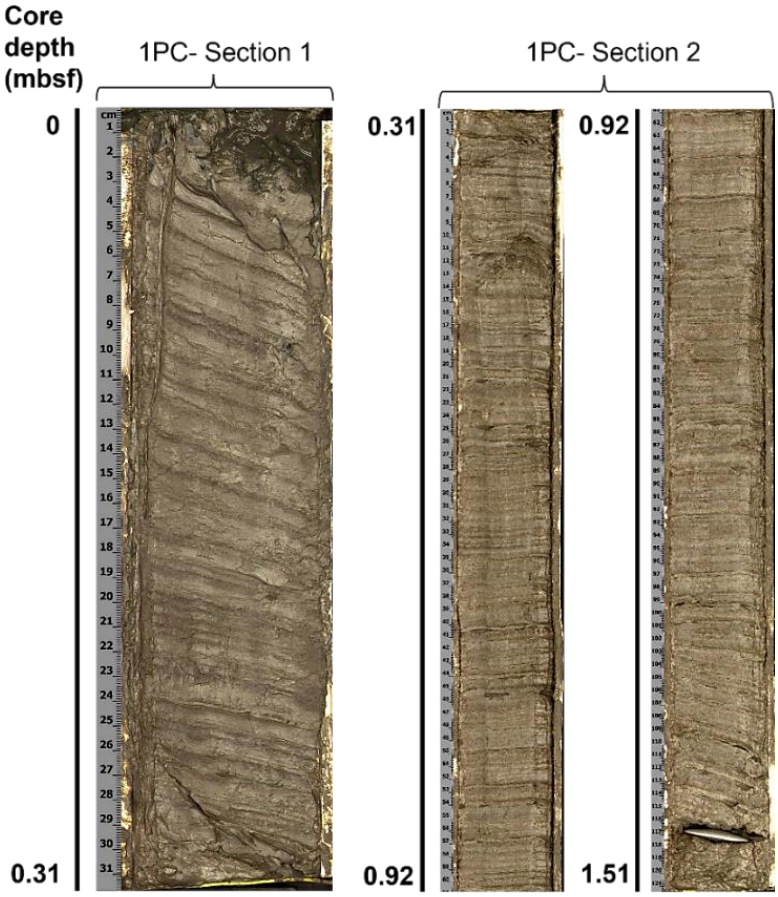

Figure 23. Core EL20-IGV07-1PC (0-1.51 mbsf). The bottom section of the original core (being 1.79 m, table 1) is not included as this was cut off for geotechnical tests for a university course outside of this project. The thickness of the varves increase upwards and this is most notable in section 1. A Marleka is buried in the bottom of section 2.

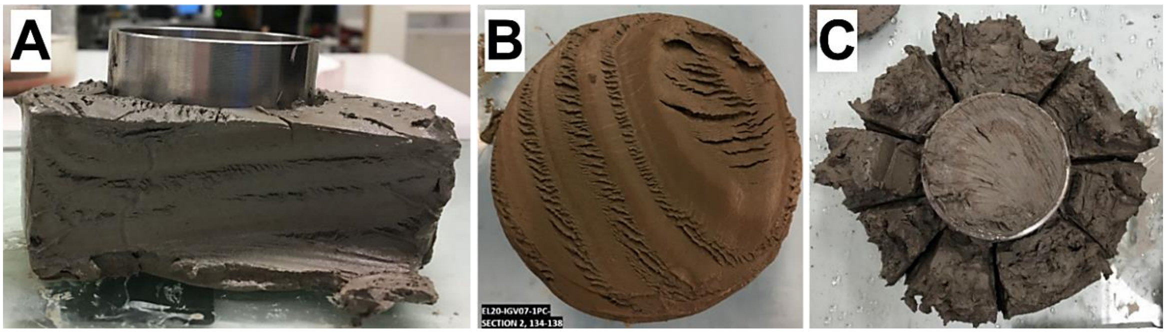

Figure 24. Samples displaying the tilted varves of glacial clay. A and B belong to core EL20-IGV07-1PC and C is from section 3 of core EL20-IGV07-2PC (Table 1).

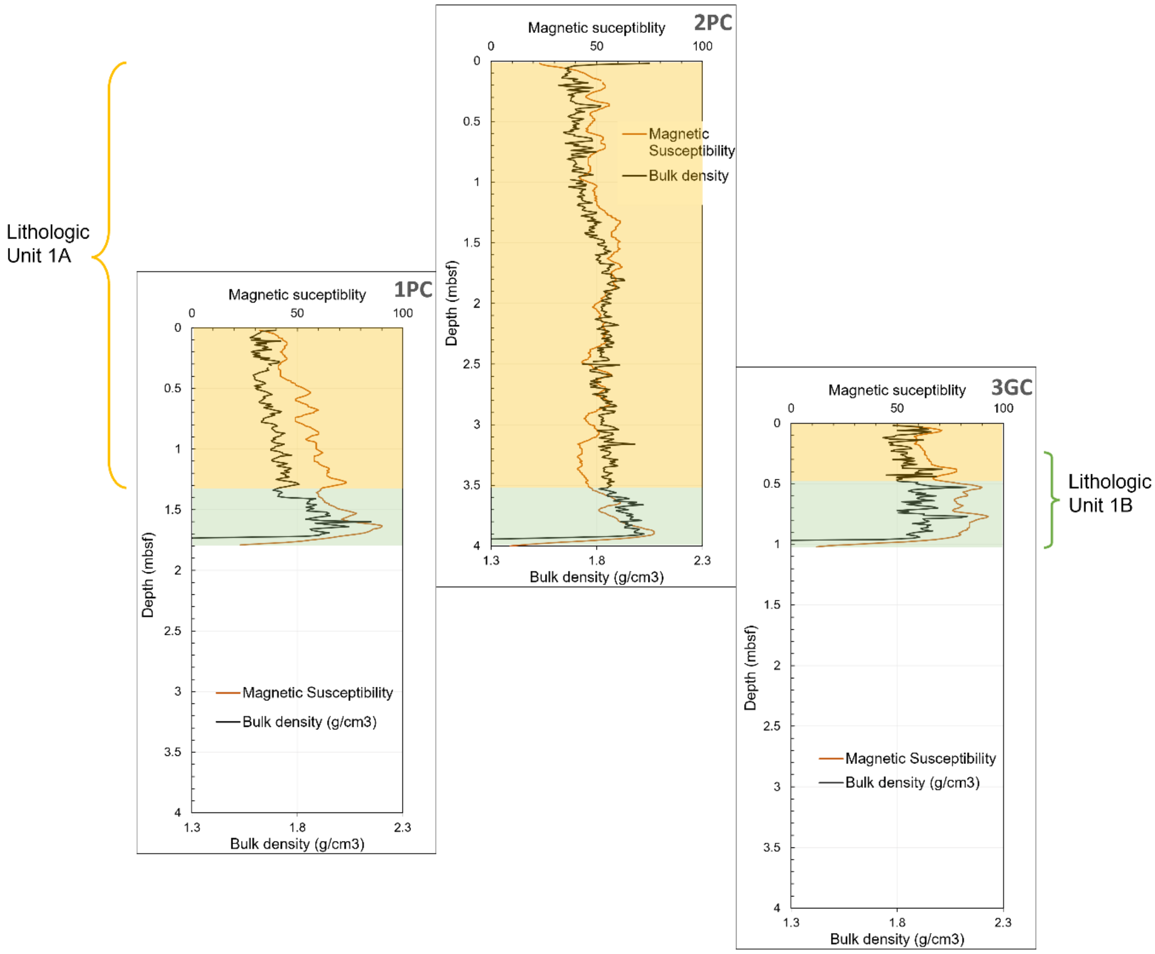

Figure 25. Correlating the MSCL measured magnetic susceptibility and bulk density of the three cores with regards to the inferred lithologic sub-units 1A and 1B. In sub-unit 1A the values increase slighly downcore and in 1B a sharp increase occurs in all cores ca 0.5 m from the bottom of the cores.

Sample	**EL20-IGV07-2PC-SEC 2-0-3**	**EL20-IGV07-2PC-SEC 2-4-7**	**EL20-IGV07-SEC 2-147-152-A**	**EL20-IGV07-SEC 2-147-152-B**	**EL20-IGV07-2PC-SEC 3-120-125**	**EL20-IGV07-2PC-SEC 3-130-136**	**EL20-IGV07-2PC-SEC 3-136-142**
Average percentage clay (0-4µm)	75	95	73	54	51	47	-
Average percentage silt (4-63µm)	25	5	27	46	49	53	-
Standard deviation (%)	0.037	0.021	0.146	0.239	0.108	0.020	-
Average grain density (g/cm³)	2.728	2.724	2.748	2.743	2.730	2.734	2.722
Standard deviation (g/cm³)	0.0052	0.0025	0.0015	0.0015	0.0016	0.0012	0.0012

Table 3. Grain size and grain density of core EL20-IGV07-2PC. The grain sizes found in core EL20-IGV07-2PC are within the size range of clay and silt (<4 - 63µm), with no detected sand or larger sized material (> 63 µm). The grain sizes generally increase downcore, with clay being highly dominant in the upper part of the core (75-95 % clay), and silt slightly dominating in the bottom (49-53 % silt). The grain density is around 2.72-2.73 g/cm^3 at the upper and lower part of the core, while the middle section of the core contains grain densities up to ~ 2.75 g/cm^3.

3.2.2. Consolidation test results

Virgin Compression Line (VCL) extraction

The consolidation plots show how the samples experience a rapid decrease, or collapse, in void ratio at the curve break between the recompression line and virgin compression line (VCL), which mainly affects the shallow samples (Figure 26A-D) and become less prominent in samples from deeper within the core (Figure 26E-F). This resulted in non-linear VCLs of the consolidation curves, as opposed to the linear VCL of a textbook example sample (Figure 8). Despite using the log-log method to produce a more linear VCL , a straight line could not be drawn between the load steps along the VCL for the shallow samples, due to their non-linear collapse in void ratio. Instead, a best fitting line for the VCL was drawn from where the break in the consolidation curve was initiated to the maximum load step (Figure 26A-D). The slope of this line represents the compression index (C_c) if the samples had consolidated linearly along the VCL (Figure 26).

Pre-consolidation pressures and overconsolidation ratio (OCR)

The pre-consolidation pressures increase slightly downcore with values ranging from 45 to 100 kPa (Figure 26, Figure 27). All pre-consolidation pressures exceed the estimated in situ downcore effective stress (which was derived from the MSCL bulk density (Equation 7)). This implies that all the sediment in the core is overconsolidated (Equation 9, Figure 27). Since the pre-consolidation pressures are derived graphically there is a considerable degree of uncertainty regarding the accuracy of the individual values of each sample. The average pre-consolidation pressure is 61 kPa and provides the best estimate for the study area. This means that the maximum effective stress that the sediment has experienced in the past is 61 kPa, which, by using the sample bulk densities of 1.79-1.44 g/cm^3 (Table 3), corresponds to a past burial depth of 8-14 m (Equation 6). Consequently, 8-14 m of sediment have been removed from the location of core EL20-IGV07-2PC.

Void ratio, compression index and grain size

When comparing the consolidation test results, a striking observation is that differences in the compression index (C_c) and inferred void ratio upon deposition (e_0) (Figure 26) appear to be strongly controlled by changes in the clay and silt content of the samples. Higher silt content reduces e_0 and lowers C_c (Table 3). Samples that contain the highest clay fraction have experienced the highest void ratio depletion since deposition (e_0) and experience the most void ratio (e) loss, during the consolidation test (Figure 26). It is evident that at any given effective stress (i.e. burial depth), the samples with high clay content (75-95 % clay) have a higher void ratio (thus, higher porosity (Equation 5)) than the silt-enriched ones (~ 49-53 % silt) (Figure 28A).

Void ratio, hydraulic conductivity, and grain size

By plotting the hydraulic conductivity (k) and void ratio (e) at the load steps along the VCL, the k- e relationship during sediment compression is derived (Figure 28B). It shows that, generally, for any given void ratio (e) the hydraulic conductivity is higher for the samples with a higher fraction of silt (Figure 28B).

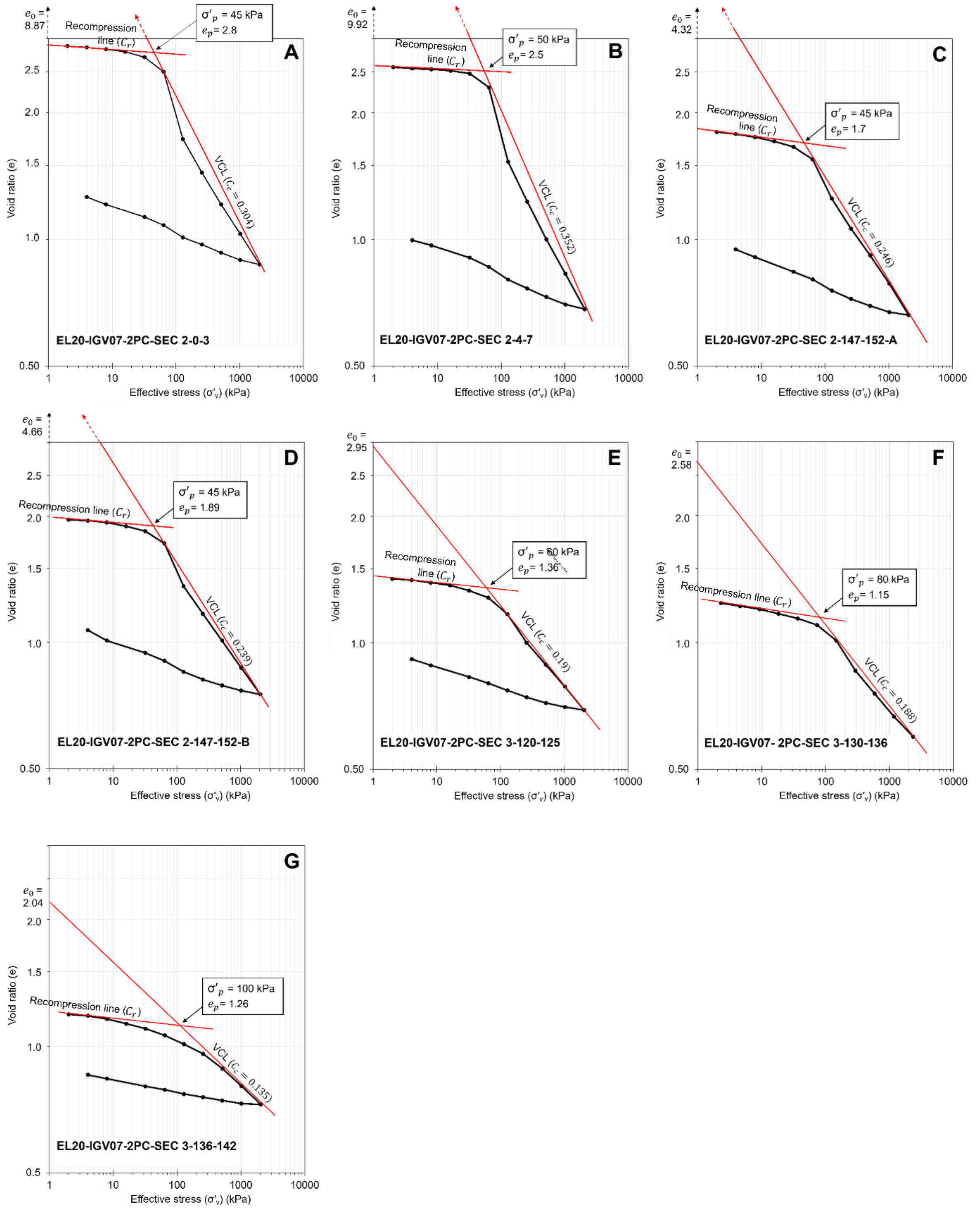

Figure 26. Consolidation curves of the samples from core EL20-IGV07-2PC, plotted on logarithmic axes. They are plotted with the fitted recompression line and virgin compression line (VCL) annotated with their corresponding slopes (recompression index (C_r) and compression index (C_c) respectively), and the deduced pre-consolidation pressure (σ'_v), void ratio at the pre-consolidation pressure (e_p) and initial void ratio upon deposition (e_0) (Table 4), according to the graphical log-log method . The shallower samples from section 2 (A-D) experience a larger void ratio loss (including a rapid collapse in void ratio at the curve break after the pre-consolidation pressure is met) during the consolidation test than the deeper samples in section 3 (E-F). This results in the shallower samples having a steeper VCL and higher compression index than the deeper samples. The void ratio upon deposition (e_0) is much higher for the shallow samples and decreases notably downcore.

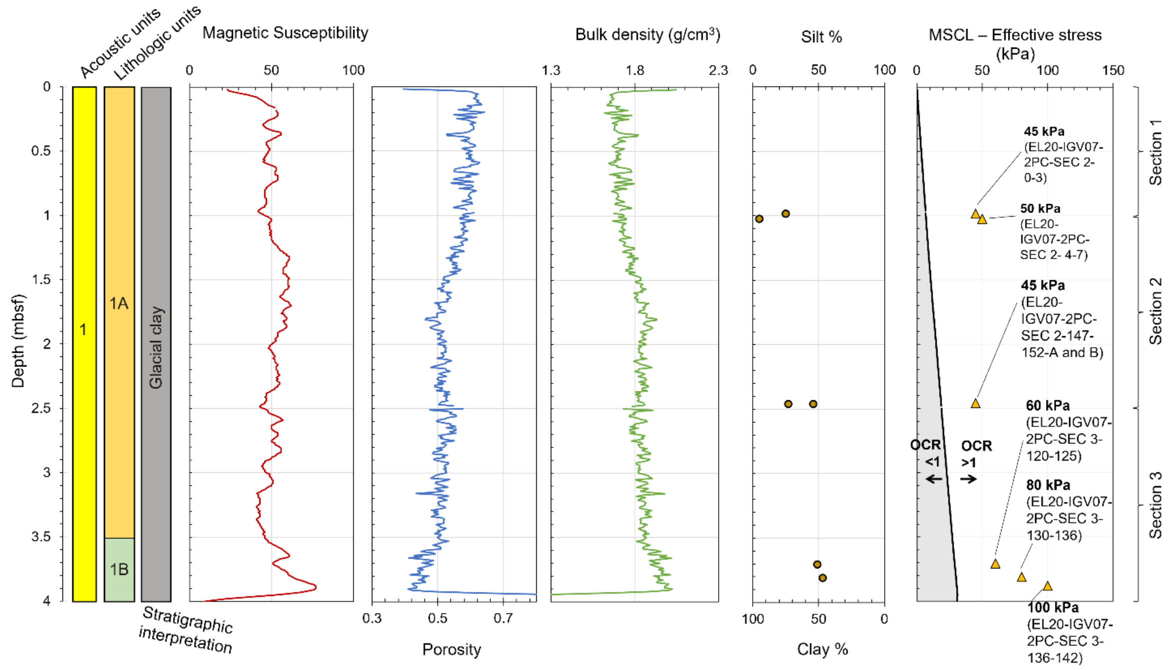

Figure 27. Interpreted acoustic unit, lithologic unit, stratigraphic interpretation and sediment physical properties of core El20-IGV07-2PC, retrieved outside of Fifång (Figure 12B). The MSCL derived magnetic susceptibility and bulk density increase gradually downcore while porosity decrease downcore. The grain size measurements are summarized in Table 3, and indicate a gradual downcore increase in amount of silt. The yellow triangles show the depths of the consolidation samples with their determined pre-consolidation pressures and sample names annotated, and the MSCL derived in-situ effective stress at various core depths is shown in the same plot (black descending line). All pre-consolidation pressures plot at higher stress values than the in-situ effective stress, indicating that they are overconsolidated (OCR>1) (Table 4).

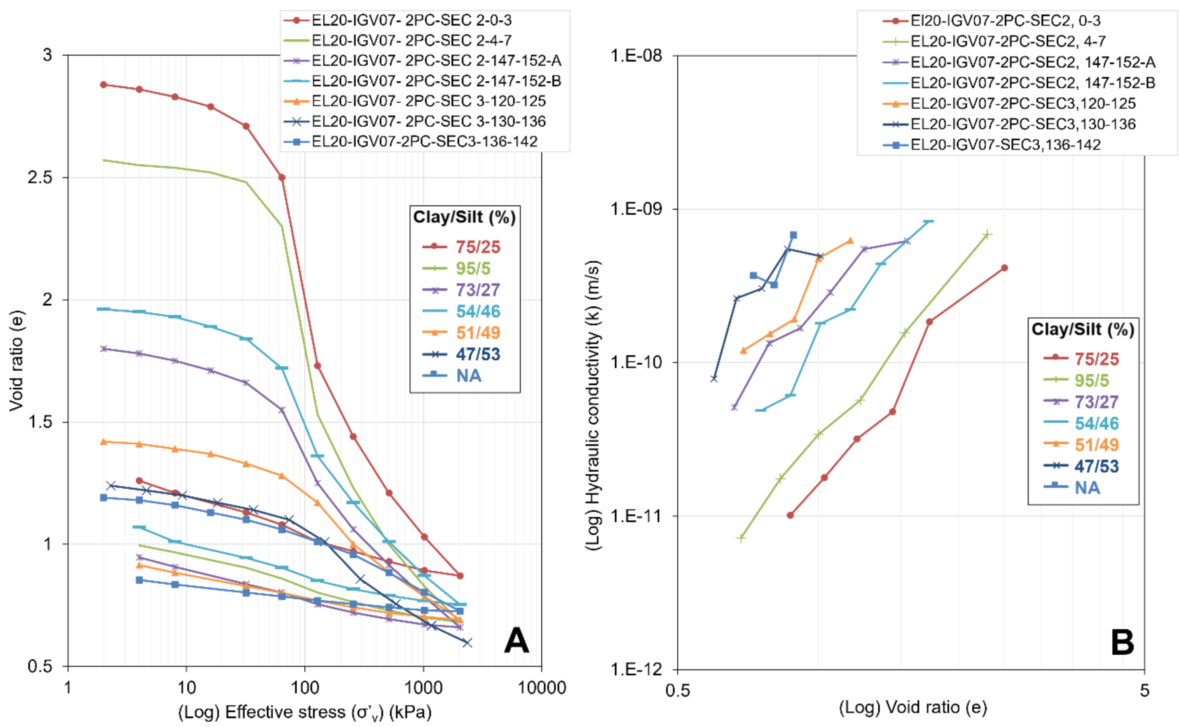

Figure 28. Consolidation plots of all samples with their measured clay/silt ratios (Table 3) showing the relationship between void ratio and hydraulic conductivity with grain size variations and depth (effective stress). A: Complete consolidation curves of the samples showing that the clay rich samples have higher initial void

ratios and the highest amount of void ratio loss as the effective stress (burial depth) increases, compared to the silt-enriched samples which contain a lower void ratio as well void ratio loss throughout the test. At a specific effective stress, the void ratio is higher for the clay-rich samples than for the silt-enriched samples. B: A *log k-log e* plot showing the load steps along the virgin compression line (VCL) of all samples. At any void ratio the clay-rich samples have a lower hydraulic conductivity than the silt-enriched samples. The combination of A and B shows that at any effective stress (burial depth) the silt-enriched samples have a lower void ratio, but at any void ratio they have a higher hydraulic conductivity than the clay-rich sediment.

3.2.3. Modelling in-situ porosity and hydraulic conductivity

To explore the groundwater flow velocities that can be generated through the outcropping glacial clays and assess if internal erosion can occur at the terrace site, the hydraulic conductivity and porosity of the sedimentary column are required (section 1.2.2).

Since at a given burial depth the clay-enriched samples will have a higher void ratio than silt-enriched samples (Figure 28A) but at any given void ratio the clay-enriched samples have a lower hydraulic conductivity (Figure 28B), these two properties may counteract, and in the end, the in-situ permeabilities of the two grain sizes may be quite similar despite their different properties. Nevertheless, due to the grain size variability seen in the varved glacial clay sequence, and their influence on compression and permeability, no single function can be used to predict the porosity and hydraulic conductivity at depths that extend below the lowermost recovered sediments. To overcome this, two end-member models are developed from a clay rich sample (EL20-IGV07-2PC-SEC 2-0-3) and a silt rich sample (EL20-IGV07-2PC-SEC 3-130-136) (Table 3).

The effective stress at the sea floor was set to the average pre-consolidation pressure of the core (61 kPa). The log void ratio (e) - log effective stress (σ'_v) relationship was defined along the VCL of each end-member sample (Figure 26A and F) and the void ratio corresponding to the initial effective stress (61 kPa) at the seafloor was obtained by:

$$e = 10^{(C_c \log(\sigma'_v) + \log(e_0))} \tag{10}$$

from which the corresponding porosity (ϕ) was derived (Equation 5).

Using the porosity (ϕ), sample grain density (ρ_G) (Table 3) and fluid density (ρ_f) of 1 g/cm^3, the bulk density (ρ_B) at the seafloor was calculated using:

$$\rho_B = \rho_G(1 - \phi) + \rho_f \phi \tag{11}$$

The corresponding hydraulic conductivity was calculated from the exponential equations defining the log hydraulic conductivity-porosity relationships for each endmember along the VCL (Figure 29). The final porosity-depth and hydraulic conductivity-depth models were extended in 1 m increments to a depth of 30 m, providing estimates of the in-situ porosity and hydraulic conductivity for clay-rich and silt-rich samples (Figure 30). A depth of 30 m is arbitrarily selected for illustrative purposes and shows how at any given depth the porosity of the silt enriched samples is lower, but that the hydraulic conductivity indeed remains higher than the clay-rich samples (Figure 30).

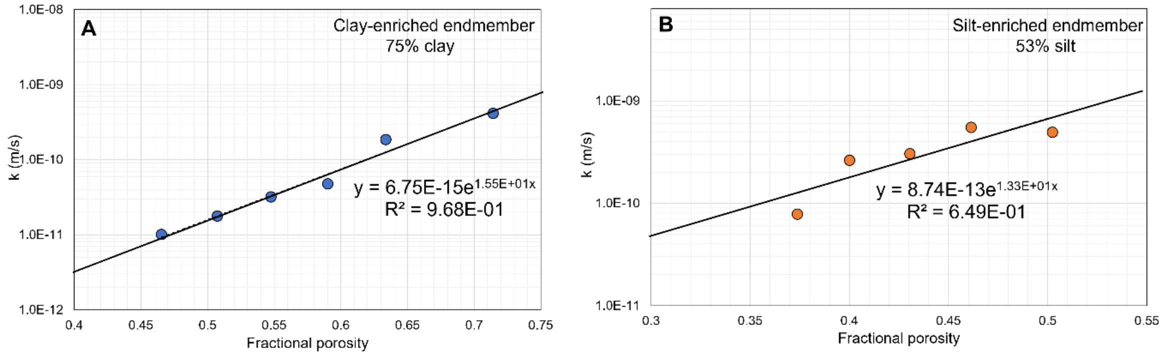

Figure 29. The clay-endmember samples plotted on log hydraulic conductivity (***k***, m/s) - porosity graphs, showing the best fit equations for the relationship between hydraulic conductivity and porosity for each sample. A: The clay-enriched endmember (EL20-IGV07-2PC- SEC 2-0-3), the best fit equation has an R-value of ~ 0.97 yielding a good fit between the samples. B: The silt-enriched endmember (EL20-IGV07-2PC-SEC 3-130-136) having a best fit with a lower R-value of ~ 0.65.

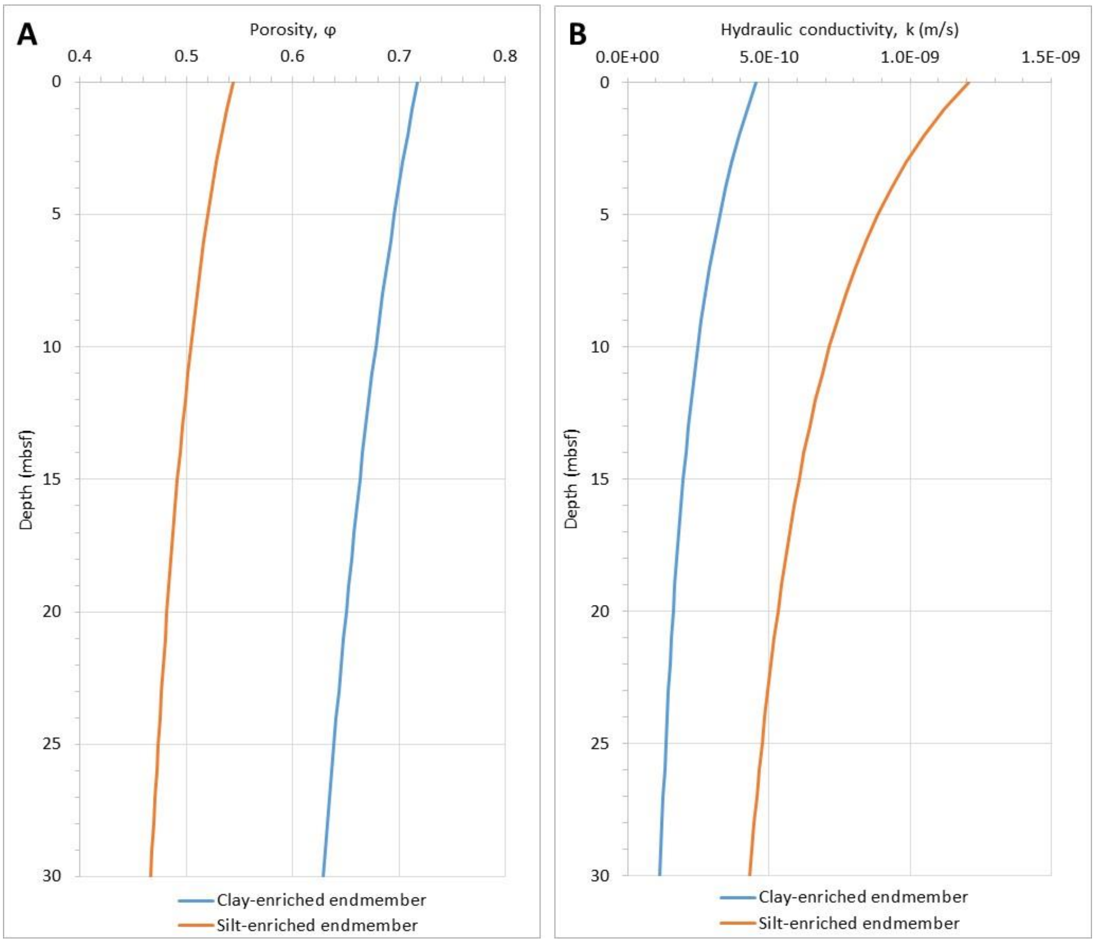

Figure 30. Graphs showing the extended porosity-depth and hydraulic conductivity-depth models for the two clay-endmember samples, where sample EL20-IGV07-2PC- SEC 2-0-3 represent a clay-enriched endmember and sample EL20-IGV07-2PC-SEC 3-130-136 represent a silt-enriched endmember. The depth scale represents meters below the seafloor. A: The difference in porosity with depth between the endmembers is consistent, with the clay-enriched endmember having ca 20 % higher porosity than the silt endmember throughout the profile. B: The hydraulic conductivity is higher for the silt-enriched sample throughout the depth profile, with almost an order of magnitude higher k at the seafloor, while the difference between the endmembers decrease downcore.

Sample ID	Interval (cm)	Depth (mbsf)	ρ_B (g/cm³)	ρ_G (g/cm³)	σ'_v (kPa)	σ'_P (kPa)	e_P	OCR	C_C	C_r	e_0	Clay (%)	Silt (%)
EL20-IGV07-2PC-SEC2-0-3	0-3	0.99	1.44	2.73	6.85	45	2.8	6.57	-0.304	-0.013	8.87	75	25
EL20-IGV07-2PC-SEC2-4-7	4-7	1.03	1.51	2.72	7.10	50	2.5	7.04	-0.352	-0.008	9.92	95	5
EL20-IGV07-SEC2- 147-152-A	147-152	2.46	1.65	2.75	18.61	45	1.7	2.42	-0.246	-0.020	4.32	73	27
EL20-IGV07-SEC2- 147-152-B	147-152	2.46	1.59	2.74	18.61	45	1.89	2.42	-0.239	-0.011	4.66	54	46
EL20-IGV07-2PC-SEC3-120-125	120-125	3.71	1.74	2.73	28.93	60	1.36	2.07	-0.190	-0.015	2.95	51	49
EL20-IGV07-2PC-SEC3-130-136	130-136	3.81	1.85	2.73	29.91	80	1.15	2.67	-0.188	-0.024	2.58	47	53
EL20-IGV07-2PC-SEC3-136-142	136-142	3.88	1.79	2.72	30.57	100	1.26	3.27	-0.135	-0.018	2.04	-	-

Table 4. Consolidation samples and summary test results. ρ_B is the bulk density of the saturated sample prior to consolidation testing, calculated from the volume and mass of the sample. ρ_B is the measured grain density of the dried trimming of the sample. σ'_v is the estimated in-situ effective vertical stress at the location of the sample, which was calculated from the MSCL measured bulk density. σ'_P is the graphically derived pre-consolidation pressure according to the log-log method . e_P is the corresponding void ratio at the pre-consolidation pressure. OCR is the overconsolidation ratio. C_c is the compression index, which is the slope of the VCL. C_r is the recompression index, which is the slope of the recompression line. e_0 is the void ratio upon deposition, corresponding to an effective vertical stress of 1 kPa. The percentages of silt and clay are summarized from Table 3.

4. Discussion

4.1. Correlating the acoustic units, the lithologic unit, and the Baltic Sea sedimentation history.

The digitized reflector 1 (R-1) marks the acoustic basement, which is interpreted as the bedrock or till overlying the bedrock. The presence of sandy till on the islands indicate that till could be present at the bottom of the seafloor since the islands were below sea level when the till was deposited (Figure 6B). The layer of till probably originates from when the Fennoscandian Ice Sheet (FIS) retreated in oscillations during the deposition of the Middle Swedish End Moraine Zone (12.9-11.7 cal. ka BP) (Figure 4A). However, the presence of older till from previous glaciations cannot be excluded. Acoustic Unit 1, with its continuous and pronounced acoustical stratification, is interpreted to be varved glacial clay. This interpretation is supported by the observations of the sediment cores, which were retrieved from acoustic Unit 1 (Figure 20), as they all have similar physical properties, are generally correlatable, and are composed of varved glacial clays (Figure 23 and Figure 25). Lithologic Unit 1B, which marks a distinct increase in bulk density and magnetic susceptibility in the bottom 0.5 m of the cores, correlate to a general downcore coarsening of the grain sizes with the highest silt fraction in lithologic Unit 1B (Figure 27). This is interpreted as the oldest, most coarse-grained glacial clay, which was deposited closest to the retreating ice margin, while the up-core finer grained sediments reflect an increased distance to the ice margin as the ice retreated northwards (Andrén, et al., 2011 and Swärd, et al., 2018). This grain size distribution is further seen in acoustic Unit 2, where the acoustic stratifications are like that of acoustic Unit 1, but often with weaker amplitudes, which may reflect a finer grained glacial clay, indicative of a distal ice margin. Acoustic Unit 3 is acoustically stratified in the lower section with generally no internal parallel reflections upwards. This unit may have been deposited during the Yoldia Sea (YS) stage when sedimentation rates increased rapidly and the ice margin retreated fast , resulting in a thicker varved clay at the bottom of the unit and a more homogeneous, fine grain size deposition further up, likely also containing postglacial clay as it started to deposit toward the end of the YS stage . Acoustic Unit 4, being the thinnest unit, is interpreted to compose entirely of postglacial sediments such as gyttja clay, which continues to build up today.

The presence of glacial clay and postglacial sediments on the islands, particularly on Askö, indicate that the islands were submerged for a long time before emerging due to isostatic uplift, and the exposed bedrock on the islands indicate that extensive erosion has taken place since (Figure 6B). This is also evident from the samples from core EL20-IGV07-2PC which all show a state of overconsolidation (Figure 27), indicating that these glacial clays were more deeply buried in the past and have been subject to somewhere between 8 and 14 meters of erosion/overburden removal (section 3.2.2). The thickness of this eroded sediment correlates with the isopach of the combined acoustic Units 2, 3 and 4 in the deep waters of the survey area (10-20 m) (Figure 18B), which further suggests that erosion due to uplift have allowed the glacial clay to be exposed at the seafloor in near-shore areas, and a hydraulic head between the land- and sea-based glacial clays may have formed, allowing the clay to serve as a groundwater conduit (Virtasalo, et al., 2019 and Jakobsson, et al., 2020). This is indicated by the presence of terraces in the near-shore areas, as well as terraces only occurring in glacial clay (Figure 5 and Figure 15). However, the exposed bedrock on the shores of Fifång or Askö (Figure 6B) speaks against a connection between the terrestrial and marine glacial clays through which the groundwater can flow. The tilted glacial clay varves, which are found in the sediment cores of this project (Figure 23 and Figure 24) as well as in other cores that have been retrieved in the area , could be the result of isostatic uplift causing the sediments to tilt as the bedrock and overlying sediments were rearranged by fracturing and folds from the movement.

4.2. Indications for groundwater flow through silty layers in varved glacial clay.

The hypothesis of this project was that groundwater travels from land through more permeable zones in the glacial clay and discharges at the seafloor to form terraces by erosion. Geotechnical tests have established that silt-enriched samples have higher permeability than the clay-enriched ones for a given porosity and that the compression behaviour and permeability/conductivity appear to be heavily dependent on grain size. The same conclusions were made by Schneider et al. (2011) in a study of laboratory mixed sediments composing of glaciomarine Boston Blue Clay and various amounts of silt-sized silica, who explained this phenomenon using a dual porosity system of clay and silt. They argue that the contact between silt grains creates silt bridges, which prevent the clay particles within the silt arrangement from being consolidated, consequently creating larger pore spaces within the matrix of silt grains that allow for enhanced fluid to flow through the sediment. This results in a higher hydraulic conductivity for silt-enriched compared to clay-enriched sediment at a specific porosity. The geophysical mapping has shown that the terraces exclusively form in glacial clay where it outcrops at the seafloor. Theoretically, this supports the hypothesis that fluid flow is more likely to be constrained within the silty layers in the varved glacial clay and that where the overlying sediment (glacial and postglacial) has been eroded fluids can discharge at the seafloor to form terraces.

However, direct lateral groundwater flow through the glacial clay from onshore Fifång to the core site-terraces is unlikely because the glacial clay sediments are discontinuous from land to sea (apart from a few locations away from the coring site), and instead bedrock outcrops all the way to the sea closest to the core site (Figure 6B). This is also evident from the glacial clay in the core site being constrained within a depression in the bedrock from which the clay is cut off from Fifång (to the east) by the acoustic basement (Figure 19). Another potential contradiction to the proposed lateral flow path is that the terraces are often accompanied by blanked areas in the sub-bottom profiles that emerge upwards from the acoustic basement (Figure 15). These blanks are here suggested to indicate upward migration of groundwater, as they resemble the suggested groundwater conduits found in sub-bottom profiles in south Finland , which were interpreted to indicate an upward flow path. The fluids appear to be consistently found within the glacial clay and cease in the overlying units, which could imply that the fluids mainly penetrate the coarser, deeper situated varved clay, but not the overlaying finer glacial and postglacial clay.

Therefore, apart from lateral groundwater flow, vertical, or near-vertical groundwater flow through the glacial clay must be considered when modelling the groundwater flow path through the sediment. In both scenarios the groundwater could initially be transported through fractures in the bedrock or through a potential till-layer draping the bedrock (in either case we assume that this media is perfectly transmissible) before entering the glacial clay.

4.3. Groundwater flow calculations

With Darcy's law of laminar flow in porous media we can evaluate if the hydraulic conductivity of the sediment is high enough for groundwater to erode them and initiate formation of the terraces. As described in section 1.2.2, erosion occurs when a sediment is exposed to a critical fluid velocity (v_c) which causes a shear stress that exceeds the shear strength of the sediment. According to Darcy's law, the velocity of fluids travelling through the pores in the sediment, the seepage velocity **(v_s, m/s)**, depends on the change in hydraulic head **(dH, m)** per unit length **(dL, m)** in the direction of the flow in an isotropic aquifer **(dH/dL)** and the hydraulic conductivity **(k, m/s)** and porosity **(ϕ)** of the sediment (Holtz, et al., 2011):

$$v_s = \frac{k\frac{dH}{dL}}{\phi} \tag{12}$$

To apply this equation, an average value of the hydraulic conductivity and porosity of the sediment are derived from the silt- and clay-rich end member models, while estimates of dH and dL are obtained from the mapped locations of the terraces, and thickness of the underlying the sediments.

4.3.1. Variables for Darcy's Law

dH

Assuming groundwater can flow through the varves anywhere within the glacial clay column, the change in hydraulic head (dH) is the difference between the elevation of the sea surface (H_1) and the elevation of the groundwater table (H_2) (Figure 31). According to the initial reported values of the groundwater table on Fifång based on SGU (2021), the groundwater table is exceptionally low (26 mbsl) compared to the nearby islands (Figure 5). The low reported values from SGU could have been a temporary anomaly as the groundwater level could have been downdrawn from pumping or from being measured directly after drilling of the well before being filled, for example. Instead, assuming that the groundwater table is like that of the other islands, the groundwater table is around the same level as the sea surface (Figure 5), which results in a dH of 0 m and no possible fluid flow. However, the personnel of the Baltic

Sea Centre at Askö recently went to the well on Fifång to observe the water level in the well (in Feb, 2022). They observed a water level some 0.5-1 m below ground (Eva Lindell personal communication), which is significantly different from SGU's reported levels. This would correspond to a groundwater table of 5-5.5 masl as the elevation of the ground at the well is 6 masl (Figure 5). Furthermore, as groundwater levels fluctuate by at least 2 m throughout the year (according to the closest located measuring station in Sandvik, ca 8 km north of the study area (Appendix E) (SGU, 2021), and since the reported groundwater tables differ, an arbitrary groundwater table range between 1-25 masl is chosen to represent the change in hydraulic head (dH) for the groundwater flow calculations (Figure 31).

dL

The distance over which the groundwater travels is different for the two flow scenarios (Figure 31). The lateral flow model will have a dL of 325 m, which equals to the distance between core 2PC and the shore of Fifång (Figure 9). This is calculated from the shore as the glacial clay does not extend onto Fifång. The vertical flow model will have a dL of 6 m, corresponding to the average thickness of the sediment at the core site (Figure 21), but assumes there is no hydraulic head lost as the groundwater travels through the highly permeable bedrock and/or till.

Hydraulic conductivity ($\boldsymbol{k}$) and porosity ($\boldsymbol{\phi}$)

From the geotechnical tests and the modelled hydraulic conductivity and porosity with depth for the two clay endmembers (Figure 30) it is evident that the small grain size changes need to be considered when modelling the potential groundwater flow through the sediments in the area. Therefore, the silt and clay endmembers are used to define the permeability and porosity of the sediment, based on their average values over the depth of the sediment thickness of 6 m. The resulting average numbers are: $k_{clay} = 3.7x10^{-10}$ m/s, ϕ_{clay}=0.7 and $k_{silt} = 1.0x10^{-09}$ m/s, ϕ_{silt}=0.53.

Seepage velocity ($\boldsymbol{v_s}$)

To know if the calculated seepage velocities are high enough to erode the endmember sediments, critical velocities for internal erosion of silt and clay sized sediment, based on different literature sources, have been summarized (5). The minimum critical velocity to erode clay is 0.0019 m/s, while the minimum critical velocity to erode silt is 0.0012 m/s, meaning that a slightly lower fluid velocity is required for erosion of silt. The deductions of the given critical velocities are specified in Table 5 and were either provided directly in the literature (Maslov, 1968; Justin, 1923; Richards & Reddy, 2012; Bonelli, et al., 2007 and Guidoux, et al., 2010) or calculated based on the equations provided in the literature (5).

Sediment classification	Mean grain size (mm)	v_c (m/s)	Velocity equation/source of numbers	Literature source
Clay **Silt**	0.001-0.005 0.005-0.05	0.02- 0.12 0.12- 2.19	Table 11 (numbers from Maslov, 1968 and Justin, 1923)	Briaud, et al. (2019)
Clay **Silt**	0.0016 0.0093	0.22 0.18	(1) $v_c\ (m/s) = 0.1(mean\ particle\ size, mm)^{-0.12}$	Briaud, et al. (2019)
Clay **Silt**	0.0016 0.0093	4.36 1.07	(2) $v_c\ (m/s) = 2.518x10^{-5}(PC^{0.2}\%)(WC^{2.06}\%)(Su^{0.51}kPa)(mean\ particle\ size^{-0.13}mm)0.8$	Briaud, et al. (2019)
Clayey silt **Silt**	CL-ML ML	0.0019 0.0012	Table 5 (Darcy's law - Critical dH/dL of CL-ML= 1.61; critical dH/dL of ML= 3.77)	Richards and Reddy (2012)
Clay **Silt**	0.0016 0.0093	0.01 0.2	Figure 3	Bonelli, et al. (2007)
Clay **Silt**	0.004 0.056	> 0.08 0.02	Table 4	Guidoux, et al. (2010)

Table 5. Summary of critical velocities (v_c) for internal erosion of clay and silt sized sediment, according to various authors. The minimum critical velocities were estimated at 0.0019 m/s for clayey silt and 0.0012 m/s for silt based on Darcy's law calculations . The mean grain sizes are provided from the literature except for the grain sizes providing the equations 1 and 2 (Briaud, et al., 2019) where the average grain size of the endmembers was used. The parameters for equation 2 is percentage clay (PC), percentage water (WC), mean grain size of

the endmember samples of this project, undrained shear strengths (Su) were calculated using the SHANSEP equation ($\text{Su (kPa)} = a * \text{OCR}^b * \sigma'_v$), where the endmember OCR values and MSCL derived in-situ effective stress σ'_v at the depths of the samples (Table 4), and the constants a=0.22, b=0.8 were used and resulted in Su values of 14.5 kPa for silt and 6.8 kPa for clay.

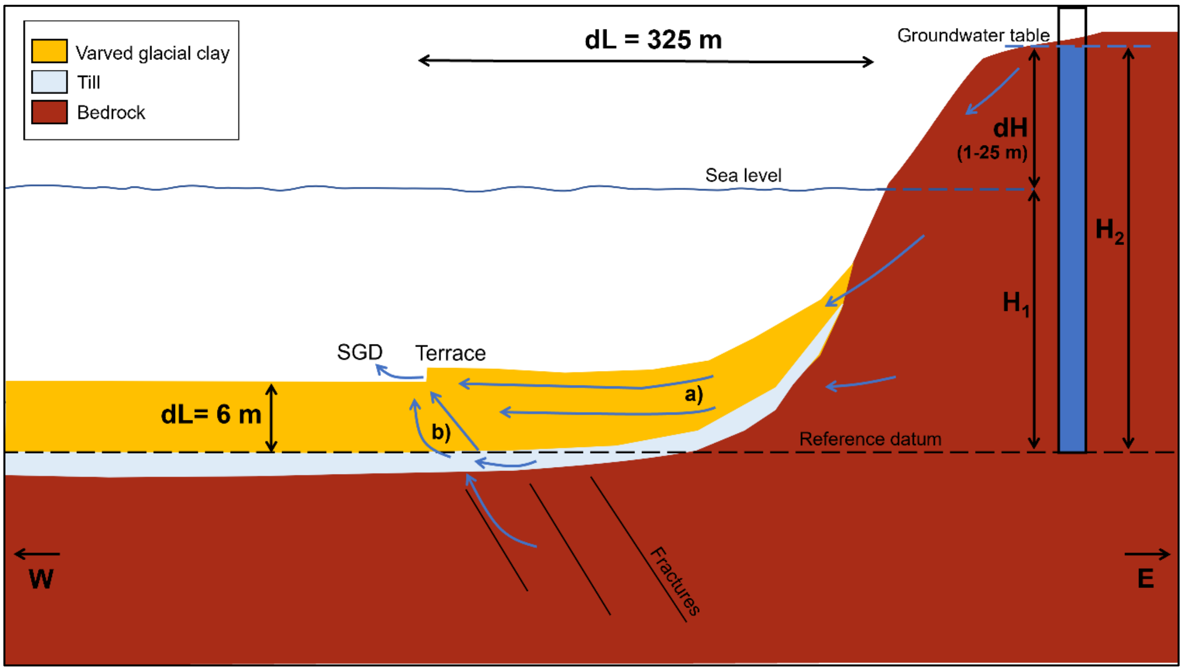

Figure 31. Sketch of the estimated groundwater flow path through the bedrock and varved glacial clay from Fifång shore to the terraces. The dimensional parameters for calculating the fluid flow through the glacial clay using Darcy's law are presented. H_1 is the elevation of the sea level above a reference datum (which is set to the bottom of the glacial clay column), H_2 is the elevation of the groundwater level above the reference datum, dH is the difference between H_1 and H_2, equivalent to the elevation of the groundwater level above the sea level. dL for lateral groundwater flow (a) is the distance between the shore and the terrace at 325 m (Figure 9), dL for vertical or near-vertical/diagonal groundwater flow (b) is the distance the water travels through the glacial clay, which is 6 m (Figure 21).

4.3.2. Calculations

The lateral seepage velocities ($v_{s,lateral}$) generated through the clay-endmember sediment are between 1.5×10^{-12} and 4×10^{-11} m/s, while through the silt-endmember sediment the velocity range is 6×10^{-12} to 1.5×10^{-10} m/s (Equation 12, Figure 32A). The vertical seepage velocities ($v_{s,vertical}$) in the clay-endmember sediment range between 9×10^{-11} m/s and 2×10^{-9} m/s, while through the silt-endmember sediment reaching values from 3×10^{-10} to 8×10^{-9} m/s (Equation 12, Figure 32B). In both flow scenarios, for a specific hydraulic gradient (dH/dL), the silt-enriched endmember allows for higher seepage velocities than the clay-enriched one with the vertical flow model through silty sediment yielding the highest velocity of 8×10^{-9} m/s (Figure 32). This corresponds to 2.5 m/year. However, the velocities are orders of magnitude too low to cause erosion (Table 5).

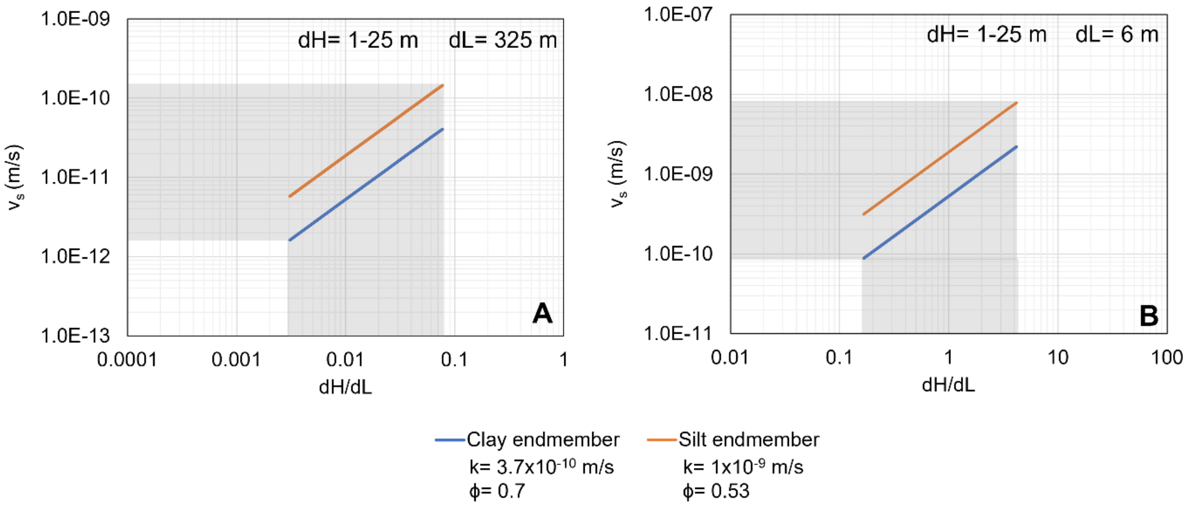

Figure 32. Calculated ranges of seepage velocities (v_s) (m/s) and corresponding hydraulic gradients (dH/dL) for the lateral (A) and vertical (B) groundwater flow models (Figure 31), for the clay-enriched and silt-enriched endmembers based on Darcy's law (Equation 12), using the average hydraulic conductivities and porosities over a 6 m depth (Figure 30). The gray areas mark the lowest and highest velocities of both clay endmembers and the corresponding range in hydraulic gradients. The vertical flow model (B) allows for a higher seepage velocity than the lateral model (A).

As neither lateral nor vertical flow is sufficient to erode the sediment with the given variables, the change in hydraulic head (dH) required to erode the sediments can be calculated based on their critical velocities (Table 5). *Figure 33* illustrates the calculated range of dH/dL for each endmember based on an arbitrarily seepage velocity range of 0.000001-10 m/s according to *v (m/s) = k (dH/dL)* (Equation 12,). The shaded area marks the combined range of the critical velocities required to erode the clay and silt (Table 5) and their corresponding hydraulic gradients (Figure 33). The minimum required gradient to reach the critical velocities required to erode the sediment is $1x10^6$ which corresponds to a minimum dH of $3x10^8$ m for lateral flow and $6x10^6$ m for vertical flow (dH=(dH/dL)*dL). These hydraulic heads are many orders of magnitude too high. For lower hydraulic gradients to be able to yield the critical velocities required to erode the sediments, the permeability needs to be substantially increased.

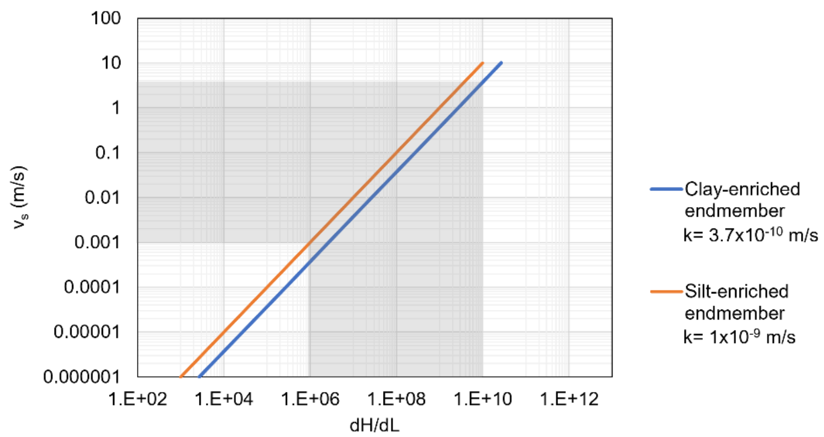

Figure 33. Seepage velocity (v_s) vs hydraulic gradient (dH/dL) graph where the endmember samples are plotted for velocities between $1x10^{-6}$ and 10 m/s based on their hydraulic conductivities (k) according to v (m/s)= k (dH/dL). The grey area shows the range of critical velocities (v_c) required to erode clay and silt according to Table 5, and the corresponding range of hydraulic gradients (dH/dL), with values between $1x10^6$ and $1x10^{10}$. The minimum velocity and dH/dL required to erode the sediment is 0.001 m/s and $6x10^6$, which corresponds to an unrealistically high dH of $3x10^8$ m.

4.4. Sensitivity analysis to theoretically increase the silt content to enhance the hydraulic conductivity.

Since the permeability/ hydraulic conductivity increases with increased silt concentration, a sensitivity analysis is made to see if the hydraulic conductivities at increased hypothetical silt contents from 60 to 100% can generate fluid flows that are sufficient to erode the sediments. This is achieved by 1) estimating the hydraulic conductivities that are required for erosion to occur in the two lateral and vertical flow scenarios, and 2) calculating if an increase in silt content could produce that level of hydraulic conductivity.

The minimum range of hydraulic conductivities required to erode silt in each flow scenario (lateral and vertical) was calculated by ***k*** (m/s) = $v_c/(dH/dL)$ (Equation 12 rearranged without porosity), where the critical velocity (v_c) is the minimum critical velocity required to erode silt (=0.001 m/s) (Richards & Reddy. 2012, Table 5), dH is a range from 1-25 m and dL= 325 for the lateral flow model, and 6 m for vertical flow model (Figure 34). The estimated minimum required hydraulic conductivity needed to cause erosion of silt is $1.3x10^{-2}$ m/s for lateral flow and $2.4x10^{-4}$ m/s for vertical flow (Figure 34). The hydraulic conductivity that Richards & Reddy (2012) used for their calculations that resulted in a critical velocity of 0.001 m/s is within this range (Table 5), but according to a table of permeabilities from Freeze & Cherry (1979) (Figure 35), these values rather correspond to the hydraulic conductivity of sand and not clay. This indicates that the minimum critical velocity of 0.001 m/s from Richards & Reddy (2012) may be too low to represent erosion through silty varves in glacial clay.

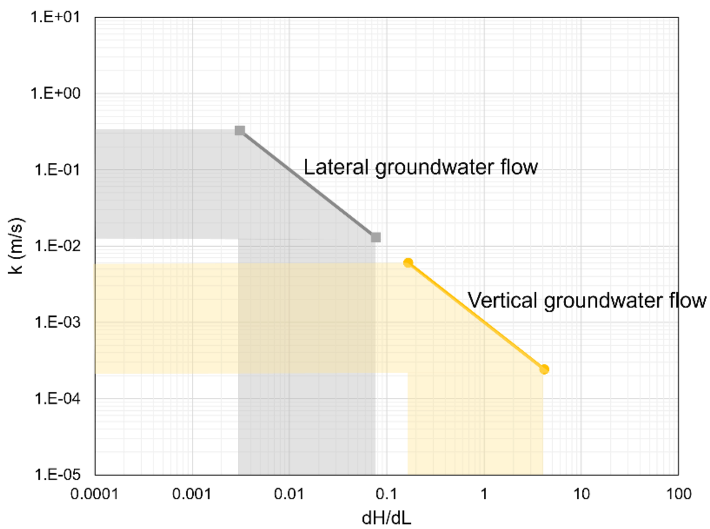

Figure 34. The range of required hydraulic conductivities (k) to erode silt based on the minimum critical velocity to erode silt of 0.001 m/s (Table 5) for the lateral (dL=325 m, dH=1-25 m), and vertical (dL=6 m, dH= 1-25 m) flow model. The highest dH/dL require the lowest k to yield the critical velocity of 0.001 m/s, with the vertical flow model requiring the lowest k of $2.4x10^{-4}$ m/s.

The best fit equation for the ***k***-ϕ relationship along the VCL for each consolidation sample (as done in Figure 29) was used to estimate the hydraulic conductivities of the samples at arbitrary porosities of 0.5, 0.7 and 0.9 (Table 6A). Then the relationship between all the samples' estimated k- at a specific porosity- and their measured silt content was obtained (Figure 36). The resulting best fit equations from each graph (Figure 36A-C) represent the relationship between the hydraulic conductivity and silt content at a specific porosity throughout the core and were subsequently used to calculate the hypothetical hydraulic conductivities at increased hypothetical silt contents from 60 to 100 % (Table 6B). The results show that the hydraulic conductivity is that of silt (10^{-9} m/s, Figure 35) when either the porosity is > 0.7 with a silt content >27 % (Table 6A), or when the porosity is >0.5 and the silt content exceeds 70 % (Table 6B). But even at 90% porosity and 100% silt, the hydraulic conductivity of $8.12x10^{-7}$ m/s (Table 6B) remains too low to yield a minimum critical seepage velocity of 0.001 m/s based on the hydraulic gradients in the study area (Figure 34). Therefore, based on these calculations the velocities of water through the silty varves in the glacial clay in the research area will not be high enough to cause erosion if driven by the hydraulic head imposed by the local groundwater table. According to Figure 34 (where the minimum critical velocity corresponds to a minimum k of 10^{-4} m/s) and Figure 35, for erosion to occur in the research area the sediment would need to be silty sand or larger sized material (with k= >10^{-4} m/s).

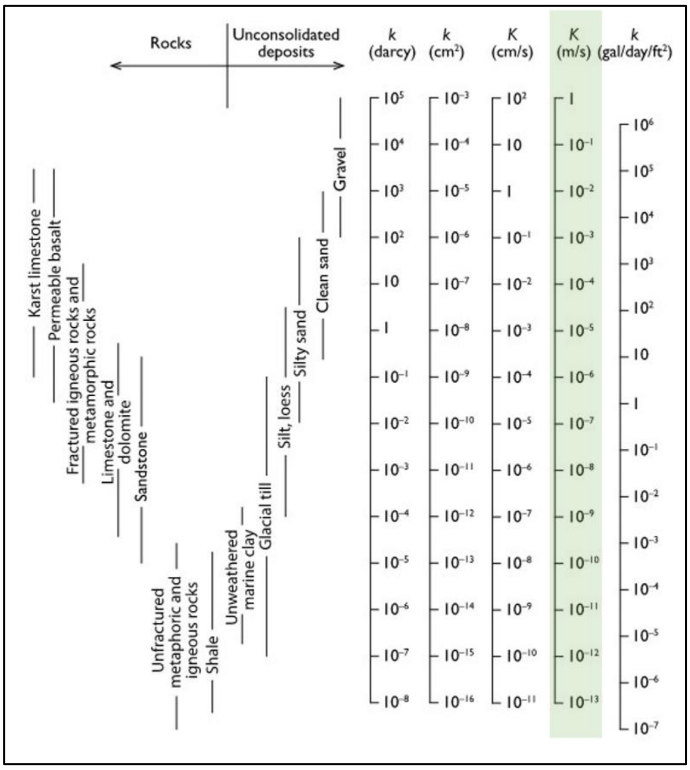

Figure 35. Ranges of hydraulic conductivities and permeabilities for different sediment types and rocks . The column marked in green is the values in terms of hydraulic conductivity (m/s). The hydraulic conductivity for silt range between 10^{-9} and 10^{-5} m/s.

A	Measured fractional % silt	Sample ID	*k* (m/s) using ϕ = 0.5	*k* (m/s) at ϕ = 0.7	*k* (m/s) at ϕ = 0.9
	0.25	EL0-IGV07-2PC-SEC 2-0-3	1.57E-11	3.48E-10	7.72E-09
	0.05	EL0-IGV07-2PC-SEC 2-4-7	4.11E-11	8.70E-10	1.84E-08
	0.27	EL0-IGV07-2PC-SEC 2-147-152-A	2.30E-10	2.48E-09	2.68E-08
	0.46	EL0-IGV07-2PC-SEC 2-147-152-B	1.34E-10	2.48E-09	4.61E-08
	0.49	EL0-IGV07-2PC-SEC 3-120-125	3.90E-10	6.12E-09	9.59E-08
	0.53	EL0-IGV07-2PC-SEC 3-130-136	6.75E-10	9.66E-09	1.38E-07
	-	EL0-IGV07-2PC-SEC 3-136-142	9.38E-10	1.10E-08	1.29E-07
B	**Hypothetical fractional % silt**		***k* (m/s) at ϕ = 0.5**	***k* (m/s) at ϕ = 0.7**	***k* (m/s) at ϕ = 0.9**
	0.6		6.02E-10	8.78E-09	1.28E-07
	0.7		1.06E-09	1.47E-08	2.03E-07
	0.8		1.87E-09	2.46E-08	3.22E-07
	0.9		3.31E-09	4.11E-08	5.12E-07
	1		5.83E-09	6.88E-08	8.12E-07

Table 6. Measured and hypothetically calculated silt contents (%) and corresponding hydraulic conductivities (k) at specific arbitrary porosities (ϕ). A: The consolidation samples from which grain size measurements were made (Table 3) with the measured % silt for each sample and their estimated hydraulic conductivity (k) for a specific porosity (calculated from the k- ϕ relationship along the VCL of each sample) . B: Hypothetical values of increased silt (%) and the corresponding hydraulic conductivities at specific porosities (calculated from the best fit equation between the estimated k-values for the samples at specific porosities and their measured silt % from Table 6A (Figure 36)).

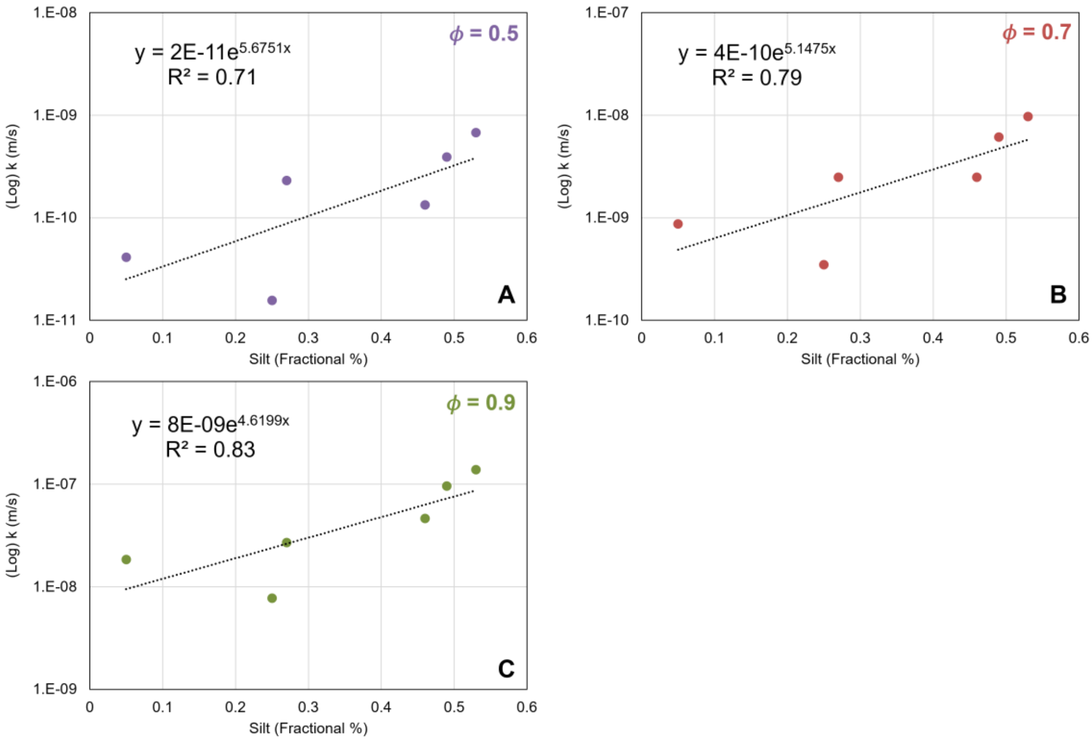

Figure 36. The relationship between the estimated hydraulic conductivities (k) of the samples and their measured silt % for a hypothetical porosity of 0.5 (A), 0.7 (B), 0.9 (C), with values obtained from Table 6A.

4.5. Permeability and other suggested groundwater flow paths

Anisotropy

Another aspect where the hydraulic conductivity/permeability is enhanced is to consider anisotropy in the sediment along the varved layers in the glacial clay . Fluids will flow more easily along the varved layers than across them. The one-dimensional consolidation test, which was used for this project, measures the vertical hydraulic conductivity in the direction of the applied stress. Thus, when a varved clay is consolidated, the permeability is measured across the layers, giving a lower value than if measured horizontally along the varved layers. For this reason, the hydraulic conductivities that were measured and used for the groundwater flow calculations may be underestimated. However, as the varves have shown to be tilted in cores EL20-IGV07-1PC and EL20-IGV07-2PC (Figure 24), the measured hydraulic conductivities may represent an average of the vertical and horizontal permeability of the sediment. Nevertheless, to obtain the real permeability parallel to the varves, other consolidation tests would need to be used where drainage is only permitted in the horizontal direction. These anisotropy measurements would need to be made on samples where the varves were horizontally oriented and not inclined. This could be established by x-raying the cores prior to selecting sample locations.

Fractures and piping erosion

Higher permeability could also come from the presence of fractures in the sediment, through which the groundwater could flow . These fractures could have arisen during isostatic uplift, from reactivation of pre-existing older faults in the bedrock by rapid ice retreat , as suggested for groundwater flow in Lake Vättern . On Fifång there are NW-SE trending fault zones (Figure 6A), which potentially could serve as groundwater conduits if they are open and allow for piping erosion along the walls of the fractures, which in turn will increase the permeability further (Bonelli, et al., 2013; Werner, et al., 2020). However, fractures do not necessary yield higher permeability as they can also serve as barriers to fluid flow , therefore further investigations of the fault system in the research area are necessary to consider this potential flow path. Piping erosion could also have formed in the grain contact between the silt-rich and clay-rich varves of the glacial clay, through which the water is channelized with higher velocity than within the porous network of the silt. Holes in the terraces support such a theory (Figure 11), however it is highly speculative and further investigations of piping erosion is needed to accurately evaluate this form of erosion in the area.

Suggested flow path

As the hydraulic conductivity to erode the sediments needs to be in the range of 10^{-2} m/s for horizontal flow and 10^{-4} m/s for vertical flow (Figure 34), which equals to that of sand or higher (Figure 35) the suggested flow path for SGD at the terraces is initially laterally, either through a till/sand layer which drapes the bedrock or in the interface between glacial clay and bedrock (if till is not present), or laterally through fractures in the bedrock, and subsequently ascending vertically through fractures in the glacial clay or through pipes in the tilted varves (Figure 31). Similar fluid flow paths have been suggested by other studies where the groundwater system is suggested to transport laterally through glaciofluvial deposits and discharge vertically through faults (Berndt, 2005; Preto, et al., 2019) or where the overburden sediments with low permeability are thinner (Hillman, et al., 2015; Preto, et al., 2019; Virtasalo, et al., 2019). The presence of terraces and fluids in the glacial clay and absence of both in the overlying sediments in deeper waters (Figure 15), indicate that the overlying younger sediments act as a cap on top of the glacial clay, which prevents the water from escaping. Therefore, even though erosion of the terraces from groundwater flow through the porous network of silty varves around Fifång is unlikely, channelized fluid flow and piping erosion through the varved glacial clay and through fractures remains possible.

An alternative source of the upwelling fluids potentially seen in sub-bottom profiles could be by seepage of over pressurized fluids or gas, or from salinity driven convection cells (Goff, et al., 2019 and Gustafson, et al., 2019). Thus, any water emerging from the sediment could be old (from the last glacial maximum) and therefore not primarily driven by the hydraulic head of the local groundwater water table.

5. Conclusions

- The terraces in the survey area exclusively form in glacial clay where overlying glacial and postglacial sediments have been eroded. Erosion likely occurred due to isostatic uplift after the retreat of the Fennoscandian Ice Sheet. This is supported by the measured overconsolidation ratio (OCR) on the consolidation samples, which indicate that 8-14 m of sediment have been eroded.

- Geotechnical tests show that there is a strong correlation between grain size, hydraulic conductivity, and porosity. Generally, at a given effective stress (burial depth) the silt-enriched sediment will have a lower porosity/void ratio than clay-enriched sediment, but at a given porosity/void ratio the silt-enriched sediment will have a higher hydraulic conductivity. Despite a lower porosity at a given burial depth, the silt-enriched endmember retains a hydraulic conductivity that is about 1 order of magnitude higher than the clay rich endmember.

- Based on the geophysical mapping, the terraces near Fifång are probably the most likely to generate groundwater flow in the survey area as they are closer to the shore than the other terraces in the area (Figure 5), which yields higher hydraulic gradients. Nevertheless, calculations using Darcy’s Law illustrate that neither lateral nor vertical groundwater flow can likely attain velocities to cause erosion of the glacial clays. The generated seepage velocities, based on the dimensions of the proposed area of groundwater flow, and the hydraulic conductivity and porosity of the sediment, are not high enough to reach required critical velocities that are reported in the literature for fine-grained sediments.

Suggestions for future work

A suggestion for future work is to investigate groundwater channelized through fractures and piping erosion in the sediment to better constrain the critical velocities required for erosion. To test this requires other experimental tests (piping tests). Another suggestion is to investigate the permeabilities of the terrestrial part of the groundwater path to complement the findings of this study. This includes to investigate the local fault zones and conduct new groundwater measurements on Fifång, preferably on several locations as Fifång has two bedrock regimes that could alter the capacity to store groundwater. The anisotropic permeability of the glacial clay could be investigated by laterally drained consolidation tests if the orientation of the varves could be established prior to sampling using x-radiography.

Acknowledgements

I want to thank my supervisors Martin Jakobsson and Matt O’Regan at Stockholm University for the help and guidance during this project.

References

Andrén, T., Björck, S., Andrén, E., Conley, D., Zillén, L., & Johanna, A. (2011). The Development of the Baltic Sea Basin During. i J. H. al. (Red.), The Baltic Sea Basin (ss. 75-97). Springer-Verlag Berlin Heidelberg.

ASTM. (2006). Standard test methods for one-dimensional consolidation properties of soils using incremental loading developed by subcommittee. D2435-04. Method B. Philadelphia, PA.: ASTM.

Berndt, C. (2005). Focused fluid flow in passive continental margins. Phil. Trans. R. Soc. A, 363, 2855-2871.

Björck, S. (1995). A REVIEW OF THE HISTORY OF THE BALTIC SEA, 13.0-8.0 ka BP. Quaternary lnternational, 27, 19-40.

Bonelli, S., Benahmed, N., & Fell, R. (2013). Erosion in Geomechanics Applied to Dams and Levees. John Wiley & Sons, Incorporated.

Bonelli, S., Marot, D., Ternat, F., & Benahmed, N. (2007). Criteria of erosion for cohesive soils. Symposium of the European Working Group of ICOLD: hal-01007477, 45-59.

Briaud, J.-L., Shafii, I., Chen, H.-C., & Medina-Cetina, Z. (2019). Relationship Between Erodibility and Properties of Soils. National Academies of Sciences, Engineering, and Medicine.

Burnett, W. C., Bokuniewicz, H., Huettel, M., Moore, W. S., & Taniguchi, M. (2003). Groundwater and pore water inputs to the coastal zone. Biogeochemistry, 66, 3-33.

Burnett, W., Aggarwal, P., Aureli, A., Bokuniewicz, H., Cable, J., Charette, M., . . . Rajar. (2006). Quantifying submarine groundwater discharge in the coastal zone via multiple methods. Science of the Total Environment, 367, 498–543.

Cho, H.-M., Kim, G., Kwon, E., Moosdorf, N., Garcia-Orellana, J., & Santos, I. R. (2018). Radium tracing nutrient inputs through submarine groundwater discharge in the global ocean. Nature Sci. Rep., 8:2439.

Dunne, T. (1990). Hydrology and mechanics of erosion by subsurface flow. i Groundwater geomorphology; the role of subsurface water in earth-surface processes and landforms. Geologic society of america, special paper 252.

Franke, R. (1982). Smooth interpolation of scattered data by local thin plate splines. Computers & Mathematics with Applications, 8(4), 273-281.

Freeze, A., & Cherry, J. (1979). Groundwater. Englewood Cliffs, N.J: Prentice-Hall, Inc.

Goff, J. A. (2019). Modern and Fossil Pockmarks in the New England Mud Patch: Implications for Submarine Groundwater Discharge on the Middle Shelf. Geophysical Research Letters, 46, 12,213-12,220.

Grabowski, R. C., Droppo, I. G., & Wharton, G. (2011). Erodibility of cohesive sediment: The importance of sediment properties. Earth-Science reviews , 105, 101-120.

Gustafson, C., Key, K., & Evans, R. L. (2019). Aquifer systems extending far offshore on the U.S Atlantic margin. Nature, 9, 1-9.

Higgins, C. G. (1982). Piping and sapping: development of landforms by groundwater outflow. Groundwater as a Geomorphic Agent: Binghamton Geomorphology Symposium 13, 18.

Hillman, J. I., Gorman, A. R., & Pecher, I. A. (2015). Geostatistical analysis of seafloor depressions on the southeast margin of New Zealand's South Island — Investigating the impact of dynamic near seafloor processes on geomorphology. Marine Geology, 360, 70-83.

Holtz, R. D., Kovacs, W. D., & Sheahan, T. C. (2011). An introduction to geotechnical engineering (2nd uppl.). NJ: Pearson Education, Inc.

Howard, A. D. (1988). Introduction: Groundwater sapping on Mars and Earth. Sapping features of the Colorado Plateau, NASA SP-491, 1-5.

Hwang, D.-W., Kim, G., Lee, Y.-W., & Yang, H.-S. (2005). Estimating submarine inputs of groundwater and nutrients to a coastal bay using radium isotopes. Marine Chemistry, 96, 61-71.

International Hydrographic Organization, I. O. (2018). The IHO-IOC GEBCO Cook Book.
Jakobsson, M., Björck, S., Alm, G., Andrén, T., Lindeberg, G., & Svensson, N.-O. (2007). Reconstructing the Younger Dryas ice dammed lake in. Global and Planetary Change, 57, 355–370.

Jakobsson, M., Björck, S., O'Regan, M., Flodén, T., Greenwood, S. L., Swärd, H., . . . Skelton, A. (2014). Major earthquake at the Pleistocene-Holocene transition in Lake Vättern, southern Sweden. Geology, 42(5), 379-382.

Jakobsson, M., Gyllencreutz, R., Mayer, L., Dowdeswell, J., Canals, M., Todd, B., . . . Larter, R. (2016). Mapping submarine glacial landforms using acoustic methods. Atlas of Submarine Glacial Landforms: Modern, Quarternary and Ancient. Geological Society, London, Memoirs, 46, 1-8.

Jakobsson, M., O'Regan, M., Mörth, C.-M., Stranne, C., Weidner, E., Hansson, J., . . . Sjöström, A. (2020). Potential links between Baltic Sea submarine terraces and groundwater seeping . Earth Surface Dynamics, 8, 1-15.

Johannes, R. E. (1980). The ecological significance of the submarine discharge of groundwater. Marine Ecology, 3, 365-373.

Jose, B. T., Sridharan, A., & Abraham, B. M. (1989). Log-Log Method for Determination of Preconsolidation Pressure. Geotechnical Testing Journal, 12(3), 230-237.

Kim, G., & Lee, K.-K. (2003). Large submarine groundwater discharge (SGD) from a volcanic island. Geophysical research letters, 30(21), 1-3.

Kim, I., & Kim, G. (2011). Large fluxes of rare earth elements through submarine groundwater discharge (SGD) from a volcanic island, Jeju, Korea. Marine Chemistry, 127, 12-19.

Larsson, R., Sällfors, G., Bengtsson, P.-E., Alen, C., Bergdahl, U., & Eriksson, L. (2007). Skjuvhållfasthet - utvärdering i kohesionsjord - Information 3. Linköping: Swedish Geotechnical Institute .

Luijendijk, E., Gleeson, T., & Moosdorf, N. (2020). Fresh groundwater discharge insignificant forthe world’s oceans but important for coastalecosystems. Nature Communications, 11:1260.

Lundqvist, J., & Wohlfarth, B. (2001). Timing and east-west correlation of south Swedish ice marginal lines during the Late Weichselian. Quaternary Science Reviews, 20, 1127-1148.

Lurton, X. (2016). An introduction to Underwater Acoustics (2nd edition). Springer-Verlag Berlin and Heidelberg GmbH & Co. KG.

Moore, W. S., Sarmiento, J. L., & Key, R. M. (2008). Submarine groundwater discharge revealed by ^{228}Ra distribution in the upper Atlantic Ocean. Nature Geoscience , 1, 309-311.

O'Regan, M., Greenwood, S. L., Preto, P., Swärd, H., & Jakobsson, M. (2016). Geotechnical and sedimentary evidence for thick-grounded ice in southern Lake Vättern during deglaciation. GFF, 138(2), 355-366.

Peltonen, K. (2002). Direct groundwater inflow to the Baltic Sea. Copenhagen: Nordic Council of Ministers.

Preto, P., Stranne, C., Greenwood, S., Jakobsson, M., Näslund, J.-O., Sundberg, J., . . . O'Regan, M. (2019). Geothermal evidence for groundwater flow through Quaternary sediments overlying bedrock aquifers below Lake Vättern, Sweden. GFF, 141(2), 106-120.

Rankka, K., Andersson-Sköld, Y., Hultén, C., Larsson, R., Leroux, V., & Dahlin, T. (2004). Quick clay in Sweden. Linköping: SGI.

Rasmussen, S. O., Andersen, K. K., Svensson, A. M., Steffensen, J. P., Vinther, B. M., Clausen, H. B., . . . Ruth, U. (2006). A new Greenland ice core chronology for the last glacialtermination. Journal of geophysical research, 111, 1-16.

Richards, K. S., & Reddy, K. R. (2012). Experimental investigation of initiation of backward erosion piping in soils. Géotechnique , 62(10), 933-942.

Robb, J. M. (1984). Spring sapping on the lower continental slope offshore New Jersey. Geology, 12, 278-282.

Rodellas, V., Garcia-Orellana, J., Masqué, P., Feldman, M., & Weinstein, Y. (2015). Submarine groundwater discharge as a major source of nutrients to the Mediterranean Sea. PNAS, 112(13), 3926-3930.

Schneider, J., Flemings, P. B., Day-Stirrat, R. J., & Germaine, J. T. (2011). Insights into pore-scale controls on mudstone permeability through resedimentation experiments. Geology, 39, 1011–1014.

Shackleton, C., Patton, H., Hubbard, A., Winsborrow, M., Kingslake, J., Esteves, M., . . . Greenwood, S. L. (2018). Subglacial water storage and drainage beneath the Fennoscandian and. Quartenary Science Reviews , 201, 13-28.

Soderberg, P., & Flodén, T. (1992). Gas seepages, gas eruptions and degassing structures in the seafloor along the Strömma tectonic lineament in the crystalline Stockholm Archipelago, east Sweden. Continental Shelf Research , 12(10), 1157-1171.

Soderberg, P., & Flodén, T. (1997). Stratabound submarine terraces and pockmarks - indicators of spring sapping in glacial clay, Stockholm Archipelago, Sweden. Proceedings of the Forth Marine Geological Conference - the Baltic, 173-178.

Stieglitz, T. (2005). Submarine groundwater discharge into the near-shore zone of the Great Barrier Reef, Australia. Marine Pollution Bulletin, 51, 51-59.

Swärd, H., O'Reagan, M., Björck, S., Greenwood, S. L., Kylander, M., Mörth, C.-M., . . . Jakobsson, M. (2018). A chronology of environmental changes in the Lake V€attern basin from. Boreas, 47, 609–624.

Swärd, H., O'Regan, M., Ampel, L., Ananyev, R., Chernykh, D., Flodén, T., . . . Jakobsson, M. (2016). Regional deglaciation and postglacial lake development as reflected in a 74 m sedimentary. GFF, 138:2, 336-354.

Taner, T. M. (2001). Seismic attributes. Recorder, 26(7).

Taniguchi, M., Burnett, W. C., Cable, J. E., & Turner, J. V. (2002). Investigation of submarine groundwater discharge. Hydrological Processes , 16, 2115–2129.

Taniguchi, M., Dulai, H., Burnett, K. M., Santos, I. R., Sugimoto, R., Stieglitz, T., . . . Burnett, W. C. (2019). Submarine Groundwater Discharge: Updates on its measurement techniques, geophysical drivers, magnitudes, and effects. Front. Environ. Sci, 7(141), 1-26.

Taylor, D. W. (1948). Fundamentals of soil mechanics. New York: Wiley and Sons, Inc.

Terzaghi, K. (1925). Erdbaumechanik auf bodenphysikalischer grundlage. Leipzig and Wien: F. Deuticke.

Venkatramaiah, C. (2006). Geotechnical engineering. New Dehli: New Age International Pvt Ltd Publishers.

Virtasalo, J. J., Schröder, J. F., Luoma, S., Majaniemi, J., Mursu, J., & Scholten, J. (2019). Submarine groundwater discharge site in the First Salpausselkä ice-marginal formation, south Finland. Solid Earth, 10, 405–423.

Wan, C., & Fell, R. (2008). Assessing the Potential of Internal Instability and Suffusionin Embankment Dams and Their Foundations. Journal of geotechnical and geoenvironmental engineering , 134(3), 401-407.

Wentworth, C. K. (1922). A scale of Grade and Class Terms for Clastic Sediments. The journal of Geology, 30(5), 377-392.

Werner, A. D., Jazayeri, A., & Ramirez-Lagunas, M. (2020). Sediment mobilisation and release through groundwater discharge to the land surface: Review and theoretical developement. Science of the Total Environment , 714, 1-17.

Zahidul, K., & Kulesza, S. (2020). Soil properties affecting the onset of erosion in cohesive soils. Kansas.

Appendices

Appendix A- OpendTect detailed method

Software nomenclature

OpendTect is a software that was developed to first and foremost handle 3D-seismic data, while the collected multibeam echo soundings and sub-bottom seismic profiles provide 2D-seismic data. For this reason, the nomenclature in OpendTect is used for 3D-seismics and several terms are different from what is used when handling 2D-seismics. In the following section some terms that are essential for understanding the OpendTect software are briefly described.

Inlines, crosslines and z-lines refer to the lines that make up a 3D-data set in the form of a cube. The inlines refer to the boat track direction during profiling while crosslines are perpendicular to the inlines. The z-line dimension corresponds to the depth in either distance or time. For sub-bottom profiling only the inlines and z-lines contain data while multibeam surveys contain data in the crossline direction and inline direction. However, as the data gathered for this project was in 2D, the sub-bottom lines/profiles were imported as 2D-seismic lines with their directions in cartesian coordinates (x, y, z) and not as inlines or crosslines.

Survey steps refer to the resolution of the data, where the number of steps correspond to the range of data to be included in the project. For steps regarding inlines and crosslines, a step of, for example, 10 means that there will be data input every tenth inline and crossline. For steps on the z-line, a step of 10 means that every 10^{th} unit of distance or time, data input occurs. The survey setup of the project had an in-line and crossline range step of 1, and a z-range step of 0.1ms.

Bins are areas along the lines in which the data is sorted into. The amount of data that gets sorted into one bin depends on how big you set the bin to be. In this project the inline/crossline bin size was set to 1 m/line.

Surface gridding with LTPS

All algorithms available in the plugin (LTPS, multilevel B splines, inverse distance weighted, nearest neighbor) were tested by gridding the surface of the seabed reflector and comparing it to the multibeam bathymetry grid, whereby Local thin plate spline LTPS had the best fit (Figure A1). This is important as it implies that the fit is likely good for the grids of the other reflectors too.

The setup for gridding with LTPS:

- In-line and crossline steps of 10. A step of 1 was tried and failed due to the high computational load and resulting in slow gridding speed. This means that each grid cell (created by the crossings of the inline and crossline) has a horizontal resolution of 10 lines. In other words, the algorithm will output a horizon every tenth inline/crossline. The distance of these steps will vary as the distance between inlines vary.
- Search radius of 800 m (which equals to the maximum sub-bottom profile-line spacing of the area).
- 5 maximum points per sector.

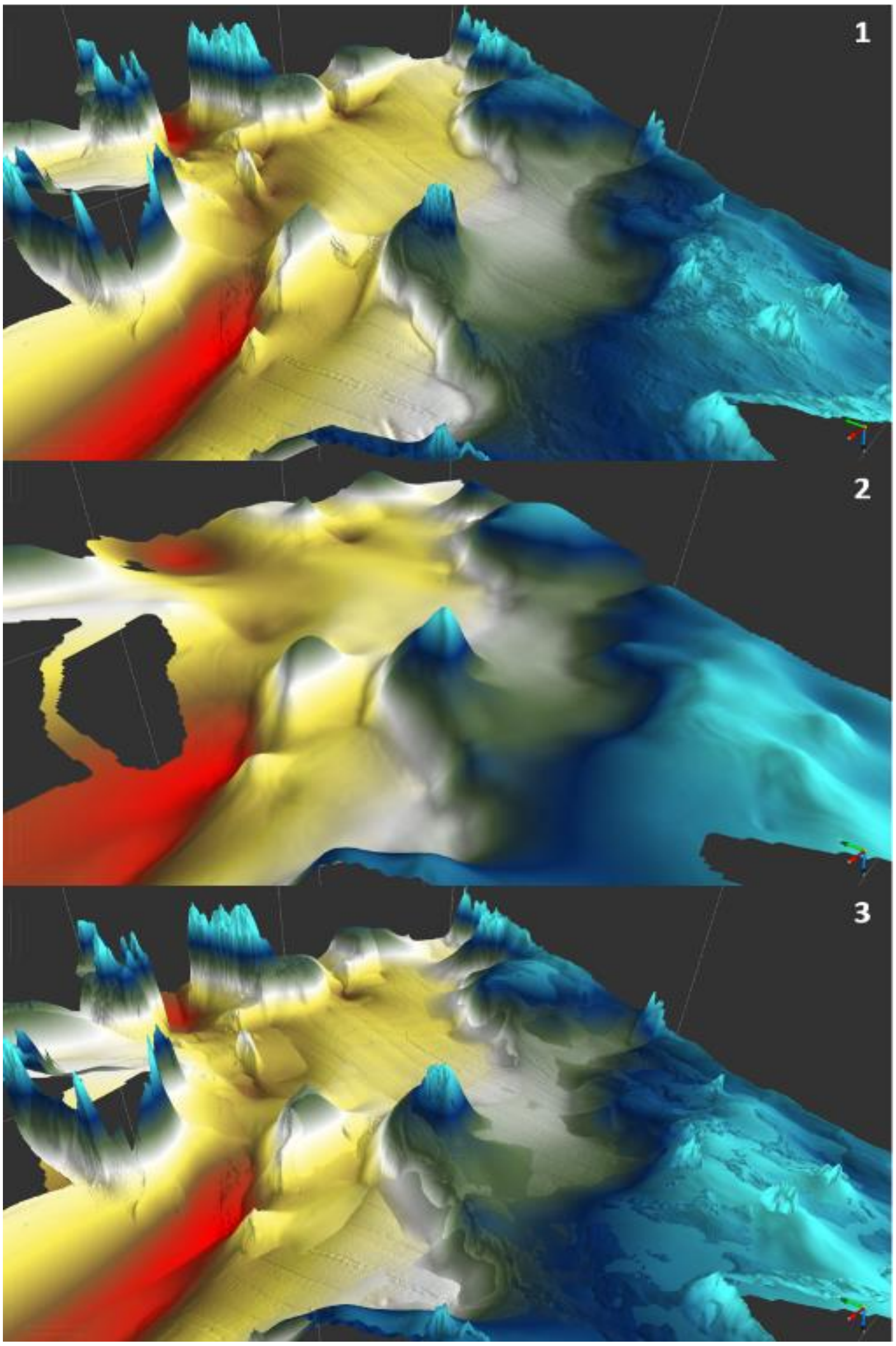

Figure A1. The gridded multibeam bathymetry compared to the LTPS-gridded digitized seafloor reflector, displayed in the OpendTect 3D-viewer. 1: The multibeam bathymetry. 2: LTPS gridded seafloor surface. 3: Both grids displayed together. The LTPS shows a good fit with the exceptions of some elevation peaks which have been missed by the LTPS algorithm, possibly due to sparseness of the subbottom profiles.

Appendix B- Geotechnical properties from the consolidation test data

For each load increment the ICON P software measures the change in sediment height (ΔH, cm) during consolidation and the time required for completion of the load step. From these measurements, together with the dimensions and mass of the wet/dry sample prior/after the consolidation test, the following calculation steps are made by the ICON P software . For sample EL20-IGV07-2PC-130-136 the wrong sample diameter was entered into the software, which led to inaccurate test results, and therefore these steps were calculated manually.

Using the mass of the dry sample (M_s, g), sample area (A, cm^2), specific gravity (G_s , g/cm^3) (by using the measured grain density (ρ_G, g/cm^3) and an assumed fluid density (ρ_f) of 1 g/cm^3), the equivalent height of each solid sample (H_s, cm) is obtained following:

$$H_s = \frac{M_s}{G_s \, \rho_w A} \qquad (B1)$$

The void ratio prior to the start of the consolidation test ($e_{0,initial}$) is calculated using the initial saturated sample height ($H_{0,initial}$, cm) and the height of the solid sample (H_s, cm):

$$e_{0,initial} = \frac{(H_{0,initial} - H_s)A}{H_s A} \qquad (B2)$$

And the final void ratio after the end of the test (e_f) is calculated based on the difference between the final height of the test (H_f, cm) and the solid sample height according to:

$$e_f = \frac{(H_f - H_s)A}{H_s A} \qquad (B3)$$

At each incremental load step, the incremental void ratio (e_i) is calculated using the void ratio at the start of the load step (e_1), the change in sediment height (ΔH_i, cm) and the equivalent height of the solid sample by:

$$e_i = e_1 - \frac{\Delta H_i}{H_s} \qquad (B4)$$

The incremental vertical strain, $\varepsilon_{v,i}$ (%), for each load increment is calculated using the change in height (ΔH) between the initial height of the sample prior to the consolidation test ($H_{0,initial}$, cm) and the height at the end of each load step (ΔH_{i2}, cm) following:

$$\varepsilon_{v,i}\ (\%) = \frac{\Delta H}{H_{0,initial}} * 100 \qquad (B5)$$

From the strain calculations, the coefficient of volume compression (M_V, 1/kPa) is calculated using the fractional change in strain ($\Delta\varepsilon$) and change in effective stress ($\Delta\sigma'_v$, kPa) from the beginning to the end of each load step:

$$M_V = \frac{\Delta\varepsilon/100}{\Delta\sigma'_v} \qquad (B6)$$

The coefficient of consolidation (C_V, cm^2/s) which essentially controls the speed of consolidation, is calculated using square root of time fitting method:

$$C_V = \frac{T_{90} D^2}{t_{90}} \quad (B7)$$

Where

T_{90} = 0.848 = the time factor at 90 % consolidation from Terzaghi's 1D consolidation theory .

t_{90} = time (seconds) for 90 % consolidation for the load step.

D^2 = drainage path (cm) = calculated as half the average thickness during the load step:

$$D = \frac{H_{i,1} + H_{i,2}}{4} \quad (B8)$$

where

$H_{i,1}$ = sample height at the beginning of the load step

$H_{i,2}$ = sample height at the end of the load step

The hydraulic conductivity (k, cm/s) at each load step is calculated with an assumed unit weight of water (γ_w) of 1 g/cm^3*g (or 1000 N/m^3) following:

$$k = M_V C_V \gamma_w \quad (B9)$$

From the hydraulic conductivity the intrinsic permeability, K (cm^2) is calculated by using the hydraulic conductivity in units of m/s and converting K to cm^2 by multiplying the equation by 10^4:

$$K = \frac{k \eta_w}{g} 10^4 \quad (B10)$$

Where

η_w = Kinetic viscosity of water at 20°C (1.007x10^{-6} m^2/s)

Appendix C – Isopach maps

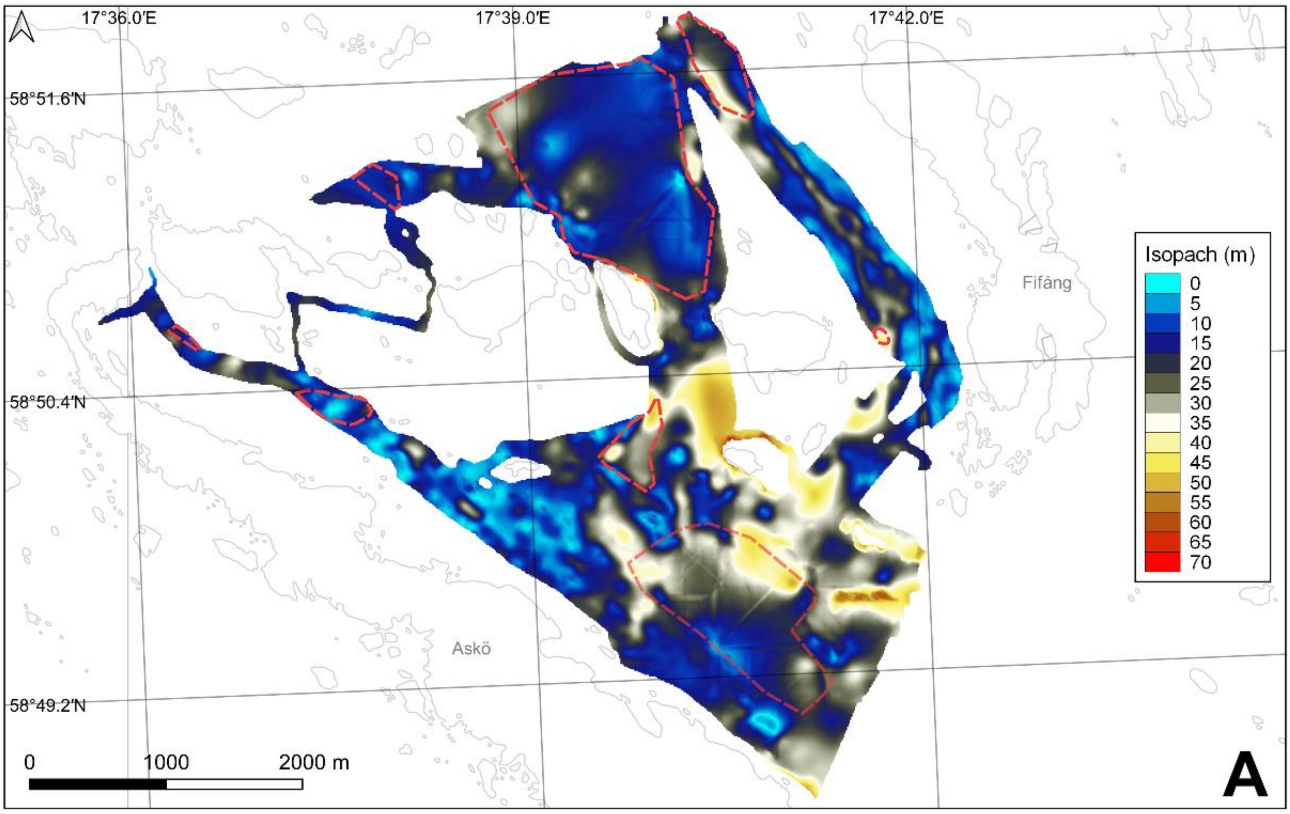

Figure C1. Isopach between S-1 and multibeam bathymetry (the total sediment thickness). Red markings indicate where the data is uncertain due to blanks in the stratigraphy of the sub-bottom profiles.

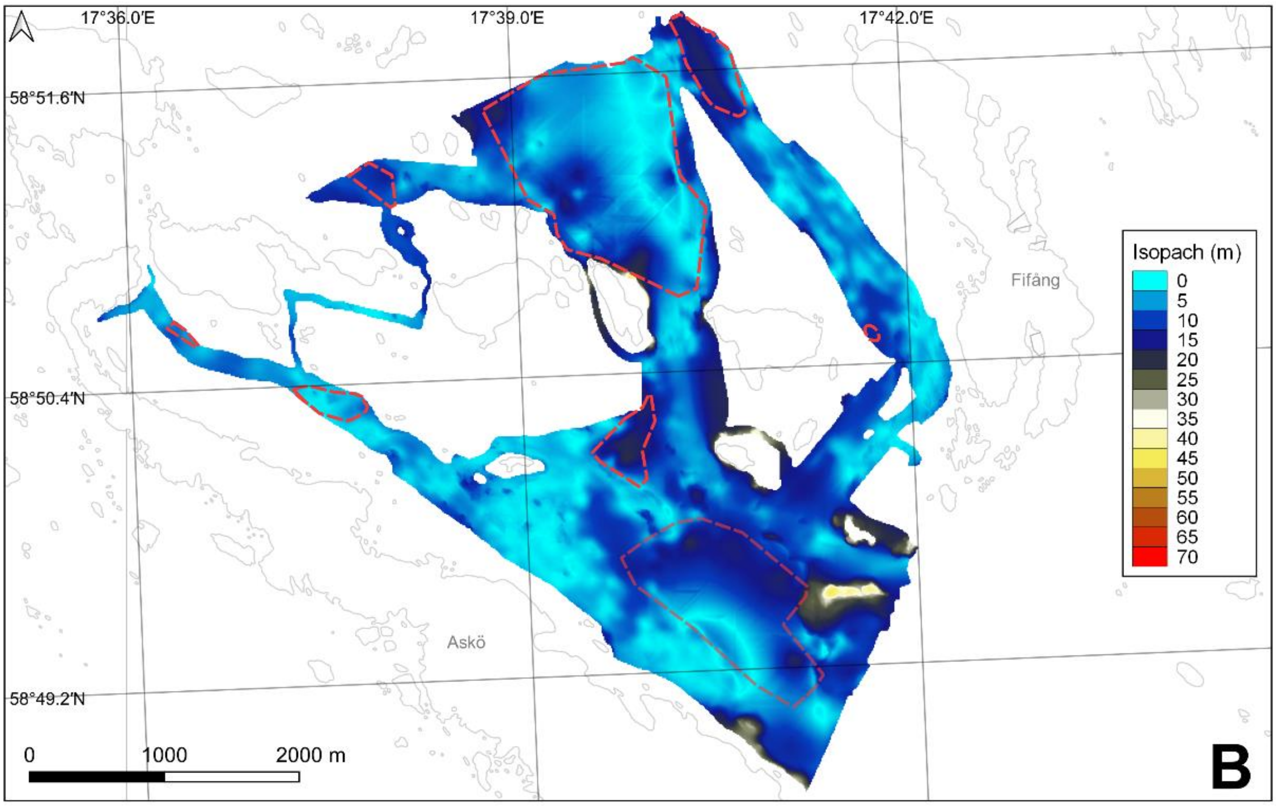

Figure C2. Isopach between S-2 and the multibeam bathymetry (combined thickness of acoustic Unit 2, 3, 4 and 5). Red markings indicate where the data is uncertain due to blanks in the stratigraphy of the sub-bottom profiles.

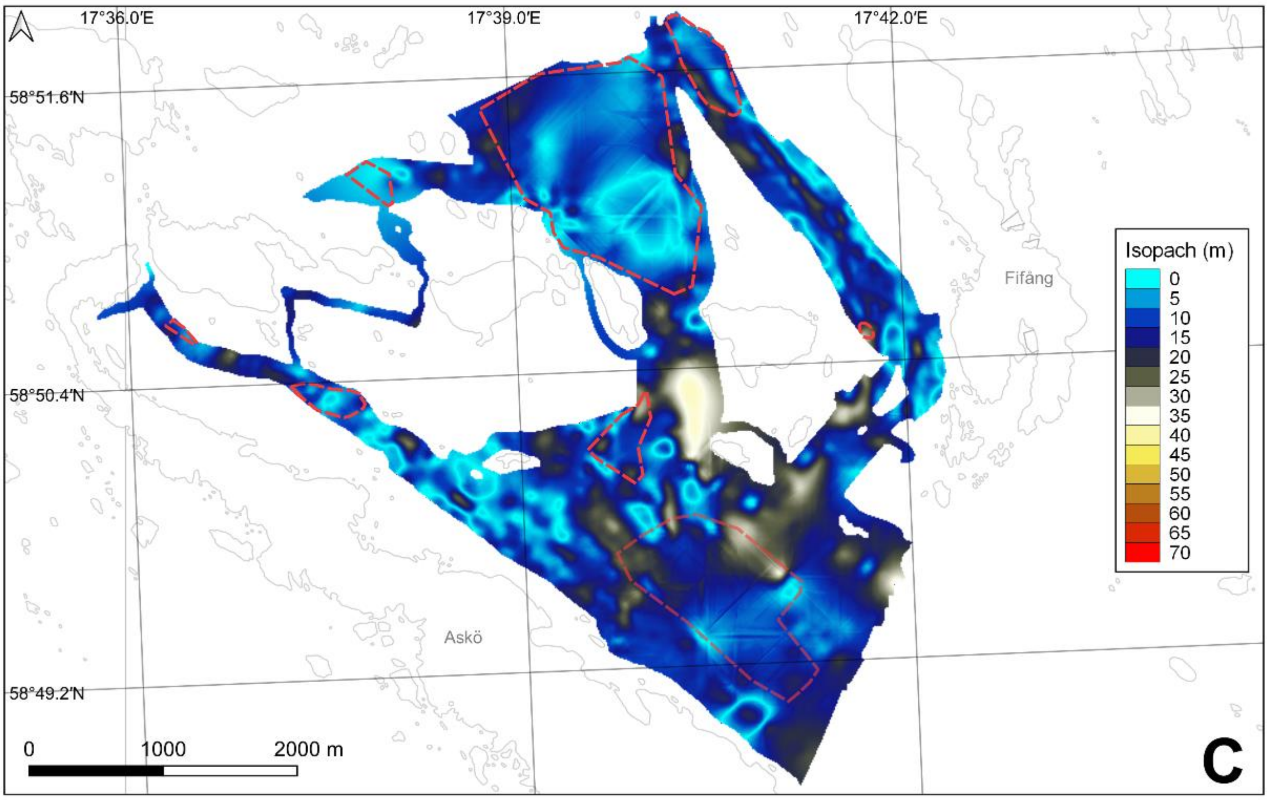

Figure C3. Isopach between S-1 and S-2 (acoustic Unit 1*). Red markings indicate where the data is uncertain due to blanks in the stratigraphy of the sub-bottom profiles.*

Appendix D – Consolidation test data

Consolidation Sample Summary			
Sample ID	EL20-IGV07-2PC-SEC3, 136-142		
Sample depth (m)	3.88		
1. Initial sample conditions		**4. Calculated Parameters**	
Sample diameter (cm)	5.04	Dry mass of sample (g)	48.78
Sample height (cm)	2.00	Initial water content (%)	44.84
Area (cm2)	19.95	Final water content (%)	31.98
Volume (cm3)	39.90	Initial dry density (g/cm3)	1.22
Ring mass (g)	60.32	Initial bulk density (g/cm3)	1.79
Sample + ring (g)	131.61	Dry unit weight (kN/m3)	12.01
Sample (g)	71.29	Volume of solids (cm3)	17.93
2. Trimmings before test		Equivalent height of solids (cm)	0.90
Tare (g)	0.74	Void ratio before test	1.21
Sample + tare (g)	32.98	Void ratio after test	0.85
Dry sample + tare (g)	23.07	Initial degree of saturation (%)	101.15
Grain density (g/cm3)	2.72	Final degree of saturation (%)	101.98
measured grain density	2.722	Porosity before test	0.55
3. End of Test		Porosity after test	0.46
Sample + ring (g)	125.28	Void ratio lost (%)	29
Tare (g)	0.74	**5. Geotechnical Properties**	
Sample + tare (g)	65.12	In-situ eff. Stress (kPa) (from MSCL table)	30.57
Dry sample + tare (g)	49.52	Preconsolidation pressure (kPa)	100
Final Height (mm)	16.80	OCR	3.27
		Compression Index (Cc)	-1.35E-01
		Recompression Index (Cr)	-1.84E-02
		e0	2.04
		e(σ'p)	1.26
		Clay (% vol)	-
		Silt (% vol)	-
		Sand (% vol)	-

	Before consolidation		After consolidation	
	Trimmings	**Sample + Ring**	**Sample + Ring**	**Sample (no ring)**
Wt. Container + Wet Soil (gm)	32.98	131.61	125.28	65.12
Wt. Container + Dry Soil (gm)	23.07	109.54	109.54	49.52
Wt. Container (gm)	0.74	60.32	60.317	0.74
Wt. Dry Soil (gm)	22.33	49.22	49.219	48.78
Water Content (%)	44.39	44.84	31.98	31.98
Void Ratio	---	1.21	0.854	---
Degree of Saturation (%)	---	101.15	101.98	---
Dry Unit Weight (N/m^3)	---	12097	14401	---

Consolidation test (EL20-IGV07-2PC-SEC3-136-142)

	Step	Applied stress (kPa)	Final displ. (mm)	Final displ. (cm)	Sample height at end (cm)	Void ratio	Porosity (%)	Fractional porosity	Strain at end (%)	sqrt T90 (min)	Coeff. Of consolidation, Cv (cm^2/s)	Coeff. Of volume change, Mv (1/kPa)	Hydraulic conductivity, k (cm/s)	Hydraulic conductivity, k (m/s)	Permeability, K (m2)
	1	2	0.17	0.02	1.98	1.19	54.34	0.54	0.86	12.35	1.13E-03	4.31E-03	4.80E-07	4.80E-09	4.92E-16
	2	4	0.28	0.03	1.97	1.18	54.13	0.54	1.39	16.32	8.46E-04	2.62E-03	2.17E-07	2.17E-09	2.23E-16
	3	8	0.47	0.05	1.95	1.16	53.70	0.54	2.33	7.69	1.77E-03	2.37E-03	4.12E-07	4.12E-09	4.22E-16
	4	16	0.69	0.07	1.93	1.13	53.05	0.53	3.47	11.86	1.12E-03	1.42E-03	1.56E-07	1.56E-09	1.60E-16
	5	32	0.98	0.10	1.90	1.10	52.38	0.52	4.92	8.36	1.55E-03	9.10E-04	1.38E-07	1.38E-09	1.42E-16
	6	64	1.32	0.13	1.87	1.06	51.46	0.51	6.57	8.89	1.41E-03	5.15E-04	7.14E-08	7.14E-10	7.32E-17
	7	128	1.74	0.17	1.83	1.01	50.25	0.50	8.70	4.46	2.70E-03	3.32E-04	8.80E-08	8.80E-10	9.02E-17
	8	256	2.26	0.23	1.77	0.96	48.93	0.49	11.30	3.82	3.00E-03	2.02E-04	5.93E-08	5.93E-10	6.08E-17
	9	512	2.92	0.29	1.71	0.88	46.92	0.47	14.60	2.02	5.31E-03	1.30E-04	6.79E-08	6.79E-10	6.96E-17
VCL	10	1020	3.65	0.37	1.63	0.80	44.57	0.45	18.30	2.15	4.59E-03	7.13E-05	3.21E-08	3.21E-10	3.29E-17
	11	2050	4.36	0.44	1.56	0.73	42.06	0.42	21.80	0.83	1.09E-02	3.44E-05	3.70E-08	3.70E-10	3.79E-17
	12	1020	4.32	0.43	1.57	0.73	42.20	0.42	21.60	0.07	1.25E-01	2.01E-06	2.46E-08	2.46E-10	2.52E-17
	13	512	4.21	0.42	1.58	0.74	42.59	0.43	21.00	0.39	2.22E-02	1.05E-05	2.30E-08	2.30E-10	2.36E-17
	14	256	4.09	0.41	1.59	0.76	43.05	0.43	20.40	0.49	1.82E-02	2.38E-05	4.26E-08	4.26E-10	4.37E-17
	15	128	3.97	0.40	1.60	0.77	43.47	0.43	19.80	2.42	3.72E-03	4.77E-05	1.74E-08	1.74E-10	1.78E-17
	16	64	3.81	0.38	1.62	0.79	44.04	0.44	19.00	4.31	2.13E-03	1.25E-04	2.60E-08	2.60E-10	2.67E-17
	17	32	3.67	0.37	1.63	0.80	44.51	0.45	18.30	10.00	9.35E-04	2.18E-04	2.00E-08	2.00E-10	2.05E-17
	18	8	3.36	0.34	1.66	0.84	45.53	0.46	16.80	12.70	7.56E-04	6.37E-04	4.73E-08	4.73E-10	4.85E-17
	19	4	3.20	0.32	1.68	0.85	46.06	0.46	16.00	83.63	1.18E-04	1.99E-03	2.31E-08	2.31E-10	2.37E-17

Consolidation Sample Summary			
Sample ID	EL20-IGV07-2PC-SEC3,130-136		
Sample depth (m)	3.81		
1. Initial sample conditions		**4. Calculated Parameters**	
Sample diameter (cm)	5.04	Dry mass of sample (g)	47.62
Sample height (cm)	2.00	Initial water content (%)	53.63
Area (cm2)	19.95	Final water content (%)	30.38
Volume (cm3)	39.90	Initial dry density (g/cm3)	1.19
Ring mass (g)	60.44	Initial bulk density (g/cm3)	1.85
Sample + ring (g)	134.22	Dry unit weight (kN/m3)	11.72
Sample (g)	73.78	Volume of solids (cm3)	17.44
2. Trimmings before test		Equivalent height of solids (cm)	0.87
Tare (g)	0.76	Void ratio before test	1.27
Sample + tare (g)	39.77	Void ratio after test	0.597
Dry sample + tare (g)	26.40	Initial degree of saturation	115.3
Grain density (g/cm3)	2.73	Final degree of saturation	139.11
3. End of Test		Porosity before test	0.56
Sample + ring (g)	123.05	Porosity after test	0.37
Tare (g)	0.74	Void ratio lost (%)	53
Sample + tare (g)	62.82	**4. Geotechnical Properties**	
Dry sample + tare (g)	48.36	In-situ eff. Stress (kPa) (from MS(	29.91
Final Height (mm)	14.06	Preconsolidation pressure (kPa)	80
		OCR	2.67
		Compression Index (Cc)	-0.188
		Recompression Index (Cr)	-0.024
		e0	2.58
		e(σ'p)	1.15
		Clay (% vol)	47
		Silt (% vol)	53
		Sand (% vol)	0

	Before consolidation		After consolidation	
	Trimmings	**Sample + Ring**	**Sample + Ring**	**Sample (no ring)**
Wt. Container + Wet Soil (gm)	39.77	134.22	123.05	62.82
Wt. Container + Dry Soil (gm)	26.40	108.46	108.46	48.36
Wt. Container (gm)	0.76	60.44	60.44	0.74
Wt. Dry Soil (gm)	25.63	48.02	48.02	47.62
Water Content (%)	52.17	53.63	30.38	30.38
Void Ratio	---	1.27	0.60	---
Degree of Saturation (%)	---	115.3	139.11	---
Dry Unit Weight (N/m^3)	---	11802	16788	---

Consolidation test (EL20-IGV07-2PC-SEC3-130-136)

	Step	Applied stress (kPa)	Final displ. (mm)	Final displ. (cm)	Sample height at end (cm)	Void ratio	Fractional porosity	Porosity (%)	Strain at end (%)	sqrt T90 (sec)	Coeff. Of consolidation, Cv (cm^2/s)	Coeff. Of volume change, Mv (1/kPa)	Hydraulic conductivity, k (cm/s)	Hydraulic conductivity, k (m/s)	Permeability, K (m2)
	1	2.3	0.32	0.03	1.968	1.24	0.55	55.36	1.58	560.64	1.5E-03	6.9E-03	1.0E-06	1.0E-08	1.0E-15
	2	4.6	0.45	0.05	1.955	1.22	0.55	54.95	2.26	#####	5.6E-04	3.0E-03	1.6E-07	1.6E-09	1.7E-16
	3	9.2	0.64	0.06	1.936	1.20	0.55	54.55	3.19	526.20	1.5E-03	2.0E-03	3.0E-07	3.0E-09	3.1E-16
	4	18.4	0.90	0.09	1.910	1.17	0.54	53.92	4.51	269.52	2.9E-03	1.4E-03	4.1E-07	4.1E-09	4.2E-16
	5	36.8	1.19	0.12	1.881	1.14	0.53	53.27	5.95	536.04	1.4E-03	7.8E-04	1.1E-07	1.1E-09	1.1E-16
	6	73.6	1.54	0.15	1.846	1.10	0.52	52.38	7.70	576.78	1.3E-03	4.8E-04	6.0E-08	6.0E-10	6.1E-17
	7	147.2	2.34	0.23	1.766	1.01	0.50	50.25	11.70	747.54	9.2E-04	5.4E-04	4.9E-08	4.9E-10	5.1E-17
	8	294.4	3.65	0.37	1.635	0.86	0.46	46.15	18.30	490.86	1.2E-03	4.5E-04	5.5E-08	5.5E-10	5.6E-17
VCL	9	588.8	4.54	0.45	1.546	0.76	0.43	43.05	22.70	258.60	2.1E-03	1.5E-04	3.0E-08	3.0E-10	3.1E-17
	10	1173	5.32	0.53	1.468	0.67	0.40	40.01	26.60	120.06	4.0E-03	6.7E-05	2.6E-08	2.6E-10	2.7E-17
	11	2357.5	5.94	0.59	1.406	0.60	0.37	37.38	29.70	143.88	3.0E-03	2.6E-05	7.8E-09	7.8E-11	8.0E-18

The incorrect sample diameter was inserted to the ICON P software prior to the test, therefore, the sample diameter and height had to be adjusted and the parameters marked in green calculated manually. The wrong sample diameter also resulted in a applied stress which exceeded the maximum stress allowed for the test, which resulted in the test automatically stopping at the highest load step (step 11).

Consolidation Sample Summary

Sample ID	EL20-IGV07-2PC-SEC3,120-125
Sample depth (m)	**3.71**

1. Initial sample conditions		**4. Calculated Parameters**	
Sample diameter (cm)	5.04	Dry mass of sample (g)	43.12
Sample height (cm)	2.00	Initial water content (%)	53.63
Area (cm2)	19.95	Final water content (%)	30.38
Volume (cm3)	39.90	Initial dry density (g/cm3)	1.08
Ring mass (g)	59.00	Initial bulk density (g/cm3)	1.74
Sample + ring (g)	128.59	Dry unit weight (kN/m3)	10.61
Sample (g)	69.59	Volume of solids (cm3)	15.85
2. Trimmings before test		Equivalent height of solids (cm)	0.79
Tare (g)	0.74	Void ratio before test	1.44
Sample + tare (g)	41.78	Void ratio after test	0.91
Dry sample + tare (g)	26.90	Initial degree of saturation	115.30
Grain density (g/cm3)	2.72	Final degree of saturation	139.11
measured grain density	2.726	Porosity before test	0.59
3. End of Test		Porosity after test	0.48
Sample + ring (g)	120.14	Void ratio lost (%)	37
Tare (g)	0.75	**5. Geotechnical Properties**	
Sample + tare (g)	59.87	In-situ eff. Stress (kPa) (from MSCL table)	28.93
Dry sample + tare (g)	43.86	Preconsolidation pressure (kPa)	60.00
Final Height (mm)	15.71	OCR	2.07
		Compression Index (Cc)	-0.190
		Recompression Index (Cr)	-0.015
		e0	2.95
		e(σ'p)	1.36
		Clay (% vol)	51
		Silt (% vol)	49
		Sand (% vol)	0

	Before consolidation		**After consolidation**	
	Trimmings	**Sample + Ring**	**Sample + Ring**	**Sample (no ring)**
Wt. Container + Wet Soil (gm)	41.78	128.59	120.14	59.87
Wt. Container + Dry Soil (gm)	26.90	103.59	103.59	43.86
Wt. Container (gm)	0.74	59.00	59.00	0.75
Wt. Dry Soil (gm)	26.16	44.59	44.59	43.12
Water Content (%)	56.89	56.08	37.13	37.13
Void Ratio	---	1.44	0.914	---
Degree of Saturation (%)	---	106.28	110.66	---
Dry Unit Weight (N/m^3)	---	10958	13954	---

Consolidation test (EL20-IGV07-2PC-SEC3-120-125)

	Step	Applied stress (kPa)	Final displ. (mm)	Final displ. (cm)	Sample height at end (cm)	Void ratio	Fractional porosity	Porosity (%)	Strain at end (%)	sqrt T90 (min)	Coeff. Of consolidation, Cv (cm^2/s)	Coeff. Of volume change, Mv (1/kPa)	Hydraulic conductivity, k (cm/s)	Hydraulic conductivity, k (m/s)	Permeability, K (m2)
	1	2	0.14	0.01	1.99	1.42	0.59	58.68	0.70	9.95	1.41E-03	3.52E-03	4.87E-07	4.87E-09	4.99E-16
	2	4	0.21	0.02	1.98	1.41	0.59	58.51	1.05	26.83	5.18E-04	1.73E-03	8.77E-08	8.77E-10	8.99E-17
	3	8	0.38	0.04	1.96	1.39	0.58	58.16	1.89	8.56	1.60E-03	2.10E-03	3.30E-07	3.30E-09	3.38E-16
	4	16	0.59	0.06	1.94	1.37	0.58	57.81	2.94	11.88	1.13E-03	1.32E-03	1.47E-07	1.47E-09	1.51E-16
	5	32	0.88	0.09	1.91	1.33	0.57	57.08	4.41	9.11	1.44E-03	9.18E-04	1.30E-07	1.30E-09	1.33E-16
	6	64	1.33	0.13	1.87	1.28	0.56	56.14	6.63	8.25	1.53E-03	6.91E-04	1.04E-07	1.04E-09	1.07E-16
	7	128	2.17	0.22	1.78	1.17	0.54	53.92	10.80	12.14	9.70E-04	6.57E-04	6.24E-08	6.24E-10	6.40E-17
	8	256	3.55	0.36	1.64	1.00	0.50	50.00	17.80	11.53	9.00E-04	5.42E-04	4.78E-08	4.78E-10	4.90E-17
VCL	9	512	4.51	0.45	1.55	0.89	0.47	47.01	22.50	8.59	1.05E-03	1.87E-04	1.92E-08	1.92E-10	1.97E-17
	10	1020	5.34	0.53	1.47	0.79	0.44	44.04	26.70	4.14	1.94E-03	8.07E-05	1.54E-08	1.54E-10	1.58E-17
	11	2050	6.12	0.61	1.39	0.69	0.41	40.86	30.60	2.25	3.19E-03	3.83E-05	1.20E-08	1.20E-10	1.23E-17
	12	1020	6.02	0.60	1.40	0.70	0.41	41.28	30.10	0.93	7.41E-03	4.87E-06	3.54E-09	3.54E-11	3.63E-18
	13	512	5.89	0.59	1.41	0.72	0.42	41.83	29.40	1.96	3.56E-03	1.28E-05	4.48E-09	4.48E-11	4.59E-18
	14	256	5.70	0.57	1.43	0.74	0.43	42.59	28.50	2.41	2.96E-03	3.64E-05	1.06E-08	1.06E-10	1.09E-17
	15	128	5.47	0.55	1.45	0.77	0.44	43.50	27.40	8.43	8.71E-04	8.98E-05	7.67E-09	7.67E-11	7.87E-18
	16	64	5.22	0.52	1.48	0.80	0.44	44.48	26.10	14.13	5.37E-04	1.99E-04	1.05E-08	1.05E-10	1.08E-17
	17	32	4.99	0.50	1.50	0.83	0.45	45.33	24.90	37.33	2.10E-04	3.65E-04	7.52E-09	7.52E-11	7.71E-18
	18	8	4.54	0.45	1.55	0.88	0.47	46.92	22.70	47.11	1.74E-04	9.33E-04	1.59E-08	1.59E-10	1.63E-17
	19	4	4.29	0.43	1.57	0.91	0.48	47.75	21.50	118.16	7.26E-05	3.03E-03	2.16E-08	2.16E-10	2.21E-17

Consolidation Sample Summary			
Sample ID	EL20-IGV07-SEC2, 147-152-B		
Sample depth (m)	2.46		
1. Initial sample conditions		**4. Calculated Parameters**	
Sample diameter (cm)	5.04	Dry mass of sample (g)	36.24
Sample height (cm)	2.00	Initial water content (%)	72.95
Area (cm2)	19.95	Final water content (%)	41.84
Volume (cm3)	39.90	Initial dry density (g/cm3)	0.91
Ring mass (g)	60.31	Initial bulk density (g/cm3)	1.59
Sample + ring (g)	123.89	Dry unit weight (kN/m3)	8.92
Sample (g)	63.58	Volume of solids (cm3)	13.23
2. Trimmings before test		Equivalent height of solids (cm)	0.66
Tare (g)	0.74	Void ratio before test	1.97
Sample + tare (g)	52.43	Void ratio after test	1.07
Dry sample + tare (g)	30.79	Initial degree of saturation	101.25
Grain density (g/cm3)	2.74	Final degree of saturation	107.30
measured grain density	2.743	Porosity before test	0.66
3. End of Test		Porosity after test	0.52
Sample + ring (g)	112.45	Void ratio lost (%)	46
Tare (g)	0.73	**5. Geotechnical Properties**	
Sample + tare (g)	52.13	In-situ eff. Stress (kPa) (from MSCL table)	18.61
Dry sample + tare (g)	36.97	Preconsolidation pressure (kPa)	45.00
Final Height (mm)	13.91	OCR	2.42
		Compression Index (Cc)	-0.239
		Recompression Index (Cr)	-0.011
		e0	4.66
		e(σ'p)	1.89
		Clay (% vol)	54
		Silt (% vol)	46
		Sand (% vol)	0

	Before consolidation		After consolidation	
	Trimmings	**Sample + Ring**	**Sample + Ring**	**Sample (no ring)**
Wt. Container + Wet Soil (gm)	52.43	123.89	112.45	52.13
Wt. Container + Dry Soil (gm)	30.79	97.07	97.07	36.97
Wt. Container (gm)	0.74	60.31	60.31	0.73
Wt. Dry Soil (gm)	30.06	36.76	36.76	36.24
Water Content (%)	71.98	72.95	41.84	41.84
Void Ratio	---	1.97	1.07	---
Degree of Saturation (%)	---	101.25	107.30	---
Dry Unit Weight (N/m^3)	---	9034.50	12991.00	---

Consolidation test (EL20-IGV07-2PC-SEC2-147-152-B)

	Step	Applied stress (kPa)	Final displ. (mm)	Final displ. (cm)	Sample height at end (cm)	Void ratio	Fractional porosity	Porosity (%)	Strain at end (%)	sqrt T90 (min)	Coeff. Of consolidation, Cv (cm^2/s)	Coeff. Of volume change, Mv (1/kPa)	Hydraulic conductivity, k (cm/s)	Hydraulic conductivity, k (m/s)	Permeability, K (m2)
	1	2	0.08	0.01	1.99	1.96	0.66	66.22	0.42	4.91	2.87E-03	2.11E-03	5.93E-07	5.93E-09	6.08E-16
	2	4	0.15	0.02	1.98	1.95	0.66	66.10	0.76	14.47	9.65E-04	1.70E-03	1.61E-07	1.61E-09	1.65E-16
	3	8	0.33	0.03	1.97	1.93	0.66	65.87	1.65	9.64	1.43E-03	2.21E-03	3.11E-07	3.11E-09	3.19E-16
	4	16	0.54	0.05	1.95	1.89	0.65	65.40	2.69	8.17	1.66E-03	1.31E-03	2.12E-07	2.12E-09	2.17E-16
	5	32	0.91	0.09	1.91	1.84	0.65	64.79	4.56	8.41	1.56E-03	1.17E-03	1.79E-07	1.79E-09	1.84E-16
	6	64	1.73	0.17	1.83	1.72	0.63	63.24	8.64	18.65	6.61E-04	1.28E-03	8.28E-08	8.28E-10	8.49E-17
	7	128	4.13	0.41	1.59	1.36	0.58	57.63	20.60	43.10	2.39E-04	1.87E-03	4.39E-08	4.39E-10	4.50E-17
VCL	8	256	5.44	0.54	1.46	1.17	0.54	53.92	27.20	18.56	4.41E-04	5.12E-04	2.21E-08	2.21E-10	2.27E-17
	9	512	6.49	0.65	1.35	1.01	0.50	50.25	32.50	7.87	8.84E-04	2.06E-04	1.79E-08	1.79E-10	1.84E-17
	10	1020	7.42	0.74	1.26	0.87	0.47	46.55	37.10	8.77	6.85E-04	9.04E-05	6.08E-09	6.08E-11	6.23E-18
	11	2050	8.22	0.82	1.18	0.75	0.43	42.92	41.10	4.12	1.27E-03	3.89E-05	4.86E-09	4.86E-11	4.98E-18
	12	1020	8.11	0.81	1.19	0.77	0.43	43.44	40.50	1.24	3.99E-03	5.27E-06	2.06E-09	2.06E-11	2.11E-18
	13	512	7.97	0.80	1.20	0.79	0.44	44.13	39.80	3.80	1.33E-03	1.39E-05	1.81E-09	1.81E-11	1.86E-18
	14	256	7.79	0.78	1.22	0.82	0.45	44.93	38.90	8.95	5.80E-04	3.46E-05	1.97E-09	1.97E-11	2.02E-18
	15	128	7.55	0.76	1.24	0.85	0.46	45.98	37.80	11.34	4.73E-04	9.21E-05	4.28E-09	4.28E-11	4.39E-18
	16	64	7.20	0.72	1.28	0.90	0.47	47.48	36.00	14.15	3.98E-04	2.77E-04	1.08E-08	1.08E-10	1.11E-17
	17	32	6.93	0.69	1.31	0.94	0.49	48.56	34.70	43.83	1.35E-04	4.18E-04	5.53E-09	5.53E-11	5.67E-18
	18	8	6.46	0.65	1.35	1.01	0.50	50.25	32.30	109.76	5.70E-05	9.85E-04	5.51E-09	5.51E-11	5.65E-18
	19	4	6.09	0.61	1.39	1.07	0.52	51.69	30.50	323.69	2.06E-05	4.59E-03	9.25E-09	9.25E-11	9.49E-18

Consolidation Sample Summary			
Sample ID	EL20-IGV07-SEC2, 147-152-A		
Sample depth (m)	2.46		

1. Initial sample conditions		**4. Calculated Parameters**	
Sample diameter (cm)	5.04	Dry mass of sample (g)	37.88
Sample height (cm)	2.00	Initial water content (%)	69.74
Area (cm2)	19.95	Final water content (%)	39.25
Volume (cm3)	39.90	Initial dry density (g/cm3)	0.95
Ring mass (g)	58.96	Initial bulk density (g/cm3)	1.65
Sample + ring (g)	124.73	Dry unit weight (kN/m3)	9.32
Sample (g)	65.77	Volume of solids (cm3)	13.77
2. Trimmings before test		Equivalent height of solids (cm)	0.69
Tare (g)	0.74	Void ratio before test	1.83
Sample + tare (g)	39.10	Void ratio after test	0.95
Dry sample + tare (g)	23.40	Initial degree of saturation	104.69
Grain density (g/cm3)	2.75	Final degree of saturation	114.11
measured grain density	2.748	Porosity before test	0.65
3. End of Test		Porosity after test	0.49
Sample + ring (g)	112.92	Void ratio lost (%)	48
Tare (g)	0.74	**5. Geotechnical Properties**	
Sample + tare (g)	53.48	In-situ eff. Stress (kPa) (from MSCL table)	18.61
Dry sample + tare (g)	38.61	Preconsolidation pressure (kPa)	45.00
Final Height (mm)	13.74	OCR	2.42
		Compression Index (Cc)	-0.246
		Recompression Index (Cr)	-0.020
		e0	4.32
		e(σ'p)	1.7
		Clay (% vol)	73
		Silt (% vol)	27
		Sand (% vol)	0

	Before consolidation		After consolidation	
	Trimmings	**Sample + Ring**	**Sample + Ring**	**Sample (no ring)**
Wt. Container + Wet Soil (gm)	39.10	124.73	112.92	53.48
Wt. Container + Dry Soil (gm)	23.40	97.71	97.71	38.61
Wt. Container (gm)	0.74	58.96	58.96	0.74
Wt. Dry Soil (gm)	22.67	38.75	38.75	37.88
Water Content (%)	69.26	69.74	39.25	39.25
Void Ratio	---	1.83	0.95	---
Degree of Saturation (%)	---	104.69	114.11	---
Dry Unit Weight (N/m^3)	---	9523.60	13858.00	---

	Consolidation test (EL20-IGV07-2PC-SEC2-147-152-A)														
	Step	Applied stress (kPa)	Final displ. (mm)	Final displ. (cm)	Sample height at end (cm)	Void ratio	Porosity (%)	Fractional porosity	Strain at end (%)	sqrt T90 (min)	Coeff. Of consolidation, Cv (cm^2/s)	Coeff. Of volume change, Mv (1/kPa)	Hydraulic conductivity, k (cm/s)	Hydraulic conductivity, k (m/s)	Permeability, K (m2)
	1	2	0.21	0.02	1.98	1.80	64.29	0.64	1.06	6.91	2.02E-03	5.31E-03	1.05E-06	1.05E-08	1.08E-15
	2	4	0.34	0.03	1.97	1.78	64.03	0.64	1.70	13.18	1.04E-03	3.20E-03	3.27E-07	3.27E-09	3.35E-16
	3	8	0.56	0.06	1.94	1.75	63.64	0.64	2.80	9.65	1.40E-03	2.76E-03	3.78E-07	3.78E-09	3.88E-16
	4	16	0.84	0.08	1.92	1.71	63.10	0.63	4.21	12.58	1.05E-03	1.76E-03	1.81E-07	1.81E-09	1.86E-16
	5	32	1.23	0.12	1.88	1.66	62.41	0.62	6.15	14.03	9.06E-04	1.21E-03	1.08E-07	1.08E-09	1.11E-16
	6	64	2.00	0.20	1.80	1.55	60.78	0.61	10.00	22.79	5.24E-04	1.20E-03	6.19E-08	6.19E-10	6.35E-17
	7	128	4.09	0.41	1.59	1.25	55.56	0.56	20.50	29.68	3.42E-04	1.63E-03	5.48E-08	5.48E-10	5.62E-17
	8	256	5.45	0.55	1.45	1.06	51.46	0.51	27.30	14.94	5.48E-04	5.32E-04	2.86E-08	2.86E-10	2.93E-17
VCL	9	512	6.47	0.65	1.35	0.92	47.78	0.48	32.40	8.09	8.61E-04	1.99E-04	1.68E-08	1.68E-10	1.72E-17
	10	1020	7.40	0.74	1.26	0.78	43.95	0.44	37.00	3.98	1.52E-03	9.03E-05	1.34E-08	1.34E-10	1.37E-17
	11	2050	8.28	0.83	1.17	0.66	39.76	0.40	41.40	4.30	1.22E-03	4.28E-05	5.10E-09	5.10E-11	5.23E-18
	12	1020	8.20	0.82	1.18	0.67	40.16	0.40	41.00	2.49	1.97E-03	3.78E-06	7.30E-10	7.30E-12	7.49E-19
	13	512	8.04	0.80	1.20	0.69	40.97	0.41	40.20	1.92	2.60E-03	1.58E-05	4.03E-09	4.03E-11	4.13E-18
	14	256	7.84	0.78	1.22	0.72	41.89	0.42	39.20	8.34	6.16E-04	3.76E-05	2.27E-09	2.27E-11	2.33E-18
	15	128	7.61	0.76	1.24	0.76	43.02	0.43	38.00	14.67	3.63E-04	9.21E-05	3.28E-09	3.28E-11	3.36E-18
	16	64	7.27	0.73	1.27	0.80	44.54	0.45	36.30	9.65	5.78E-04	2.65E-04	1.50E-08	1.50E-10	1.54E-17
	17	32	7.02	0.70	1.30	0.84	45.56	0.46	35.10	37.78	1.55E-04	3.81E-04	5.78E-09	5.78E-11	5.93E-18
	18	8	6.53	0.65	1.35	0.91	47.56	0.48	32.60	95.50	6.47E-05	1.03E-03	6.54E-09	6.54E-11	6.71E-18
	19	4	6.26	0.63	1.37	0.95	48.61	0.49	31.30	207.36	3.16E-05	3.42E-03	1.06E-08	1.06E-10	1.09E-17

Consolidation Sample Summary			
Sample ID	EL20-IGV07-2PC-SEC2-4-7		
Sample depth (m)	1.03		

1. Initial sample conditions		**4. Calculated Parameters**	
Sample diameter (cm)	5.04	Dry mass of sample (g)	29.94
Sample height (cm)	2.00	Initial water content (%)	97.96
Area (cm2)	19.95	Final water content (%)	44.59
Volume (cm3)	39.90	Initial dry density (g/cm3)	0.75
Ring mass (g)	60.44	Initial bulk density (g/cm3)	1.51
Sample + ring (g)	120.59	Dry unit weight (kN/m3)	7.37
Sample (g)	60.15	Volume of solids (cm3)	11.01
2. Trimmings before test		Equivalent height of solids (cm)	0.55
Tare (g)	0.74	Void ratio before test	2.57
Sample + tare (g)	29.17	Void ratio after test	1.00
Dry sample + tare (g)	15.11	Initial degree of saturation	103.60
Grain density (g/cm3)	2.72	Final degree of saturation	121.89
measured grain density	2.724	Porosity before test	0.72
3. End of Test		Porosity after test	0.50
Sample + ring (g)	104.37	Void ratio lost (%)	61
Tare (g)	0.74	**5. Geotechnical Properties**	
Sample + tare (g)	44.02	In-situ eff. Stress (kPa) (from MSCL table)	7.10
Dry sample + tare (g)	30.67	Preconsolidation pressure (kPa)	50.00
Final Height (mm)	11.17	OCR	7.04
		Compression Index (Cc)	-0.352
		Recompression Index (Cr)	-0.008
		e(σ'p)	2.5
		e0	9.92
		Clay (% vol)	95
		Silt (% vol)	5
		Sand (% vol)	0

	Before consolidation		After consolidation	
	Trimmings	**Sample + Ring**	**Sample + Ring**	**Sample (no ring)**
Wt. Container + Wet Soil (gm)	29.17	120.59	104.37	44.02
Wt. Container + Dry Soil (gm)	15.11	90.82	90.82	30.67
Wt. Container (gm)	0.74	60.44	60.44	0.74
Wt. Dry Soil (gm)	14.37	30.38	30.38	29.94
Water Content (%)	97.88	97.96	44.59	44.59
Void Ratio	---	2.57	1.00	---
Degree of Saturation (%)	---	103.60	121.89	---
Dry Unit Weight (N/m^3)	---	7467.50	13371	---

Consolidation test (EL20-IGV07-2PC-SEC2-4-7)

	Step	Applied stress (kPa)	Final displ. (mm)	Final displ. (cm)	Sample height at end (cm)	Void ratio	Fractional porosity	Porosity (%)	Strain at end (%)	sqrt T90 (min)	Coeff. Of consolidation, Cv (cm^2/s)	Coeff. Of volume change, Mv (1/kPa)	Hydraulic conductivity, k (cm/s)	Hydraulic conductivity, k (m/s)	Permeability, K (m2)
	1	2	0.03	0.00	#REF!	2.57	0.72	71.99	0.14	1.41	1.00E-02	7.01E-04	6.90E-07	6.90E-09	7.08E-16
	2	4	0.15	0.02	1.98	2.55	0.72	71.83	0.76	0.29	4.88E-02	3.08E-03	1.47E-05	1.47E-07	1.51E-14
	3	8	0.21	0.02	1.98	2.54	0.72	71.75	1.03	4.85	2.87E-03	6.73E-04	1.89E-07	1.89E-09	1.94E-16
	4	16	0.31	0.03	1.97	2.52	0.72	71.59	1.54	9.68	1.42E-03	6.45E-04	9.01E-08	9.01E-10	9.24E-17
	5	32	0.54	0.05	1.95	2.48	0.71	71.26	2.71	13.50	1.00E-03	7.31E-04	7.19E-08	7.19E-10	7.37E-17
	6	64	1.51	0.15	1.85	2.30	0.70	69.70	7.54	27.49	4.63E-04	1.51E-03	6.84E-08	6.84E-10	7.01E-17
	7	128	5.84	0.58	1.42	1.53	0.60	60.47	29.20	199.89	4.71E-05	3.39E-03	1.56E-08	1.56E-10	1.60E-17
	8	256	7.52	0.75	1.25	1.23	0.55	55.16	37.60	70.72	8.87E-05	6.56E-04	5.70E-09	5.70E-11	5.85E-18
VCL	9	512	8.78	0.88	1.12	1.00	0.50	50.00	43.90	35.26	1.41E-04	2.46E-04	3.40E-09	3.40E-11	3.49E-18
	10	1020	9.77	0.98	1.02	0.83	0.45	45.30	48.80	21.93	1.85E-04	9.63E-05	1.75E-09	1.75E-11	1.79E-18
	11	2050	10.58	1.06	0.94	0.68	0.41	40.55	52.90	18.55	1.84E-04	3.98E-05	7.18E-10	7.18E-12	7.36E-19
	12	1020	10.48	1.05	0.95	0.70	0.41	41.18	52.40	9.16	3.46E-04	4.93E-06	1.67E-10	1.67E-12	1.71E-19
	13	512	10.32	1.03	0.97	0.73	0.42	42.16	51.60	19.12	1.70E-04	1.58E-05	2.64E-10	2.64E-12	2.71E-19
	14	256	10.13	1.01	0.99	0.76	0.43	43.31	50.60	21.81	1.55E-04	3.74E-05	5.67E-10	5.67E-12	5.81E-19
	15	128	9.91	0.99	1.01	0.80	0.45	44.51	49.60	68.67	5.13E-05	8.39E-05	4.22E-10	4.22E-12	4.33E-19
	16	64	9.59	0.96	1.04	0.86	0.46	46.24	47.90	47.23	7.86E-05	2.53E-04	1.95E-09	1.95E-11	2.00E-18
	17	32	9.34	0.93	1.07	0.90	0.47	47.48	46.70	165.41	2.37E-05	3.90E-04	9.08E-10	9.08E-12	9.31E-19
	18	8	8.99	0.90	1.10	0.97	0.49	49.16	44.90	143.29	2.90E-05	7.26E-04	2.06E-09	2.06E-11	2.11E-18
	19	4	8.83	0.88	1.12	1.00	0.50	49.87	44.10	0.00	0.00E+00	1.98E-03	0.00E+00	0.00E+00	0.00E+00

Consolidation Sample Summary			
Sample ID	EL20-IGV07-2PC-SEC2-0-3		
Sample depth (m)	**0.99**		
1. Initial sample conditions		**4. Calculated Parameters**	
Sample diameter (cm)	5.04	Dry mass of sample (g)	27.59
Sample height (cm)	2.00	Initial water content (%)	106.34
Area (cm2)	19.95	Final water content (%)	48.13
Volume (cm3)	39.90	Initial dry density (g/cm3)	0.69
Ring mass (g)	58.96	Initial bulk density (g/cm3)	1.44
Sample + ring (g)	116.59	Dry unit weight (kN/m3)	6.79
Sample (g)	57.63	Volume of solids (cm3)	10.11
2. Trimmings before test		Equivalent height of solids (cm)	0.51
Tare (g)	0.7	Void ratio before test	2.90
Sample + tare (g)	32.2	Void ratio after test	1.26
Dry sample + tare (g)	16.0	Initial degree of saturation	106.34
Grain density (g/cm3)	2.73	Final degree of saturation	48.13
Measured grain density	2.728	Porosity before test	0.74
3. End of Test		Porosity after test	0.56
Sample + ring (g)	100.33	Void ratio lost (%)	57
Tare (g)	0.74	**5. Geotechnical Properties**	
Sample + tare (g)	41.60	In-situ eff. Stress (kPa) (from MSCL table)	6.85
Dry sample + tare (g)	28.33	Preconsolidation pressure (kPa)	45
Final Height (mm):	11.58	OCR	6.57
		Compression Index (Cc)	-0.304
		Recompression Index (Cr)	-0.013
		e(σ'p)	2.8
		e0	8.87
		Clay (% vol)	75
		Silt (% vol)	25
		Sand (% vol)	0

	Before consolidation		After consolidation	
	Trimmings	**Sample + Ring**	**Sample + Ring**	**Sample (no ring)**
Wt. Container + Wet Soil (gm)	32.17	116.59	100.33	41.60
Wt. Container + Dry Soil (gm)	15.99	86.89	86.89	28.33
Wt. Container (gm)	0.73	58.96	58.96	0.74
Wt. Dry Soil (gm)	15.26	27.93	27.93	27.59
Water Content (%)	106.10	106.34	48.13	48.13
Void Ratio	---	2.90	1.26	---
Degree of Saturation (%)	---	100.10	104.39	---
Dry Unit Weight (N/m^3)	---	6864.10	11854.00	---

Consolidation test (EL20-IGV07-2PC-SEC2-0-3)

	Step	Applied stress (kPa)	Final displ. (mm)	Final displ. (cm)	Sample height at end (cm)	Void ratio	Fractional porosity	Porosity (%)	Strain at end (%)	sqrt T90 (min)	Coeff. Of consolidation , Cv (cm^2/s)	Coeff. Of volume change, Mv (1/kPa)	Hydraulic conductivity, k (cm/s)	Hydraulic conductivity, k (m/s)	Permeability, K (m2)
	1	2	0.11	0.01	1.99	2.88	0.74	74.23	0.57	4.39	3.20E-03	2.84E-03	8.93E-07	8.93E-09	9.16E-16
	2	4	0.20	0.02	1.98	2.86	0.74	74.09	1.00	14.17	9.82E-04	2.17E-03	2.09E-07	2.09E-09	2.14E-16
	3	8	0.38	0.04	1.96	2.83	0.74	73.89	1.90	22.26	6.17E-04	2.24E-03	1.36E-07	1.36E-09	1.39E-16
	4	16	0.59	0.06	1.94	2.79	0.74	73.61	2.93	16.27	8.27E-04	1.29E-03	1.05E-07	1.05E-09	1.08E-16
	5	32	0.98	0.10	1.90	2.71	0.73	73.05	4.88	22.80	5.72E-04	1.22E-03	6.84E-08	6.84E-10	7.01E-17
	6	64	2.08	0.21	1.79	2.50	0.71	71.43	10.40	49.09	2.46E-04	1.72E-03	4.14E-08	4.14E-10	4.25E-17
	7	128	6.00	0.60	1.40	1.73	0.63	63.37	30.00	146.19	6.16E-05	3.07E-03	1.85E-08	1.85E-10	1.90E-17
VCL	8	256	7.47	0.75	1.25	1.44	0.59	59.02	37.30	73.29	8.49E-05	5.73E-04	4.77E-09	4.77E-11	4.89E-18
	9	512	8.65	0.87	1.13	1.21	0.55	54.75	43.30	35.97	1.40E-04	2.32E-04	3.18E-09	3.18E-11	3.26E-18
	10	1020	9.58	0.96	1.04	1.03	0.51	50.74	47.90	21.03	1.99E-04	9.10E-05	1.78E-09	1.78E-11	1.83E-18
	11	2050	10.41	1.04	0.96	0.87	0.47	46.55	52.00	13.81	2.56E-04	4.03E-05	1.01E-09	1.01E-11	1.04E-18
	12	1020	10.29	1.03	0.97	0.89	0.47	47.17	51.50	2.69	1.22E-03	5.62E-06	6.75E-10	6.75E-12	6.92E-19
	13	512	10.11	1.01	0.99	0.93	0.48	48.16	50.50	13.28	2.55E-04	1.80E-05	4.51E-10	4.51E-12	4.62E-19
	14	256	9.89	0.99	1.01	0.97	0.49	49.26	49.50	43.58	8.11E-05	4.19E-05	3.33E-10	3.33E-12	3.41E-19
	15	128	9.69	0.97	1.03	1.01	0.50	50.25	48.40	36.95	9.97E-05	8.16E-05	7.98E-10	7.98E-12	8.18E-19
	16	64	9.34	0.93	1.07	1.08	0.52	51.92	46.70	49.62	7.83E-05	2.71E-04	2.08E-09	2.08E-11	2.13E-18
	17	32	9.09	0.91	1.09	1.13	0.53	53.05	45.50	188.36	2.18E-05	3.85E-04	8.24E-10	8.24E-12	8.45E-19
	18	8	8.67	0.87	1.13	1.21	0.55	54.75	43.30	337.63	1.29E-05	8.89E-04	1.13E-09	1.13E-11	1.16E-18
	19	4	8.42	0.84	1.16	1.26	0.56	55.75	42.10	936.76	4.95E-06	3.08E-03	1.49E-09	1.49E-11	1.53E-18

Appendix E - Groundwater fluctuations at Sandvik

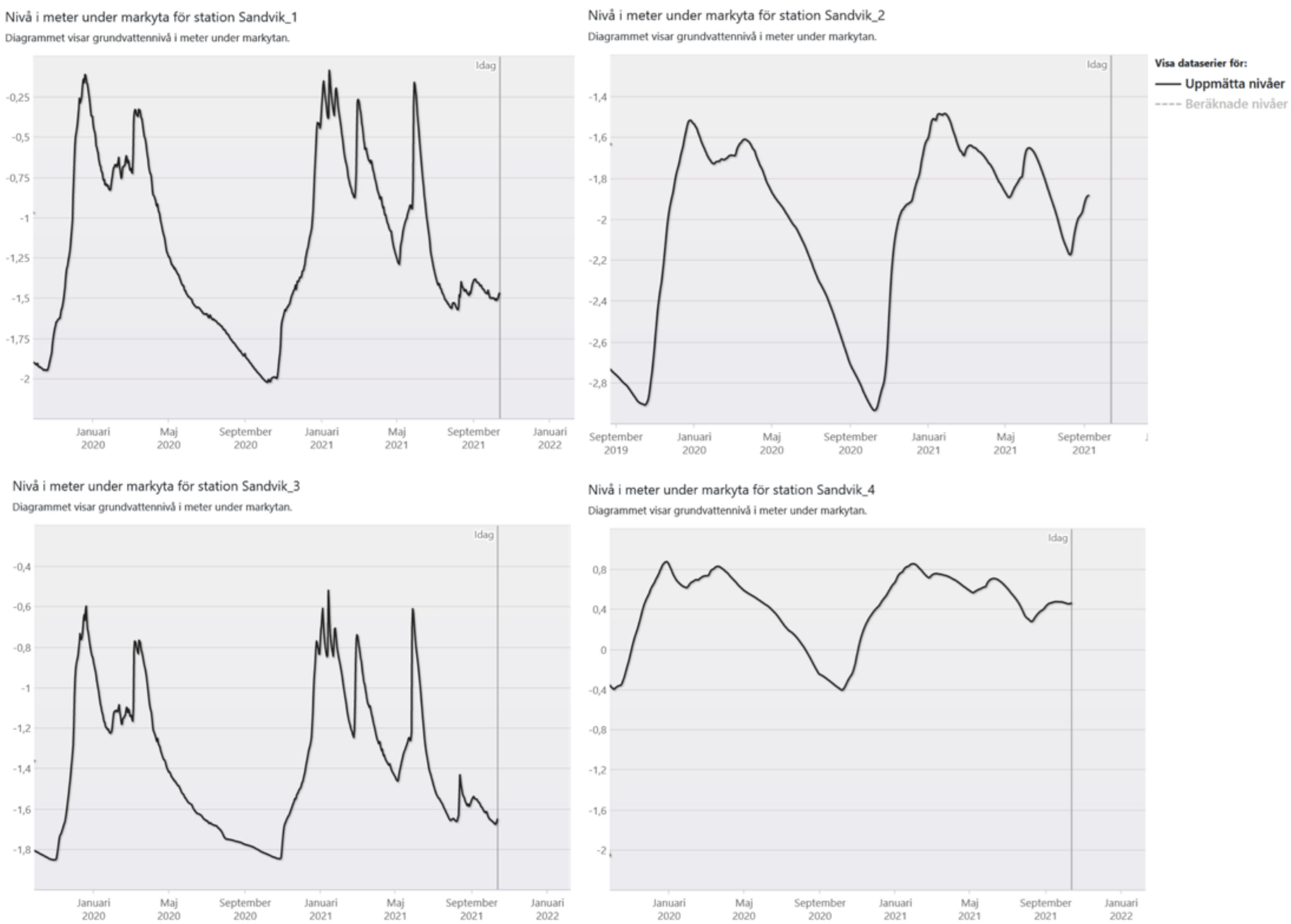

Figure E1. Groundwater fluctuations at Sandvik measuring station in three different geological settings. Station Sandvik_1 and 2 is in bedrock aquifers. Station Sandvik_3 is in a sand and/or gravel aquifer. Station Sandvik_4 is in a non-varved clay aquifer. (SGU, 2021: https://www.sgu.se/grundvatten/grundvattennivaer/matstationer/. [2021-10-13])